Dissertation

submitted to the

Combined Faculties for the Natural Sciences and for Mathematics

of the Ruperto-Carola University of Heidelberg, Germany

for the degree of

Doctor of Natural Sciences

Put forward by

Diplom-Physiker: Henrik Hetzheim
Born in: Berlin

Oral examination: 14.1.2009

Ionization and bound-state relativistic quantum dynamics in laser-driven multiply charged ions

Referees: **Prof. Dr. Christoph H. Keitel**

Prof. Dr. Joachim H. Ullrich

Zusammenfassung

Die Wechselwirkung von ultra-starken Laserfeldern mit mehrfach geladenen wasserstoffartigen Ionen lässt sich zum einen in die Ionisationsdynamik und zum anderen in die gebundene Dynamik unterteilen. Beide Bereiche werden numerisch mittels der Diracgleichung in zwei Dimensionen und der klassisch relativistischen Monte-Carlo Simulation untersucht. Zum Besseren Verständnis der zugrunde liegenden höchst nichtlinearen physikalischen Prozesse wird die Entwicklung von wohldefinierten ultra-starken Laserfeldern weiter vorangetrieben, die bestens geeignet sind um z.B. Magnetfeldeffekte des Laserfeldes zu studieren, welche eine zusätzliche Bewegung des Elektrons in die Laserpropagationsrichtung bewirken. Eine neue Methode zur sensitiven Bestimmung dieser ultra-starker Laserintensitäten vom optischen Frequenzbereich über den UV zum XUV Bereich wird in dieser Arbeit vorgestellt und angewendet. Im Bereich der gebundenen Dynamik ist die Bestimmung der Mehrphotonenübergangsmatrixelemente zwischen verschieden Zuständen mittels Rabi Oszillationen untersucht worden.

Abstract

The interaction of ultra-strong laser fields with multiply charged hydrogen-like ions can be distinguished in an ionization and a bound dynamics regime. Both are investigated by means of numerically solving the Dirac equation in two dimensions and by a classical relativistic Monte-Carlo simulation. For a better understanding of highly nonlinear physical processes the development of a well characterized ultra-intense relativistic laser field strength has been driven forward, capable of studying e.g. the magnetic field effects of the laser resulting in an additional electron motion in the laser propagation direction. A novel method to sensitively measure these ultra-strong laser intensities is developed and employed from the optical via the UV towards the XUV frequency regime. In the bound dynamics field, the determination of multiphoton transition matrixelements has been investigated between different bound states via Rabi oscillations.

Contents

1 Introduction **9**

2 Fundamental aspects of the dynamics of laser-matter interaction **15**

2.1 Ionization dynamics 16

2.1.1 Non-relativistic laser-atom interaction 19

2.1.2 Relativistic laser-ion interaction 21

2.2 Bound dynamics 24

2.2.1 Dipole/Non-dipole interaction 25

2.3 Properties of multiply charged ions 28

3 Model system and numerical approach **31**

3.1 General framework 31

3.2 The Dirac atom in 2D 32

3.2.1 The soft-core potential 32

3.2.2 The generation of energy eigenstates 33

3.2.3 Spectral method 35

3.2.4 σ_3 component of the total angular momentum 38

3.2.5 Parity 40

3.2.6 Selection rules 42

3.3 The 2D Dirac atom in a laser field 43

3.3.1 The laser pulse 43

3.3.2 The Split-Operator technique 45

3.4 Observables 48

3.5 Classical relativistic model 50

3.5.1 Monte-Carlo simulation 50

4 Ionization dynamics of multiply charged ions **55**
4.1 Motivation . . . 55
4.2 Ionization rate . . . 58
4.2.1 Semiclassical calculation in the non-relativistic regime . . . 59
4.2.2 Semiclassical calculation in the relativistic regime . . . 60
4.3 Determination of ultra-strong laser intensities . . . 63
4.3.1 Quantum Dirac calculation - ionization angle . . . 64
4.3.2 Classical relativistic calculation - ionization fraction . . . 72
4.4 Influence of quantum effects, laser frequency, pulse shape, length and carrier phase . . . 76
4.4.1 Investigation of the pulse length . . . 76
4.4.2 Investigation of the carrier phase . . . 78
4.4.3 Investigation of the pulse shape . . . 81
4.4.4 Investigation of the laser frequency . . . 83
4.4.5 Quantum versus classical calculation . . . 84
4.5 Conclusion . . . 87

5 Bound dynamics of multiply charged ions **89**
5.1 Motivation . . . 89
5.2 Transitions beyond the dipole approximation . . . 90
5.2.1 One photon transition . . . 93
5.2.2 Three-photon transitions . . . 98
5.3 Conclusion . . . 101

Summary and Outlook **103**

A Method of finite differences **107**

B Clifford algebra **109**

C Atomic units **111**

Chapter 1

Introduction

The relativistically correct quantum mechanical description of particles in the presence of time and space dependent classical fields is obtained by the Lorentz co-variant Dirac equation [1]. Analytical solutions of it are only possible in a few cases, e.g. for free particles [2] or for the hydrogen atom in case of plane waves [3]. Especially the latter, as an example of an interaction of matter with an external field, has been of great interest throughout the development of modern physics. An experimental breakthrough was the invention of the laser in the 1970s. It became possible to experimentally study the interaction of monochromatic coherent light with matter.

The generation of laser fields with shorter pulses, higher frequencies ω and intensities I led to new physical phenomena [4]. The existence of very short pulses is of great importance and has been used to image chemical reactions on a femtosecond scale [5] (nobel prize winner 1999, A. H. Zewail) or even electron motions on an attosecond scale [6]. New laser sources that have recently been built and those scheduled for the near future will obtain even higher frequencies. The typical wavelengths of these linear accelerator sources are $\lambda = 32$ nm (Free-Electron Laser (FEL) [7], $\omega = 1.4$ a.u.), $\lambda = 6.5$ nm (Free-Electron Laser in Hamburg (FLASH) [8], $\omega = 7$ a.u.) and $\lambda = 0.4$ nm (X-Ray Free-Electron Laser (XFEL) [9], $\omega = 114$ a.u.). Unlike the conventional lasers, in which electrons are excited in bound atomic or molecular states, these FEL's use a relativistic electron beam as lasing medium. The advantage is a widely tunable wavelength from infrared via the visible spectrum towards the UV and soft XUV range. The coherent light source is based on a

relativistic beam of electrons that passes through an undulator in the form of periodic arranged magnets which results in a sinusoidal trajectory of the electron beam. The acceleration along this path leads then to a release of photon radiation, which is emitted coherently if the electron motion is in phase with the emission of the radiation.

A further intention, beyond the aim of smaller wavelengths, is the availability of enhanced laser intensities, providing a deeper insight into the fascinating field of strong laser-matter interaction. Therefore large-scale facilities with typical parameters of kJ energy in a single pulse of nanosecond duration and terawatt powers have been built over many places around the world, e.g. at CEA-Limeil in France, in the Rutherford Appleton Laboratory in the UK and at the Institute of Laser Engineering at the Osaka University in Japan. In addition to these large facilities table-top devices are used of comparable parameters e.g. at the University of Texas Austin USA (LLNL Jan USP laser, with a peak intensity of $2 \times 10^{20}\mathrm{W/cm^2}$ [10]); the 100 terawatt facility of the LULI laboratory in France (with a peak intensity of $2 \times 10^{19}\mathrm{W/cm^2}$ [11]) or at the Max-Born Institute in Berlin (with a peak intensity of $0.8 \times 10^{19}\mathrm{W/cm^2}$ [12]). The aim for achieving intensities in the ultra-relativistic regime of the order of $10^{25}\mathrm{W/cm^2}$ e.g. by the european project of Extreme Light Infrastructure (ELI) [13] offers the opportunity to challenge the vacuum critical field strength to test the validity of QED effects through vacuum polarization [14], to study nuclear reaction and generating GeV electron beams [15] or for medical application as accomplished in cancer therapy [16]. The most striking contribution to higher intensities has been obtained by the chirped pulse amplification technique [17], where a short pulse is stretched in time in order not to destroy the related optics, then amplified and at the end compressed to the original pulse length. Using this technique short ultra-intense laser pulses with an intensity of up to $10^{21}\mathrm{W/cm^2}$ [18] have been achieved so far. Highly non-linear effects covering quantum interferences like tunneling or spin effects have been investigated with these kinds of relativistic intensities. Review articles on this topic can be found in [19].

Before characterizing the laser intensity in different regimes the most interesting phenomena in the area of atom laser interaction will be briefly reviewed. We especially focus on the ionization dynamics. A bound electron can be ionized by absorbing many photons,

whose single energy is lower than the required ionization potential energy. This process is named multiphoton ionization. In case of above-threshold ionization the electron absorbs more photons than required to reach the continuum and return to its origin. In case of small laser frequencies and together with strong laser fields the electron can simply leave the atom via tunneling. After the electron leaves the atom by any of the aforementioned possibilities it can return to its origin. For the recollision scenario three different situations are possible. Firstly, the electron recombines with the ion emitting its energy plus the ionization energy as a photon, which leads to high harmonic spectra. Secondly, the electron can inelastically scatter off the ion and release a second electron known as non-sequential double ionization. Thirdly, it may scatter elastically acquiring drift energies much higher than otherwise.

The interaction of atoms with laser frequencies in the optical domain can be distinguished in the following three main parts. For a laser intensity below 10^{16} W/cm^2 the interaction is non-relativistic. In this regime the laser electric field component dominates the interaction in comparison to the magnetic field component and therefore the electron motion takes place mainly in the polarization direction. In the intermediate intensity regime of 10^{16}-10^{18}W/cm^2, relativistic corrections of the order of (v/c) start to be of importance, with the electron velocity v and the speed of light c. These first-order effects and higher-orders can be calculated by a Foldy-Wouthuysen transformation of the Dirac-Hamilton operator, which summarized, is a transformation to decouple the Dirac equation into two two-component equations. In this intensity domain, the magnetic field component of the laser field needs to be considered and the dipole approximation (ωt -$\mathbf{kr} \approx \omega t$) starts to break down, where $\mathbf{kr}$ characterizes the laser wavefront, ω the frequency and t the interaction time of the laser field. The full relativistic dynamics comes into play for intensities above 10^{18}W/cm^2.

The atomic field strength in multiply charged hydrogen-like ions can compensate depending on their ionic core charge these ultra-intense laser fields. The strongest laser intensity of 10^{22}W/cm^2 [20] achieved today can be e.g. compensated by a hydrogen-like ion of charge $Z = 10$. The applicable intensity regime for perturbation theory is below 10^{14}W/cm^2. Above this domain high-order effects are essential and non-perturbative ap-

proaches are needed to describe them, which belong to the subject of strongly pertubated quantum systems.

In general, analytic solutions of single-atom responses in these intensity regimes are difficult to obtain, as temporal and spatial effects have to be considered, forcing the development of numerical methods. However, even the simplest investigation of an electron in hydrogen, applied to an intense laser field presents a great numerical challenge for the numerical work. Therefore, a variety of compromises concerning the modeling of real systems have been made. A numerically calculated wavefunction provides information about the details of time-dependent phenomena like ionization or the population dynamic of the atomic ground state and any other excited state considered in the calculation. To include relativistic effects of ultra-strong laser matter interaction as well as not to be restricted by several approximations, the numerical solution of the Dirac equation offers a promising prospect as the wave packet dynamics of the interaction can be adequately investigated, as done in this thesis.

The aim of this thesis is to generally contribute to a better understanding of highly nonlinear processes in relativistic laser-ion interaction. In particular we developed a novel method to sensitively measure and better characterize ultra-strong laser intensities from the optical to the UV and beyond towards the XUV frequency range. Our method is especially important as its realm of viability extends into a laser intensity regime in which conventional methods are simply not feasible. The selective use of multiply charged ions, taken such that their atomic field strength is on average comparable to that of the laser field, renders them applicable to a wide range of laser intensities both presently available and in the future. This specific characterization of ultra-strong laser fields is particularly important for the forthcoming aim to investigate laser-matter interaction in the ultra-relativistic regime. For the bound dynamics regime the determination of multiphoton transition matrix elements via Rabi oscillations in multiply charged hydrogen-like ions has been examined. This is of broad interest as the radiation from these transitions have an application as a tunable table-top source in the XUV and soft X-ray regime and because in this way ionic transition matrix elements may be probed.

In chapter 2, the fundamental processes of the ionization and bound dynamics regime will be introduced. A special focus lies on the non-relativistic and relativistic ionization interaction giving a diagram of the importance of magnetic and relativistic effects as a function of the field frequency and intensity for various ionic core charges Z. Moreover, the bound dynamics section concerns multiphoton transition processes within the dipole approximation and beyond. This chapter finishes with a general overview of some of the characteristic properties of multiply charged ions. Proceeding with chapter 3, we specify the used numerical models for the simulation of the interaction of the laser field with multiply charged hydrogen-like ions. These comprise a classical relativistic Monte-Carlo simulation and the solution of the Dirac equation in two dimensions. For the latter we have generated the energy eigenstates together with their associated wavefunction for several multiply charged ions by using the spectral method. Moreover, the two-dimensional eigenstates are characterized by determining their angular momentum and parity. The dynamics of the generated wavefunction via the interaction with the laser pulse is calculated by the split-operator method as explained within this chapter.

The focus of chapter 4 is on the ionization dynamics of multiply charged hydrogen-like ions in ultra-intense laser fields. In the first part we investigate the regime of validity of the analytically calculated tunnel rate formula for the non-relativistic laser-atom interaction and in the relativistic laser-ion interaction via the solution of the classical relativistic equation of motion. In the second part a most sensitive measurement of ultra-strong laser intensities is proposed by studying the ionization fraction of the considered interaction with multiply charged ions. The method is based on the compensation of the laser field by the atomic field strength of the chosen atomic species. This includes the investigation of the dependence on the typical laser parameters: frequency, pulse length, shape and phase. In addition to the ionization fraction, the ionization angle has been studied by both the classical relativistic and the quantum Dirac calculation. Our study of the measurement of ultra-strong laser fields permits in the optical frequency regime the characterization of laser intensities of up to $10^{26}\mathrm{W/cm}^2$ and is even applicable in the XUV frequency regime e.g. for the in the near future scheduled XFEL laser source.

Beyond the ionization dynamics of multiply charged ions the bound dynamics in chap-

ter 5 has been examined. In this case, the external laser field strength has to be below the atomic field strength to diminish the ionization probability. Thereby multiphoton transitions with the aim to determine the associated dipole transition matrix elements beyond the usual dipole approximation of the laser field have been studied, by investigating the Rabi frequency of the population dynamics. In the associated radiation spectra these transitions have been identified.

Throughout this thesis, if not stated otherwise, atomic units (a.u.) are used ($\hbar$=m_e=e=1) with electron charge e and mass m_e.

Chapter 2

Fundamental aspects of the dynamics of laser-matter interaction

In this thesis we deal with the interaction of atomic/ionic systems in the presence of an external laser field. In particular, we investigate two main branches of interaction types, namely the ionization dynamics, where the laser field strength is of the order of the atomic field strength or beyond and the bound dynamics with a laser field strength well below the atomic field strength. The regime of interest of ultra-intense laser intensities $I = 10^{18} - 10^{26}\mathrm{W/cm^2}$ allows the study of the quantum dynamics of the electron in the relativistic regime. The current maximum peak laser intensity achieved of the order of $10^{22}\mathrm{W/cm^2}$ [20], lies well within this regime and shows the increasing interest in the field of relativistic dynamics.

The relativistic character of the electron originates from two sources. Firstly, if the velocity of the electron approaches the speed of light c, originate by the acceleration of the laser field, relativistic effects become essential including the relativistic mass shift and the spin-orbit coupling. These effects depend on the intensity of the applied external laser field which increases the velocity of the electron due to acceleration. Secondly, in multiply charged states, the deeply bound electrons move in the binding potential with velocities close to c, causing relativistic effects in the bound state wavefunction. The acceleration of the electron to velocities close to the speed of light after leaving the atomic core is of main importance for the ionization dynamics, whereas the relativistic modification of the wavefunction of the ionic core charge state is essential for the bound dynamics.

One of the main topics to be addressed in this thesis, is the relativistic laser-matter interaction, related to ionization (chapter 4). The relativistic context in this system arises from ultra-strong laser fields in the optical frequency domain, which are applied to hydrogen-like multiply charged ions. Although the Coulomb force of the ion potential is quite strong, when the electron leaves the vicinity of the ionic core of charge Z, it has a non-negligible velocity compared to the speed of light. Furthermore, we examine the bound-bound dynamics in multiply charged ions (see chapter 5) which involves a relativistic treatment. Here, the high velocity v of the bound electrons in the multiply charged ion ($v \sim Z$) requires us to cast the problem relativistically.

2.1 Ionization dynamics

In the early stages of the generation of laser light in the optical regime, the intensity was very limited. Hence, the analysis of the laser-atom interaction by laser intensities below $10^{15}\mathrm{W/cm^2}$ in the optical regime could be treated by perturbation theory, where the laser field is treated as a small perturbation to the atom. The validity of the application of perturbation theory is provided if the perturbation term $\mathbf{E} \cdot \mathbf{r}$ is small compared to the photon energy ω. Here, E is the laser field strength and r is of the size of the typical Bohr radius a_0 of the system. In the case of a strong electric field, which deforms the atomic potential, the perturbation treatment of the problem is not valid anymore. In this case, we enter the regime of strong fields, which needs to be treated differently as described in the following.

Analytical models describing the strong laser-atom interaction were given in the early 1960s and late 1970s by the famous work of Keldysh (1965), Faisal (1973) and Reiss (1980) [21–23], who successfully developed a framework of the strong-field phenomena by introducing the strong field approximation (SFA). The fundamental idea behind this approximation for laser-induced ionization processes is to neglect the Coulomb potential of the ionic core once the electron is detached by the laser field and vice versa to disregard the influence of the laser field on the deeply bound electrons. However, an electron can be directly ejected in the applied laser field through the absorption of multiple photons,

known as multiphoton absorption. The behavior of the electron after it leaves the ionic core (ionization) can be described classically by the so-called recollision model, first proposed by Corkum [24]. The assumption made for the classical description of the electron in this model, is the zero velocity of the electron during ionization. Once the electron is liberated from the ionic core it propagates in the laser field accumulating energy from it. When the electric field changes sign the electron can be accelerated back (depending on the ionization time) and recollide with the ionic core. This recollision process can either lead to a rescattering of the electron, in which the associated rescattering energy and further structures are manifested in the above-threshold ionization (ATI) spectrum [25], or else it can recombine and radiate multiples of the laser frequency, which is generally known as the process of high harmonic generation (HHG) [26]. If there is more than one electron involved in the process of recollision, the electron's energy is employed to set free further electrons. This process is known as non-sequential ionization [27]. The simple recollision model allows us to describe qualitative features in the regime, where the laser field dominates the interaction. For example, the calculation of the exact cutoff energy of the HHG and ATI spectrum, the plateau structure in the HHG spectrum and the peak separation by the photon frequency in the ATI spectra were carried out.

The physical process of ionization can be distinguished between three main processes see Fig. 2.1, over-the-barrier ionization (OTBI), tunnel ionization (TI) and multiphoton ionization (MPI). The classification between these different ionization processes is usually done by the generalized Keldysh parameter $\gamma = \sqrt{2I_p}\omega/E$ for a hydrogen atom, where I_p is the ionization potential of the atomic species, ω the laser field frequency and E the laser field amplitude. This can be extended for arbitrary ionic charges Z under consideration of the ionization potential as $I_p = Z^2/2$, to $\gamma = \frac{Z\omega}{E}$. The Keldysh parameter behind this definition can be understood as the ratio of the tunnel time to the time the laser field needs to change its direction (see also the extension for the relativistic case in section 2.1.2). For a Keldysh parameter of $\gamma > 1$ (*multiphoton ionization* regime) bound-free transitions can be described perturbatively. The ionization in this regime takes place via simultaneous absorption of N, $N+1$, $N+2$, ... number of photons, i.e. $N\omega > I_p$ has to be fulfilled, whereas N is the smallest photon number to overcome the ionization potential

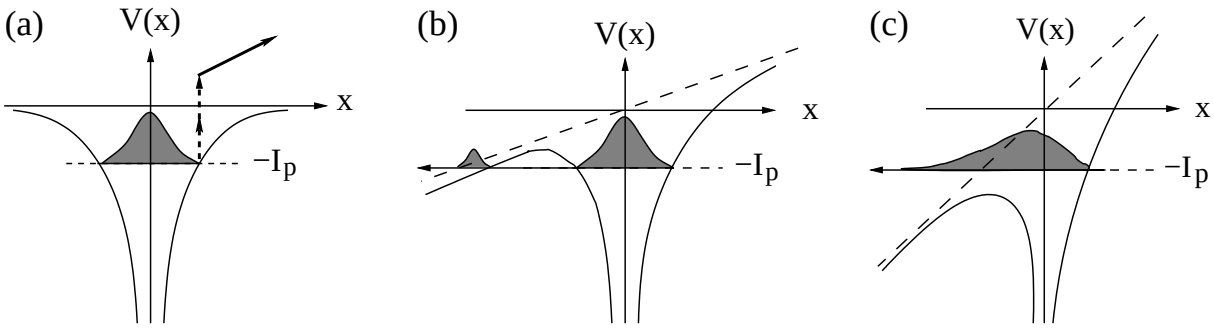

Figure 2.1: Schematic diagram of the different ionization mechanisms, namely the multiphoton ionization (a), tunnel ionization (b) and over-the-barrier ionization (c). Shown is an effective potential (solid line) in one dimension, which is a superposition of the Coulomb potential and a static electric field (dashed line). Additionally, the ionization potential I_p and a bound state wavefunction, marked by the shaded Gaussian-like profile has been added.

I_p. For $\gamma < 1$ the effective field consisting of a superposition of the laser field and the atomic Coulomb potential is modified in such a way that the electron can tunnel through the potential barrier, leading to quantum mechanical *tunnel ionization*. For even stronger laser fields, the Coulomb barrier is so strongly suppressed that the electron can classically leave the ionic core, which is known as the regime of *over-the-barrier ionization*. In this case, the escape rate adiabatically follows the variation of the optical laser field.

The theories of intense laser-matter interactions have been further developed over the years to include the description of different ionization processes e.g. by many-body S-matrix theory [28], full classical theory [29] and density functional theory [30]. Even semi-analytic non-perturbative approaches work principally, but the solutions of these are extremely difficult to obtain and unreliable for ultra-intense laser intensities. In addition to the analytical models, including relativistic laser-matter interaction, numerical codes have been developed in order to investigate the interaction dynamics in a more accurate way. A further advantage of them is that no assumptions about the frequency range or intensity range of the laser have to be made. Likewise, the pulse type and shape can be chosen freely. Despite the advantage of accurate calculation using numerical integration techniques, the computationally intensive codes require some approximation, to reduce the amount of computation time. The bottleneck in numerical algorithms, especially in the Dirac equation solver, is the large number of time steps needed for the calculation.

The reason is the intrinsic energy time uncertainty relation, where the energy contains the large rest mass of the electron in case of the Dirac equation, which has to be temporally resolved. A decrease of the associated computation time of these kind of calculations is accomplished by a reduction of the number of physical dimensions. In the early stages, simulations have been performed for linear polarized laser fields in one dimension using the Schrödinger equation. The general basis of the numerics, is to discretize the time-dependent wavefunction on a grid by using the finite difference method (see appendix A). The one-dimensional calculations are generally sufficient to look at, e.g. the fundamental structure of a high-harmonic spectrum. However, they do not provide any information for circular polarized light or take magnetic field effects into account. This can already be seen from a classical analysis of the equation of motions of the Lorentz force given in atomic units.

$$\frac{\mathrm{d}}{\mathrm{dt}}\mathbf{p} = -[\mathbf{E}(\eta) + \frac{\mathbf{v}}{c} \times \mathbf{B}(\eta)] \,, \tag{2.1}$$

with $\mathbf{p} = \tilde{\gamma}\mathbf{v}$, where $\mathbf{v}$ defines the velocity of the electron, $\tilde{\gamma} = (1 - \boldsymbol{\beta}^2)^{-1/2}$ and $\boldsymbol{\beta} = \mathbf{v}/c$. We consider a laser pulse linearly polarized in x-direction, propagating in the z-direction with $\mathbf{k} = k\mathbf{e}_z$, with $k = \omega/c$. Thereby, the parameter η is defined as $\eta = \omega t - \mathbf{kr} = \omega(t - z/c)$. If we neglect all the terms of the order of v/c, the resulting electron motion is one-dimensional in polarization direction x:

$$\frac{\mathrm{d}}{\mathrm{dt}}v_x = -\mathrm{E}(\omega t) \,. \tag{2.2}$$

If one keeps the first order in v/c, the electron motion becomes two-dimensional in the (xz)-plane, with

$$\frac{\mathrm{d}}{\mathrm{dt}}v_x = -\mathrm{E}(\omega t) \,; \qquad \frac{\mathrm{d}}{\mathrm{dt}}v_z = -\frac{v_x}{c}B(\omega t) \,. \tag{2.3}$$

These simple considerations lead to a division of the electron motion in a non-relativistic and a relativistic regime, which will be explained below.

2.1.1 Non-relativistic laser-atom interaction

In the non-relativistic laser-atom interaction regime the electron velocity is much smaller than the speed of light c. In this case the spatial dependence of the phase $\eta = \omega t - \mathbf{kr}$ in

the electric field E can be written as $\eta \approx \omega t$. This approximation of the electric field is the so called dipole approximation $a_0/\lambda \ll 1$, where a_0 is the Bohr radius and λ the laser wavelength. A second condition for the use of the dipole approximation is $E/\omega \ll c$. In both cases the magnetic component of the laser field can be ignored in the evolution of the wave packet dynamics. In the case of free electron motion in such a laser field, the electron oscillates only in the laser polarization direction. The latter will be compared with the case where the magnetic field of the laser is not negligible.

The simplest system of study is the investigation of the dynamics of a free electron, showing a typical zigzag motion [31] as depicted in Fig. 2.2 for various field strengths. The drift of the electron in propagation direction is due to the coupling of the laser field to the magnetic field of the moving electron, increasing with laser intensity for a fixed frequency.

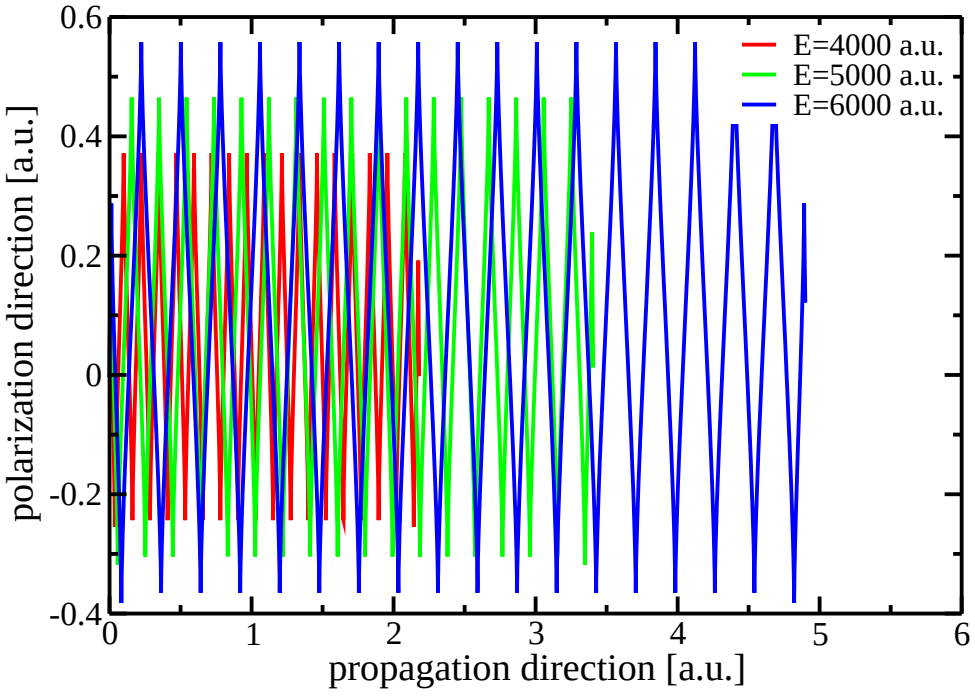

Figure 2.2: Typical zigzag motion of a free electron starting at rest for various field strengths in an external laser field with a frequency of $\omega = 114$ a.u. ($\lambda = 0.4$ nm) in the plane of the laser polarization x and propagation z direction. The pulse consists of 20 cycles including 2 cycles of turn-on and turn-off phases. Apart from the oscillation in laser polarization direction a clear drift in laser propagation direction is visible, increasing with field strength.

Due to the above mentioned assumptions the laser-driven matter interaction in the non-relativistic regime can be calculated either analytically or numerically by solving the Schrödinger equation. Especially for laser intensities below $10^{16}\mathrm{W/cm^2}$, a variety of investigations of the laser interaction with atoms [32], molecules [33], clusters [34] and solids [35] have been performed in the past. However, when the electron is accelerated to velocities close to the speed of light, relativistic effects become important and the magnetic field component of the Lorentz force can no longer be neglected. Since optical laser fields of intensities of the order of $10^{21}\mathrm{W/cm^2}$ become nowadays available, investigations of the relativistic dynamics become popular. An overview will be given in the next section.

2.1.2 Relativistic laser-ion interaction

For laser intensities of the order of $10^{18}\mathrm{W/cm^2}$ the interaction of the atom with an external laser field is in the relativistic regime in which the electron velocity approaches the speed of light. To account for the full relativistic effects of the dynamics in this regime the calculation of the Dirac equation is the unique choice.

Relativity can be expressed by the parameter $\xi = E/\omega c$ for neutral atoms, where E and ω are the laser field strength and frequency, respectively. The interaction is relativistic when ξ approaches 1, i.e. the laser field provides the electron with energy that equals its rest energy. The distinction of the different ionization regimes via the Keldysh parameter γ modifies in the relativistic case to

$$\gamma_{rel} = \frac{\omega}{E}\sqrt{1-\epsilon^2} \tag{2.4}$$

with $\epsilon = \sqrt{1-(Z\alpha)}$ for the ground state of an arbitrary ionic core of charge Z and $\alpha = 1/c$. As will be discussed in the ionization dynamics section relativistic effects become important at ionic core charges above $Z = 10$.

After having defined our relativistic regime we will now look at the typical trajectories that occur. As mentioned in the previous section, magnetic field effects become important in the relativistic regime as the classical magnetic field component of the Lorentz force cannot be neglected. Rather, the magnetic field component of the linearly polarized laser field induces a drift of the electron in laser propagation direction, in addition to the oscillatory

motion in the laser polarization direction, which renders the motion two-dimensional.

In the following, an overview is given regarding the range of importance of magnetic field effects and relativistic effects [36]. When an atom/ion is subjected to an intense laser field photoelectrons with relativistic energies can be produced. In this case the dipole approximation is no longer valid and the magnetic field of the laser needs to be taken into account. With the solution of the classical relativistic equation (2.1) of the free electron the extension of the maximum excursion amplitude in laser propagation direction x of the zigzag motion (Fig. 2.2) can be approximated by

$$\begin{aligned} \frac{|x|}{\lambda} &= \frac{1}{2\pi}\zeta/8 = \frac{\zeta/8}{c/\omega\lambda} \\ \zeta &\equiv \frac{2z_f}{1+z_f} \end{aligned}$$

The intensity parameter z_f is defined as $z_f \equiv 2U_p/c^2$. The above calculated excursion amplitude of the figure of eight motion (which an in laser propagation direction moving observer sees) of a free electron is modified in case of a binding potential with the Bohr radius a_0 by

$$\frac{|x|}{a_0} \approx (z_f/4)(c/a_0\omega)\ . \tag{2.5}$$

Therefore, the width of the figure-of-eight becomes equal to the diameter of the Bohr atom when $z_f = 4a_0\omega/c$. In terms of the intensity parameter $z' = U_p/\omega$ with the help of $z_f \equiv \frac{2U_p}{c^2}$, z' can be expressed as $z' = 2a_0c \approx 275$, which is proportional to the ratio of twice the Bohr radius to the Compton wavelength $\lambda_c = 2\pi/c$. The magnetic field strength can be regarded as important when z' is bigger than 1% of its value, i.e. $z' \geq 2.75$. For several atomic core charges Z the importance of the magnetic field is depicted in Fig. 2.3. Apart from magnetic field effects, relativistic effects can be estimated by the intensity parameter z_f. They become important for $z_f \approx 0.1$, which is depicted in Fig. 2.3 by the upper line. Both estimations can be generalized for any atomic core charge Z and give the regime of the associated important effects as a function of the laser intensity and frequency. To conclude, in the intensity domain indicated by the lower line of Fig. 2.3, v/c effects of the magnetic field in the laser interaction with atoms have to be considered. True relativistic effects of the order of $(v/c)^2$ are important above the upper line in Fig. 2.3.

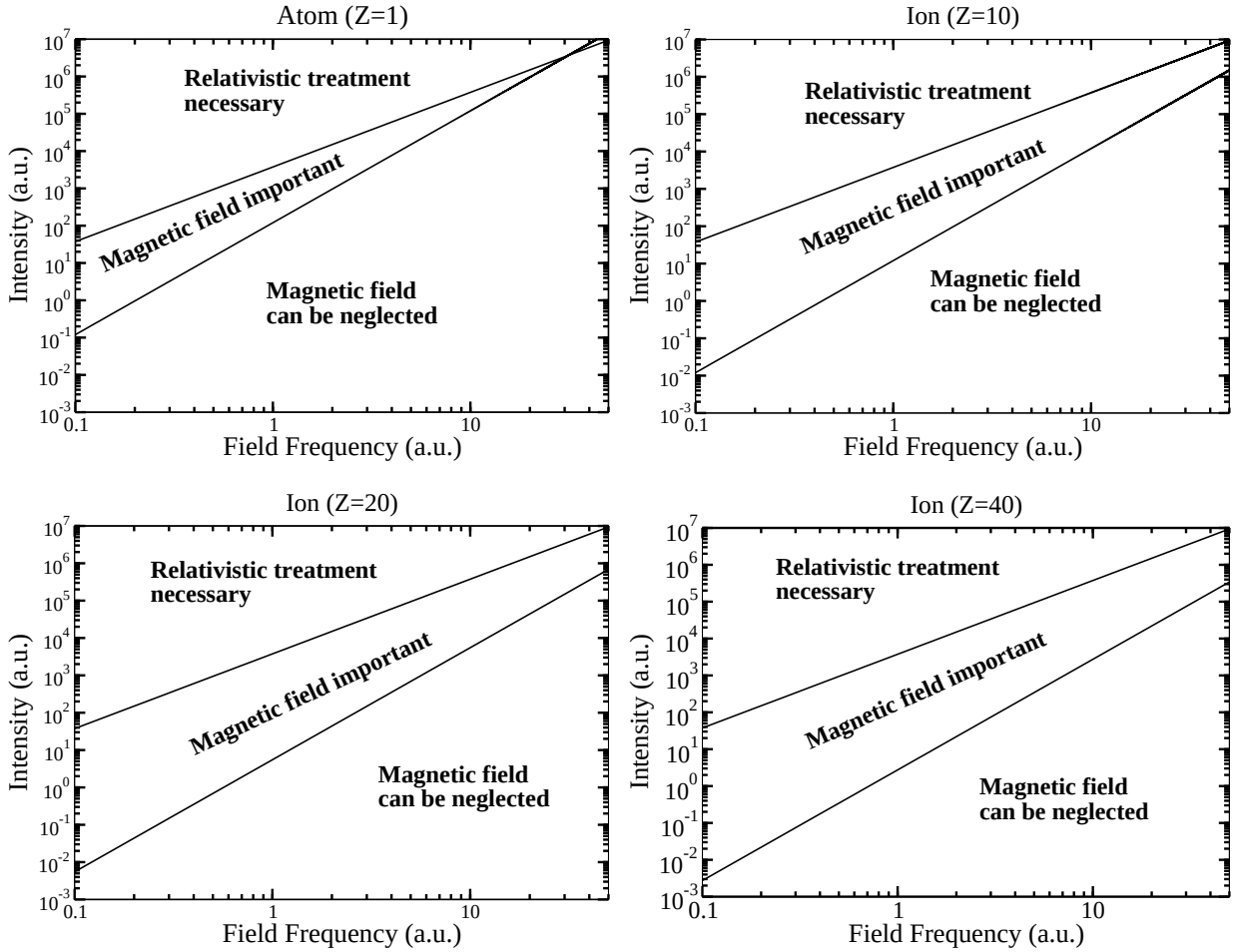

Figure 2.3: Plotted are the regime of importance of magnetic field effects and relativistic effects in case of an atom ($Z = 1$) and for the ionic core charges of $Z = 10$, 20, 40. Magnetic effects are important above the lower line, whereas relativistic effects have to be taken care of above the upper line.

Novel features, beyond the dipole approximation of the intense laser-atom interaction, appear in two-dimensional calculations as the influence of the spatial dependency of the vector potential is taken into account, forcing the electron trajectory on a two-dimensional plane. This is essential for the numerical study of the relativistic laser-matter interaction with the help of the Dirac equation as carried out in this thesis. If one keeps the dimensionality, the computer load is dramatically increasing. To achieve a proper computation time the pulse length has to be decreased in order to minimize the interaction time, which is only feasible within the limit of high frequencies. Another option is to use absorbing boundary conditions, so that the ionized wavepacket is removed and cannot be reflected at the border of the grid. The advantage is that one can reduce the spatial size of the grid and thus, limit the computation time. This leads to a decrease in the normalization of the wavepacket, which in turn can be used as a quantitative measure of the ionization rate. The relativistic laser-matter interaction concerning the bound dynamics will be introduced in the next section.

2.2 Bound dynamics

A problem that quickly arises in the bound dynamics regime for relativistic laser parameters is the large ionization probability of multiphoton ionization of the bound electron. To be still able to investigate relativistic bound dynamics we make use of multiply charged ions. The attractive Coulomb force ($E_{at} \sim Z^3$) in multiply charged ions can be chosen such that, the electron can withstand e.g. relativistically strong near-optical pulses. In these ions the first Bohr orbit of the electron is inversely proportional to the atomic charge Z resulting in a much stronger bound electron compared to the case of the hydrogen atom. These aforementioned characteristics of multiply charged hydrogen-like ions in the field of ultra-strong lasers, renders this regime of interaction a very interesting and promising one to study, as the occurring dynamics will be governed by relativity. The leading relativistic corrections to a non-relativistic treatment of the laser-matter interaction dynamics are the magnetic field component of the laser, the spin-orbit coupling and the relativistic mass shift.

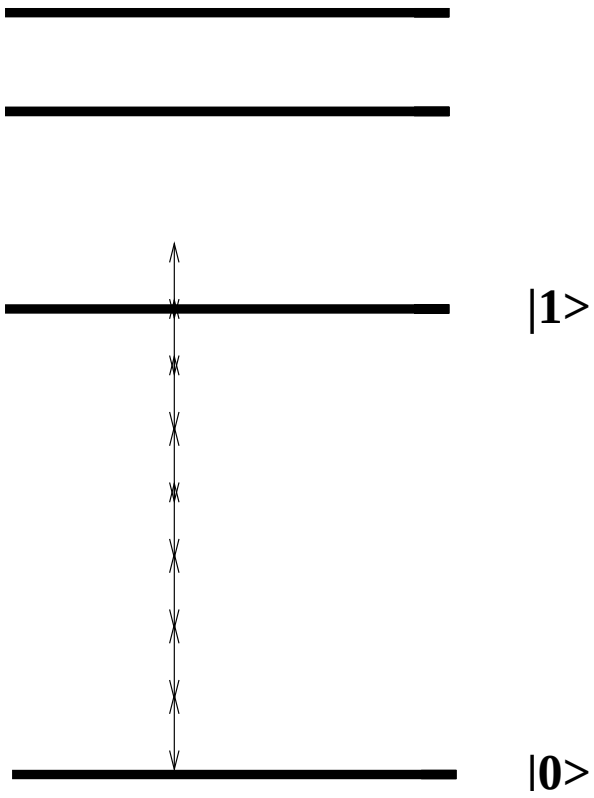

Figure 2.4: Schematic diagram of a resonant multiphoton transition in multiply charged hydrogen-like ions, where each two-ended arrow indicates one photon.

One typical feature of highly charged ions are their widely separated eigenstates. They can be coupled via multiphoton transitions as depicted in Fig. 2.4. The radiative emission from these transition are e.g. in the favorable high-frequency XUV range. An important application of these XUV frequency transitions is e.g. a higher resolution in the frequency domain interferometry, which is used for probing, manipulating and controlling ultrafast phenomena.

2.2.1 Dipole/Non-dipole interaction

In the following, we focus on the time evolution of the electronic wave packet within and beyond the dipole approximation. The dynamics of the center-of-mass motion is in both cases displayed in Fig. 2.5 for an ionic charge of $Z = 30$. The electron wave packet dynamics of the solution of the time-dependent Dirac equation in two dimensions is given by the spatial expectation value of the laser polarization and propagation direction of

the related wave packet. In the case of a free electron we have already seen the zigzag motion in laser propagation direction. For a laser field strengths well below the atomic field strength of $E_{at} = 27000$ a.u. ($I = 2.5 \times 10^{25}\mathrm{W/cm^2}$) in case of an ionic core charge of $Z = 30$, the atomic field of the ionic core seriously competes with the drift imposed by the laser field. This drift motion in laser propagation direction can be seen together with an oscillation of the electronic wave packet around the ionic core in Fig. 2.5, showing the importance of the laser magnetic field component.

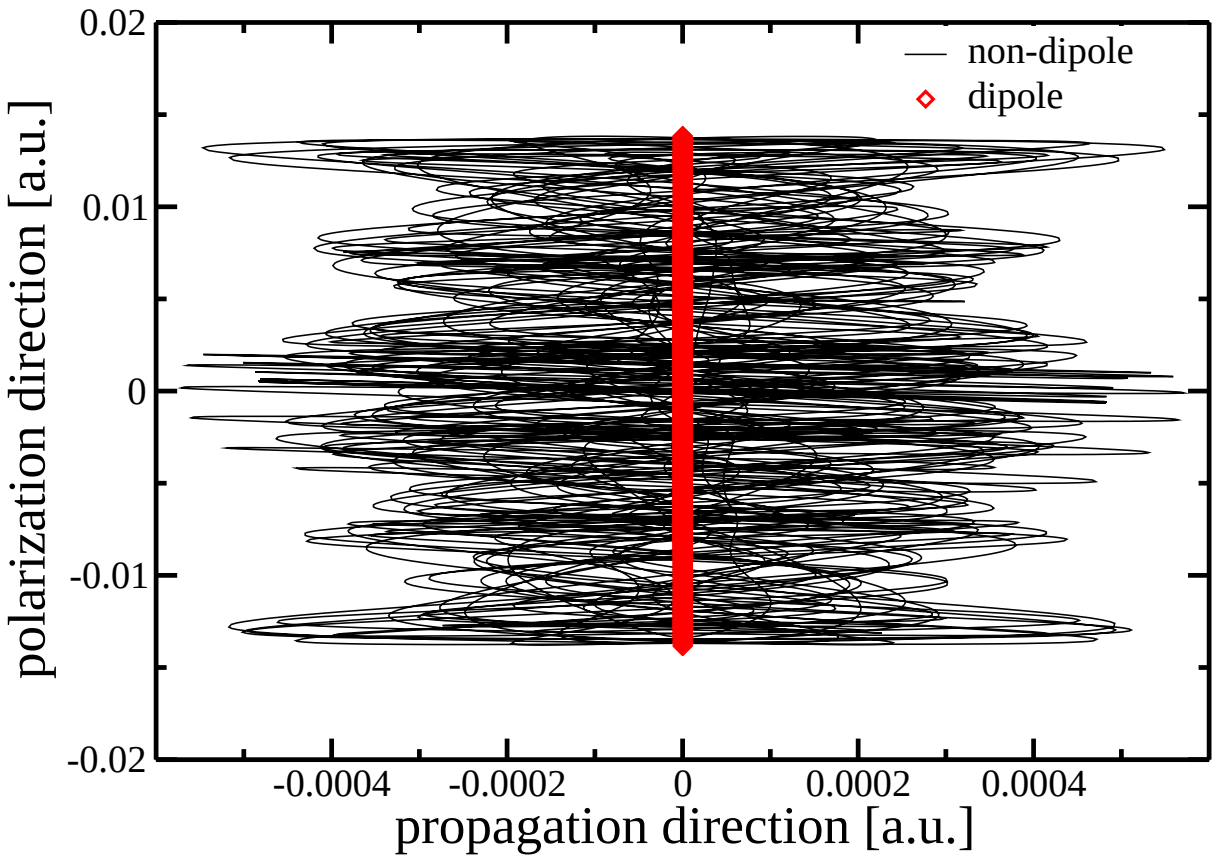

Figure 2.5: Center-of-mass motion of a bound electron in an external laser field in the plane of laser polarization direction x and propagation direction z for a laser field strength of $E = 18000$ a.u. ($I = 1.14 \times 10^{25}\mathrm{W/cm^2}$) and a frequency of $\omega = 114$ a.u. ($\lambda = 0.4$ nm). These parameters have been used in case of a 20 cycle pulse with 2 cycle turn-on and turn-off ramp, respectively and an ionic core charge of $Z = 30$. The diamonds display the center-of-mass motion within the dipole approximation, where the magnetic field component of the laser field is neglected. The solid line shows the entire center-of-mass motion in the case the magnetic component of the laser field is included in the calculation.

In Fig. 2.6 the center-of-mass motion of the wave packet of a bound electron for different ratios of the laser field strength E to the atomic field strength E_{at} of an ionic charge $Z = 30$ is shown. For all the ratios of E to E_{at} the electron motion has a component in laser propagation direction as well as in the laser polarization direction. In case of a laser field strength below the atomic field strength, the drift in propagation direction per laser cycle is small in comparison to a field strength above the atomic field strength. In the case of $E/E_{at} = 0.8$, the electron motion goes mainly in the negative laser polarization direction due to the Coulomb attraction of the nucleus compared to the motion in positive laser polarization direction for the field strengths above E_{at}.

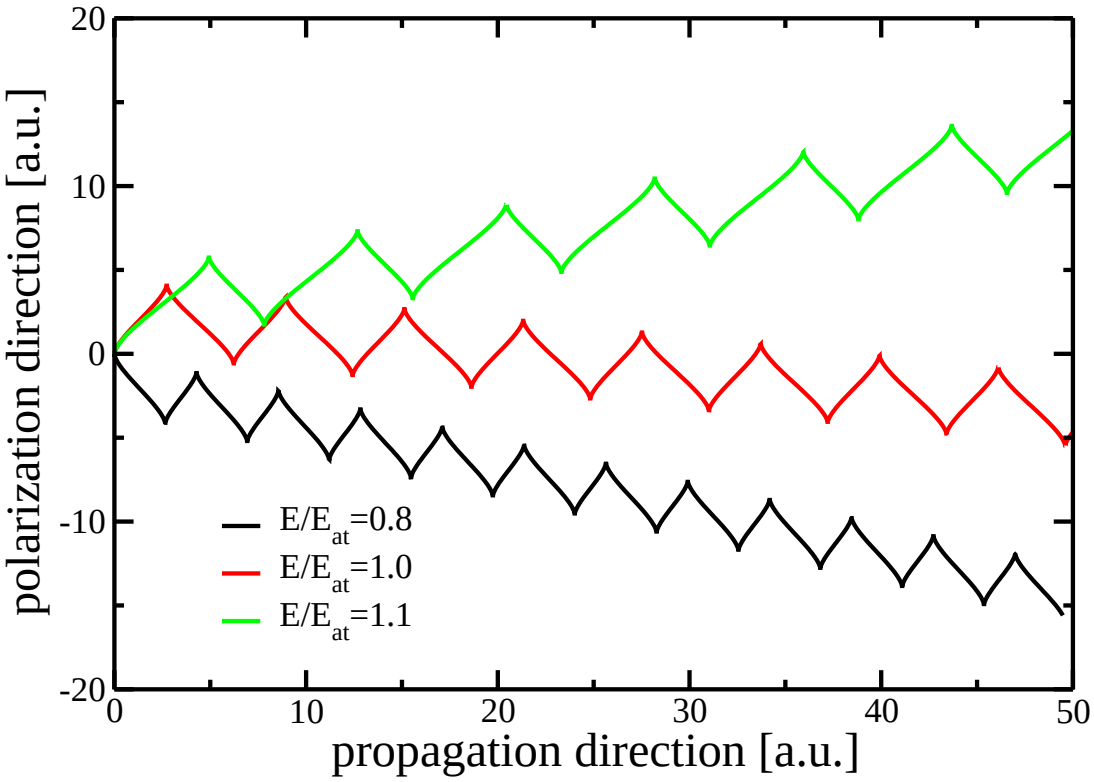

Figure 2.6: Center-of-mass motion in the plane of the laser polarization and propagation direction of a bound electron (in the ionic core charge of $Z = 30$) for different ratios of the laser field strengths E to the atomic field strength E_{at}.

2.3 Properties of multiply charged ions

Since the whole universe exists of multiply charged ionized matter, it is very interesting to look at the fundamental properties of multiply charged ions and their use in atomic physics. Today, powerful devices are available to produce any ionization stage of naturally occurring atoms [37].

A broad range of research with highly charged ions incorporates the radiation from highly ionized matter relevant in X-ray astrophysics [38]; for the investigation of the critical field strength for vacuum to become instable through a phase transition from a neutral state to a charge state by spontaneous generation of positron-electron pairs [39]; ion lithography, where the focused ion beam can produce structures of 8 nm size [40]; quantum computing by trapped ions [41]; as a diagnostic tool for conditions in fusion plasma and to efficiently treat tumors in the human body. The latter is possible by precisely directing the ion beam at the tumor target and to adjust the beam so that the beam energy is completely deposited inside the tumor target with relatively little damage to the healthy surrounding tissue.

In the following some of the important properties of multiply charged hydrogen-like ions will be specified. The Bohr radius of the groundstate wavefunction of an multiply charged ion is inversely proportional to the ionic core charge Z ($R \sim 1/Z$). In case of ionic core charges above $Z \sim 50$ the electron wavefunction has an overlap with the nucleus wavefunction and therefore the spatial density distribution is proportional to Z. One essential outcome is parity violation. The short-range interaction between the electron and the nucleus is then determined by the exchange of massive Z vector bosons. These kind of processes are not regarded here.

The potential energy of multiply charged ions can be distinguished in ionization energy and neutralization energy. To clarify the difference between them, the ionization energy is the energy which is necessary to remove one electron from the atom to produce the charge of Q+1 out of the charge Q. The potential energy is given by $U(Z) \sim Z/R = Z^2$. The ionization energy is an important quantity for the production of highly charged ions, where one electron after the other is removed. Under the term neutralization energy we

understand the energy which is set free when all electrons are removed from the atom. This quantity is usually relevant for the influence of ions on surfaces.

Another important form of energy is the photon energy. It is defined as the energy between two different eigenenergies and can be used to determine the wavelength of the emitted light of such a transition. However, the main contribution for the transition between different neighboring states derives from the Coulomb potential and leads to a scaling of the energy by Z^2. Transitions considering the fine structure of the energy levels scales like Z^4. This can be understood semiclassically, arising from the magnetic dipole interaction of the electron spin with the magnetic field caused by the electron motion through the electric field of the nucleus. The associated magnetic field is proportional to the vector product of the nuclear Coulomb field and the electron's velocity. One step further in the interaction contribution is the hyperfine structure, where the energy levels scales like Z^3. Here, the origin of the shift arises from the interaction of the electron magnetic moment with the magnetic moment of the nucleus. These scaling laws shows the range of energy splitting of the associated electronic structure of the related ionic charges, measurable with high-resolved laser spectroscopy.

Chapter 3

Model system and numerical approach

3.1 General framework

The interaction of the laser field with matter covers the study of individual atoms up to complex systems like plasma. To gain a deeper insight in the relativistic laser-plasma field, investigations of collective multi-particle dynamics [42], fission, fusion and nuclear processes [43] have been carried out.

In this thesis two main fields of light-matter interaction are dealt with, namely the ionization dynamics (chapter 4) and the bound dynamics (chapter 5) of the "active" electron in multiply charged hydrogen-like ions. The atomic field strength of multiply charged hydrogen-like ions scales with the ionic core charge of Z^3. In case of a hydrogen atom ($Z = 1$) the atomic field strength for an electron on the first Bohr orbit is 1 a.u. $= 5.14 \times 10^9$ V/cm. The bound dynamics regime is then defined by a laser field strength well below the atomic field strength of the given ion, whereas in the ionization dynamics regime the laser field strength is in the order of the atomic field strength or well above.

In principle, multi-electron charged ions can be calculated as well, if the single-active electron approximation is applied. Hence, it is assumed that the response of the atom is entirely dominated by the dynamics of a single electron in the multiply charged ion system.

Nowadays, the preparation of multiply charged ions of any specific charge Z can be

accomplished with both high density and purity. One possibility of generating them is by sending the related atom through thin foils as discussed in [44]. Another method is due to the help of lasers considered in e.g. [45] through which most of the outer electrons are stripped away by the rising edge of the pulse. This kind of interaction produces multiply charged ions along with very energetic electrons [46]. The absolute charge state achievable is limited to a charge of about $Z = 40$ because of the broad distribution of the different multiply charged ions in the time of flight spectrum. Another problem are the not yet available ultra-strong laser intensities for the actual production of hydrogen-like ions above $Z = 40$. In the following, we are going to investigate the numerical generation of the eigenenergies and associated wavefunctions of multiply charged hydrogen-like ions.

3.2 The Dirac atom in 2D

Before looking at the dynamics of the electron wavefunction in different situations, the generation of the wavefunction with the associated energy eigenstates will be described in the following chapter, in the case of two dimensions. To reduce the number of dimensions from three to effectively two (the third dimension being a constant) is necessary in order to numerically handle the atomic system with the help of the Dirac equation. Reasons for this will be given in the proceeding sections.

3.2.1 The soft-core potential

In three dimensions the interaction of the electron with the nucleus is modeled by a pure Coulomb potential, whose energy eigenstates are calculated via

$$E_n = c^2 \left[1 + \left(\frac{Z\alpha}{n - (j + 1/2) + \sqrt{(j + 1/2)^2 - (Z\alpha)^2}} \right)^2 \right]^{-1/2} . \tag{3.1}$$

Here Z denotes the charge of the atom, c is the speed of light, $\alpha = 1/c$ (in atomic units) is the fine structure constant, n refers to the main quantum and j is the quantum number of the total angular momentum in three dimensions. In general, there are only a few potentials that have an analytical solution.

For the numerical solution of the Dirac equation in two dimensions a potential is needed, which can adequately produce the proper bound energy eigenstates comparable to the three-dimensional case. This condition is satisfied by a soft-core potential, which is applied for the generation of wavefunctions and their associated bound states [47]. Although this potential has no analytical solution, it is a rather good approximation of the Coulomb potential in terms of the energy eigenstates and the associated wavefunctions, especially for small soft-core parameters a. The soft-core potential $U(x, z)$ in two dimensions is described by:

$$U(x, z) = -\frac{Z}{\sqrt{x^2 + z^2 + a}} \,. \tag{3.2}$$

The soft-core parameter a models the missing third dimension of the atomic potential and at the same time avoids the singularity of the Coulomb potential at its origin. In the definition of the soft-core potential, one has two degrees of freedom, viz. the charge Z of the atomic core and the soft-core parameter a. The charge Z has been fixed and the soft-core parameter a varied to match the ground state energy of the equivalent three-dimensional problem with the ground state energy of the soft-core potential Eq. (3.2). Having found the correct soft-core parameter of the energy ground state (see table in section 3.2.2), the higher excited states are then modified accordingly, as there exists no universal soft-core parameter that matches for all the energy eigenstates of the spectrum. The soft-core parameter has to be changed until the ground state energy of the three-dimensional analytically given solution Eq. (3.1) matches with the two-dimensional Coulomb potential calculation. For a fixed charge Z the energy eigenstates change to higher values with increasing values of a, as can be seen in Fig. 3.1. In table 3.1 some of the soft-core parameters for different charges Z are listed. The generation of the energy eigenstates of the soft-core potential is done via the spectral method as will be explained in the following sections.

3.2.2 The generation of energy eigenstates

The analytical calculation of the wavefunction of the Dirac equation given by a two-dimensional Coulomb potential goes back to the work of G. Mocken [48], who calculated

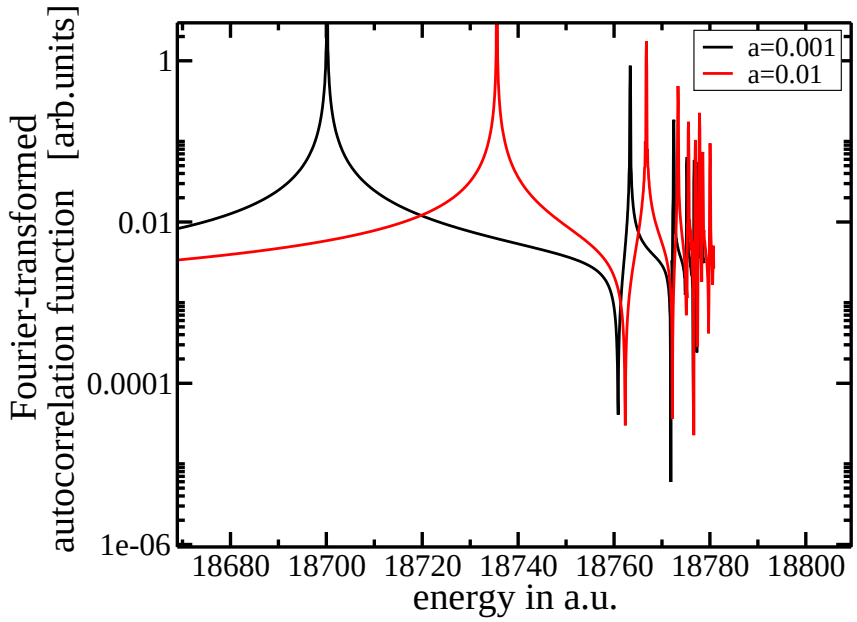

Figure 3.1: Depicted is a typical energy spectrum for the charge $Z = 10$ generated via the spectral method. For a fixed charge Z the energies are shifted towards lower values for smaller soft-core parameters a.

it for the general case of a Dirac spinor Ψ in three dimensions. Thereby, one dimension was treated as a constant, because of the chosen scalar potential which is invariant under translation in a particular direction. It remains an effective two-dimensional Dirac equation:

$$i\frac{\partial}{\partial t}\Psi(x,z,t) = \left\{c\boldsymbol{\alpha}\cdot\tilde{\mathbf{p}} + c^2\tilde{\beta} + U(x,z)\right\}\Psi(x,z,t)\ . \tag{3.3}$$

The four component Dirac spinor wavefunction is represented by $\Psi(x,z,t)$ with $\boldsymbol{\alpha}$, $\tilde{\beta}$ denoting the usual Dirac matrices, whereas the electron kinetic momentum is given by $\tilde{\mathbf{p}} = \mathbf{p} + \frac{1}{c}\mathbf{A}(z,t)$ with the canonical momentum $\mathbf{p}$ and the vector potential $\mathbf{A}(z,t)$. The

Table 3.1: Listed are the soft-core parameters a and the numerical properties, that are essential for the calculation of the wavefunction for a given ionic core of charge Z. The size of the numerical grid decreases because the electron orbit decreases as it is inversely proportional to Z.

charge Z	a	grid size in a.u.	spatial resolution
10	0.00625	8×8	256×256
30	0.00060	2×2	256×256
47	0.00016	0.5×0.5	256×256

numerical solution of this equation will be given in section 3.3.2. Other works [49, 50] calculated the Dirac wavefunction in two dimensions with complex spinors [1] Ψ .

The numerical calculation of the energy eigenstates and their corresponding wavefunctions is done via the spectral method, which is described in detail in the next section.

3.2.3 Spectral method

There are many methods known to numerically calculate the Dirac energy eigenstates in a known potential. Examples of these are inverse iteration [51], variation [52] or Monte-Carlo [53] techniques. For our calculations we have chosen the spectral method [54], based on the split-operator technique (section 3.3.2). From the numerical point of view, the generation of the energy spectrum in the Dirac case takes considerably longer compared to the Schrödinger case. The main reason for this is the energy-time uncertainty. In the case of the Dirac equation it means that the necessary time steps are considerably small, because the large rest mass of the electron has to be taken into account ($\Delta t < 1/E$). Additionally, for the Schrödinger equation, a faster converging algorithm for the generation of the energy spectrum exists, namely the method of imaginary time. Here the propagation time t is substituted by $\tau{=}it$ and the new propagation time τ is used for the repeated application of the stationary Hamiltonian. The new wavefunction converges then quickly to the state of lowest energy. Unfortunately, this method cannot be applied in the case of the Dirac equation as the lowest-energy state would converge into the negative continuum instead of into the lowest-energetic bound state in the positive continuum. Therefore, the proper soft-core parameter can only be determined by applying the spectral method brute force.

The procedure of generating the energy eigenstates of our two-dimensional model system with the time-independent Dirac Hamiltonian H

$$H\Psi = [c\boldsymbol{\alpha} \cdot \mathbf{p} + \tilde{\beta}c^2 + U(x, z)]\Psi = E\Psi \tag{3.4}$$

consist of the following steps. Firstly, an initial Dirac spinor test wavefunction is chosen to be numerically propagated in time and space, accomplished via the split operator method

[1] Calculation for the three-dimensional Coulomb problem is given in [55, 56]

(section 3.3.2). The energy spectrum is obtained by the Fourier transformation of the autocorrelation function $P(t)$ of the arbitrary test wavefunction for fixed Z and a. The autocorrelation function is generally defined by the scalar product of the wavefunction at different points in time

$$P(t) = \langle \Psi(t_M) | \Psi(t) \rangle \ . \tag{3.5}$$

Here $|\Psi(t_M)\rangle$ defines the wavefunction at the initial time t_M, which has to be implemented into the auto-correlation calculation, under consideration of eventually special symmetry of the to be generated wavefunction. To verify that the peaks of the energy spectrum are the eigenvalues of the stationary Dirac equation we expand the wavefunction $\Psi(t)$ into the bound eigenstates $\Psi(t) = \sum_{n,j} \varphi_{n,j} c_{n,j} e^{-i\vec{\sigma_3} t E_n}$, quantized along the σ_3 axis, where $\varphi_{n,j}$ are the functions of the bound energy states, $c_{n,j}$ are the expansion coefficients and E_n the degenerate energies. Insertion of this expansion into the scalar product of Eq. (3.5) results in

$$P(t) = \sum_{n,j} c^{\star}_{n,j} c_{n,j} e^{-i\vec{\sigma_3}(t-t_M)E_n} \tag{3.6}$$

and applying upon it a Fourier transformation gives the unknown energy eigenstates of the implemented arbitrary test wavefunction. The heights of the energy peaks are defined by the absolute value of the energy eigenfunctions of the implemented wavefunction, for more details see [54]. The so generated energy spectrum contains the energies of the related soft-core potential $U(x, z)$ for a fixed ionic charge Z and a soft-core parameter a. Adjusting the energy of the two-dimensional soft-core potential to the three-dimensional Coulomb potential (Eq. (3.1)) by modifying the parameters Z, a the associated wavefunction or a nonlinear combination of the degenerated states with the desired energy can be generated. The wavefunctions associated to the separated energy peaks are then generated in a second loop by again propagating the wavefunction temporally and spatially with the before defined energy value. Notice that the parameters Z, a can only be adjusted to one energy peak, all other peaks are shifted accordingly. For our purpose the energy of the ground state wavefunction was chosen to be equal with the three-dimensional Coulomb energy.

For practical purposes of the calculation of the autocorrelation function $P(t)$ the time

interval $[t_0, t_1]$ is multiplied by a smoothing function before applying the Fourier transformation. In our case a Hann function

$$H(t) = \begin{cases} 1 - \cos\left(\frac{2\pi(t-t_l)}{t_r - t_l}\right) & , \quad t \in [t_l, t_r] \\ 0 & , \quad \text{else} \end{cases}$$

is used, whereas $t_r = t_1 - t_0$ and $t_l = -(t_1 - t_0)$. The advantage is that most of the possible oscillations, resulting from a Fourier transformation of a otherwise rectangle function, in the spectrum is filtered out.

Other possible oscillations can arise from a too small chosen grid size used for the generation of the spectrum, which can be easily suppressed by taking a larger grid. Another crucial factor for the generation of the energy spectrum is the propagation time t. In principle, the propagation time should be infinite in order to get the most accurate position of the energy eigenstates. During our calculation a propagation time of 50 a.u. turned out to be a proper agreement between computation time and accurate position of the energy peaks. In Fig. 3.2 such a typical energy spectrum for the spin-up component of the Dirac spinor is depicted.

The energies of the bound states calculated by the two-dimensional Dirac equation for a pure Coulomb potential depend on the radial quantum number n_r and the absolute value of the σ_3-component of the total angular momentum denoted by the quantum number $|\lambda|$. That means the states with the same n_r, $|\lambda|$ are energetically degenerated. This condition changes in the case of the soft-core potential. The reason is that the symmetry of the Runge-Lenz vector $\mathbf{R}$ is broken

$$\mathbf{R} = \mathbf{p} \times \mathbf{L} - Z\frac{\mathbf{r}}{r} \, . \tag{3.7}$$

The Runge-Lenz vector is a constant of motion in the case of a pure Coulomb potential $V(r) = -Z/r$. The break of symmetry of this vector due to the soft-core potential leads to a non-degeneracy of the energy eigenstates with the same radial quantum number n_r and absolute value of the σ_3-component of the total angular momentum quantum number $|\lambda|$. The comparison of the energy spectrum of the spin-up and spin-down component of the wavefunction shows that the change of the sign of λ and the spin component lead to the same energy values. Before coming to the selection rules in our two-dimensional system

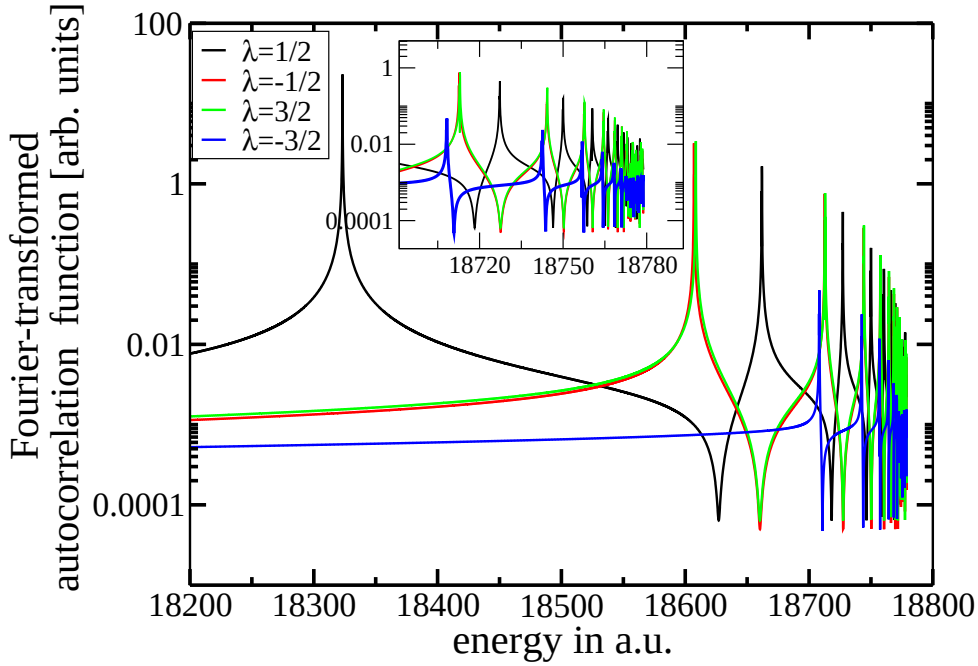

Figure 3.2: Fourier-transformed spectrum of the autocorrelation function $P(t) = \langle\Psi(t)|\Psi(0)\rangle$ for the spin-up component for the different angul ar momentum quantum numbers $\lambda = \pm 1/2, \pm 3/2$. The peaks in this spectrum represent the eigenenergy values in the soft-core potential. The chosen parameters are $Z = 30$ and $a = 0.006$.

the σ_3-component of the total angular momentum and another good quantum number, namely, the parity, will be discussed below.

3.2.4 σ_3 component of the total angular momentum

The eigenvectors of the total angular momentum operator around the σ_3-axis (conventional Pauli spin matrix), for the spin-up and spin-down comprise (in Clifford algebra notation [2]):

$$\Psi_\lambda^\uparrow = e^{-i_3\varphi/2}\,(u_0(r) + u_2(r)\vec{\sigma_2})\,e^{i_3\lambda\varphi} \tag{3.8}$$

$$\Psi_\lambda^\downarrow = e^{-i_3\varphi/2}\,(v_0(r) + v_2(r)\vec{\sigma_2})\,i_2 e^{i_3\lambda\varphi}\,, \tag{3.9}$$

[2] see also appendix (B)

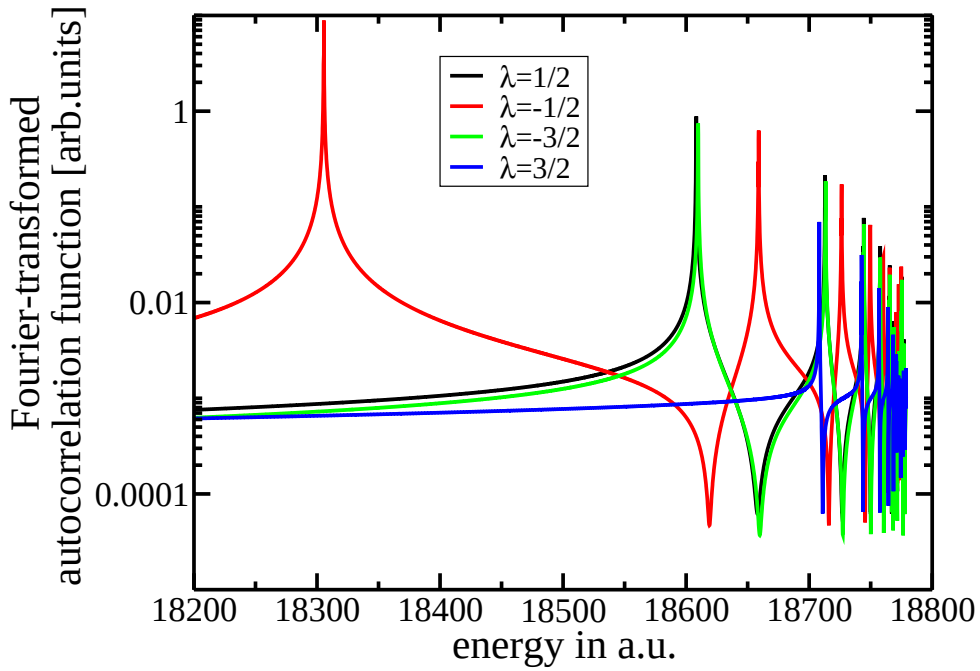

Figure 3.3: Same as figure 3.2, but for the spin-down component of the wavefunction. The position of the energy states are interchanged equivalently to the change of the sign of λ.

or in the standard notation :

$$\Psi_\lambda^\uparrow = \begin{pmatrix} u_0(r)e^{i(\lambda-\frac{1}{2})\varphi} \\ 0 \\ 0 \\ u_2(r)ie^{i(\lambda+\frac{1}{2})\varphi} \end{pmatrix} \qquad \Psi_\lambda^\downarrow = \begin{pmatrix} 0 \\ -v_0(r)e^{-i(\lambda+\frac{1}{2})\varphi} \\ v_2(r)ie^{i(\lambda-\frac{1}{2})\varphi} \\ 0 \end{pmatrix} .$$

Here, $u_0(r)$ and $u_2(r)$ are the solutions of the radial part of the Dirac equation similar to the known textbook example of the hydrogen atom. In our case the system of equations reads:

$$c\frac{\partial u_0}{\partial r} - \frac{c\lambda}{r}u_0 + (E + \frac{Z}{r} + c^2)u_2 = 0 \tag{3.10}$$

$$c\frac{\partial u_2}{\partial r} + \frac{c\lambda}{r}u_2 - (E + \frac{Z}{r} - c^2)u_0 = 0\,. \tag{3.11}$$

The same is true for the spin-down solutions $v_0(r)$, $v_2(r)$. The azimuthal angle φ together with the radius r defines the coordinate system of our two-dimensional problem. After the generation of the wavefunctions, we characterize those by determining their angular momentum and the parity. For the Coulomb potential in three dimensions the σ_3-component

is a good quantum number. In two dimensions the σ_3-component (out of the plane of the coordinate system) is still a good quantum number. To verify, whether we get the same eigenvalue λ of the analytical solvable two-dimensional Coulomb potential [48] in case of the soft-core parameter, the σ_3 component of the total angular momentum is calculated using the known two-dimensional eigenvectors with the two spin orientations up and down

$$\Psi_\lambda^\uparrow = \begin{pmatrix} u_0(r)e^{i(\lambda-\frac{1}{2})\varphi} \\ 0 \\ 0 \\ u_2(r)ie^{i(\lambda+\frac{1}{2})\varphi} \end{pmatrix} \qquad \Psi_\lambda^\downarrow = \begin{pmatrix} 0 \\ -v_0(r)e^{-i(\lambda+\frac{1}{2})\varphi} \\ v_2(r)ie^{i(\lambda-\frac{1}{2})\varphi} \\ 0 \end{pmatrix} .$$

The application of the angular momentum operator $\hat{J}_3$ in σ_3-direction can be written in the standard notation as

$$\left(-i\frac{\partial}{\partial\varphi} + \frac{1}{2}\begin{pmatrix} \sigma_3 & 0 \\ 0 & \sigma_3 \end{pmatrix}\right)\Psi_\lambda^{\uparrow\downarrow} = \lambda\Psi_\lambda^{\uparrow\downarrow} . \tag{3.12}$$

In analogy to the expectation value of the angular momentum operator $\hat{J}_3$, we can reapply $\hat{J}_3$ to calculate the expectation value of $\hat{J}_3^2$

$$-\left(\frac{\partial^2}{\partial\varphi^2} + i_3\frac{\partial}{\partial\varphi} - \frac{1}{4}\right)\Psi_\lambda^{\uparrow\downarrow} = \lambda^2\Psi_\lambda^{\uparrow\downarrow} \tag{3.13}$$

The quantum number λ can be calculated from the norm of

$$\|(\hat{J}_3 - \lambda)\Psi_\lambda^{\uparrow\downarrow}\| = 0 \qquad \lambda \in \mathbb{Z}_{\frac{1}{2}} \tag{3.14}$$

for both the spin-up and spin-down component of the wavefunction. Moreover, Eq. (3.14) also provides a test of the expectation value of the angular momentum operator $\hat{J}_3$ by setting $\lambda = 0$. We show that the eigenvalues of $\hat{J}_3$ and the expectation of Eq. (3.14) of our numerically applied soft-core potential agree with the known values of the Coulomb case. This result will be later used to define the selection rules in the case of the soft-core potential in two dimensions.

3.2.5 Parity

The parity operator $\hat{P}$ is a further quantity, which can be used for the identification of the bound states. The calculation of the parity of the wavefunction will be done using

the Clifford algebra. In this algebra the parity operator $\hat{P}$ is given by:

$$\hat{P}\Psi_{\lambda}^{\uparrow\downarrow}(\mathbf{r},t) \;=\; \gamma_0\Psi_{\lambda}^{\uparrow\downarrow}(-\mathbf{r},t)\gamma_0\;, \tag{3.15}$$

whereas the substitution from $\mathbf{r}\to-\mathbf{x}$ in polar coordinates is written as $\varphi\to\varphi+\pi$. The application of the parity operator on the particular wavefunction ($\Psi^{\uparrow}$,$\Psi^{\downarrow}$) results in the following parities of the wavefunctions:

$$\begin{aligned}
\hat{P}\Psi_{\lambda}^{\uparrow} &= \gamma_0 e^{-i_3\frac{\varphi+\pi}{2}}(u_0(r)+u_2(r)\vec{\sigma_2})e^{i_3\lambda(\varphi+\pi)}\gamma_0\\
&= \gamma_0^2 e^{-i_3\frac{\varphi}{2}}(-i_3)(u_0(r)-u_2(r)\vec{\sigma_2})e^{i_3\lambda\varphi}e^{i_3\lambda\pi}\\
&= e^{-i_3\frac{\varphi}{2}}(u_0(r)+u_2(r)\vec{\sigma_2})e^{i_3\lambda\varphi}e^{i_3(\lambda-\frac{1}{2})\pi}\\
&= (-1)^{\lambda-\frac{1}{2}}\Psi_{\lambda}^{\uparrow} \qquad (3.16)\\
\hat{P}\Psi_{\lambda}^{\downarrow} &= \gamma_0 e^{-i_3\frac{\varphi+\pi}{2}}(v_0(r)+v_2(r)\vec{\sigma_2})i_2e^{i_3\lambda(\varphi+\pi)}\gamma_0\\
&= \gamma_0^2 e^{-i_3\frac{\varphi}{2}}(-i_3)(v_0(r)-v_2(r)\vec{\sigma_2})i_2e^{i_3\lambda\varphi}e^{i_3\lambda\pi}\\
&= e^{-i_3\frac{\varphi}{2}}(v_0(r)+v_2(r)\vec{\sigma_2})i_2e^{i_3\lambda\varphi}e^{i_3(\lambda+\frac{1}{2})\pi}\\
&= (-1)^{\lambda+\frac{1}{2}}\Psi_{\lambda}^{\downarrow}\;. \qquad (3.17)
\end{aligned}$$

The following relations of the Clifford algebra were used, applying the parity operator on the spinor wavefunction [3]:

$$\begin{aligned}
i_k &= i\vec{\sigma_k}\\
[\vec{\sigma_k},\vec{\sigma_l}]_+ &= 0\\
\vec{\sigma_k}^{\,2} &= 1\;.
\end{aligned}$$

The states $\Psi_{\lambda}^{\uparrow}$, $\Psi_{-\lambda}^{\uparrow}$ are non-degenerate in terms of energy and have different parities, which can be seen by the following rules:

$$\hat{P}\Psi_{-\lambda}^{\uparrow} = (-1)^{-\lambda-\frac{1}{2}}\Psi_{-\lambda}^{\uparrow} \tag{3.18}$$

and for the spin-down component of the wavefunction

$$\hat{P}\Psi_{-\lambda}^{\downarrow} = (-1)^{-\lambda+\frac{1}{2}}\Psi_{-\lambda}^{\downarrow}\;. \tag{3.19}$$

[3] A brief excursion into the Clifford algebra is given in the appendix B.

A linear combination of $\Psi^{\uparrow}_{\lambda}$ and $\Psi^{\uparrow}_{-\lambda}$ does not have a well defined parity, as it is the case for the Coulomb potential in three dimensions, and moreover is not energetically viable anymore. The only degenerated states are the pairs with ($\lambda = -1/2 \leftrightarrow \lambda = 3/2$) and ($\lambda = -3/2 \leftrightarrow \lambda = 5/2$) for the spin-up component of the wavefunction as seen from Fig. (3.2). The same is true for the spin-down component of the wavefunction by simply multiplying λ by -1. One more difference to the three-dimensional density distribution is the absence of any bulb-like structure for the p-like states in two dimensions. In the Schrödinger case a nonlinear combination of $\Psi_{m_l}+\Psi_{m_{-l}}$ is conserved. The reason for that, is the dependence of the change of the parity on the angular momentum l rather then on the magnetic quantum number m_l. Therefore, any nonlinear combination of the m_l does not change the parity in the Schrödinger case. In order to guarantee a conservation of the parity in the two-dimensional Dirac case only the following combinations of states $\Psi^{\uparrow}_{\lambda}$ with $\Psi^{\downarrow}_{-\lambda}$ or $\Psi^{\uparrow}_{-\lambda}$ with $\Psi^{\downarrow}_{\lambda}$ are possible. This results in a trivial φ-independent constant for the density distribution. All possible combinations show no specific bulb-like structure for the density of p-like states or states with a higher angular momentum as known from the Schrödinger case.

3.2.6 Selection rules

As shown in the previous section, our two-dimensional soft-core potential has two good quantum numbers, namely the σ_3-component of the total angular momentum and the parity. Together with the radial quantum number n_r, we can now characterize the two-dimensional states and define their selection rules. As can be seen in table 3.2, there are two main differences compared to the known notation in the Dirac case for the Coulomb potential. One is the degeneracy of the "p-states" (for all $P_{1/2}$, $P_{3/2}$, ...) with different quantum number λ. And the other is the difference in energy of the generated states, which originates from the reduced dimension of the system. The reason for the first one is the used soft-core potential, discussed in detail in section 3.2.3. The radial quantum number can be read off from the probability density distribution of the wavefunction. Pictures of these distributions are given in Fig. 3.4 and an exemplary notation of the two-dimensional states is presented in table 3.2. The energy states of the selected ionic

n_r	n=n_r+1	λ	parity	notation	energy in [a.u.]
0	1	1/2	1	$\|1S_{1/2}\rangle$	18323
1	2	-1/2	-1	$\|2P_{1/2}\rangle$	18607
1	2	3/2	1	$\|2P_{3/2}\rangle$	18607
1	2	1/2	1	$\|2S_{1/2}\rangle$	18662
2	3	5/2	1	$\|3S_{5/2}\rangle$	18705
2	3	-1/2	-1	$\|3P_{1/2}\rangle$	18713
2	3	3/2	1	$\|3P_{3/2}\rangle$	18713
2	3	1/2	1	$\|3S_{1/2}\rangle$	18727

Table 3.2: Notation of the relativistic quantum numbers in hydrogen-like Zn^{29+} in two dimensions for the spin-up component. The radial quantum number is denoted by n_r and the total angular momentum by λ.

core charge Z can be identified from the possible ring structures of the probability density distribution of Fig. 3.4. In (a) there is no additional ring structure (ground state), resulting in a radial quantum number of $n_r = 0$. Looking at the probability density distribution in (b), (c) and (d) additional rings appear and the distribution is expanding with an increasing number of rings, representing higher excited states.

3.3 The 2D Dirac atom in a laser field

After having generated the wavefunctions of the bound states of our system of interest we can now look at the dynamics of them by applying an external laser field. In the following section the used laser field will be defined and the split-operator method for the numerical solution of the Dirac equation will be presented.

3.3.1 The laser pulse

We describe the laser field as a plane wave modulated by an envelope function $f(\eta)$. The electric field component reads

$$\mathbf{E}(\eta) = E_0 f(\eta)\cos(\eta)\mathbf{e}_x \,, \tag{3.20}$$

where $\eta = \omega t - \mathbf{kr}$ with the laser frequency ω and the magnetic field is given by:

$$\mathbf{B}(\eta) = E_0 f(\eta)\cos(\eta)\mathbf{e}_y \,. \tag{3.21}$$

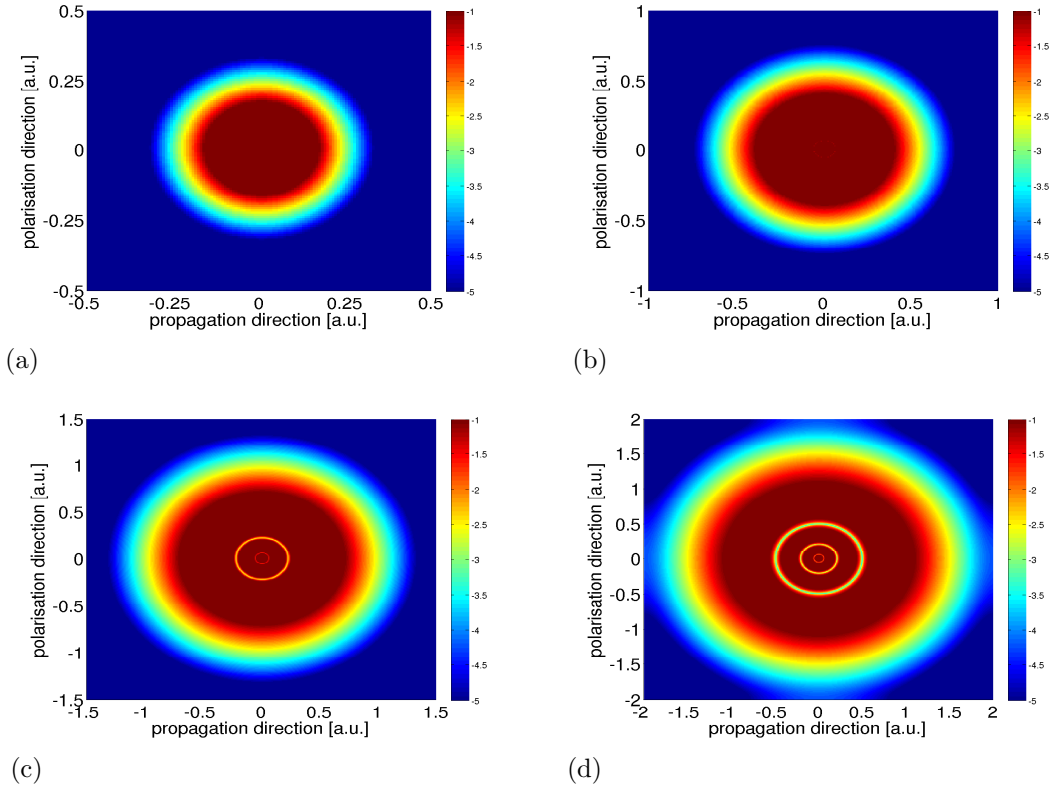

Figure 3.4: Plotted is the probability density distribution for an ionic core charge of $Z = 30$ on a logarithmic color scale of the states (a) $|1S_{1/2}\rangle$, $(n_r = 0)$, (b) $|2S_{1/2}\rangle$ $(n_r = 1)$, (c) $|3S_{1/2}\rangle$ $(n_r = 2)$, (d) $|4S_{1/2}\rangle$ $(n_r = 3)$. Note that the grid size is increasing with higher values of n_r.

The spatial dependency of the vector potential $\mathbf{A}(\eta)$ is responsible for the laser magnetic field effects on the electron wavepacket. The elimination of this spatial dependency allows us to carry out calculations in the dipole approximation and to compare them to the case when the full spatial dependency of the vector potential is taken into account (see chapter 5). The corresponding relation between the vector potential $\mathbf{A}(\eta)$, the electric field $\mathbf{E}(\eta)$ and the magnetic field $\mathbf{B}(\eta)$ is given by: $\mathbf{B}(\eta) = \boldsymbol{\nabla} \times \mathbf{A}(\eta)$, $\mathbf{E}(\eta) = -\frac{1}{c}\frac{\partial \mathbf{A}(\eta)}{\partial t} - \boldsymbol{\nabla} U$, with U to be the stationary potential. The envelope function of the nonlinear polarized light is chosen to be $\sin^2$- shaped. In detail, the ascent and decline are $\sin^2$-shaped with a constant part in between:

$$f(\eta) = \begin{cases} 0 & , \quad -\infty \leq \eta \leq 0 \\ \sin^2(\frac{\eta}{4N_{on}}) & , \quad 0 \leq \eta \leq 2\pi N_{on} \\ 1 & , \quad 2\pi N_{on} \leq \eta \leq 2\pi(N_{on} + N_{const}) \\ \cos^2\left(\frac{\eta - 2\pi(N_{on}+N_{const})}{4N_{off}}\right) & , \quad 2\pi(N_{on} + N_{const}) \leq \eta \leq 2\pi(N_{on} + N_{const} + N_{off}) \\ 0 & , \quad 2\pi(N_{on} + N_{const} + N_{off}) \leq \eta \leq \infty \end{cases}$$

The chosen notation of N_{on}, N_{const}, N_{off} stands for the turn-on phase, the constant phase and the turn-off phase, respectively. This additional envelope function renders the pulse more realistic and compensates the unphysical effects resulting from a sharp turn-on/-off of the pulse.

Experimentally, the spectrum of a mode-coupled laser pulse consists of many lines; resembling a comb. The distance between two neighboring lines is constant and equivalent to the pulse repetition frequency of the laser. This so-called frequency comb has two degrees of freedom, the offset frequency of the comb and the pulse repetition rate. A change of the position of the offset frequency leads in the time domain to a variation of the phase $\Delta\varphi$ of the oscillating electric field from pulse to pulse. If one can control both the repetition rate and the phase of the laser pulse then the exact position of the comb lines are known and one has a guide in the frequency domain to precisely measure the optical frequencies [57].

3.3.2 The Split-Operator technique

The split-operator method was firstly introduced by [54] to solve the time-independent Schrödinger equation for the eigenenergies and eigenstates of a general potential. This

method is used both, for the generation of eigenenergies and eigenstates of the time-independent Dirac Hamiltonian and for the calculation of the time-dependent dynamics of the Dirac wavefunction. Having the bound states of our system, we can start with the calculation of the dynamics of our initially prepared wave packet of the bound state. The dynamics of the system is given by the time evolution of our initial wave packet. The time propagation of the wavefunction is numerically realized by the relativistic split-operator method. Therefore we split the Dirac equation in a derivative-dependent part and a position-dependent part

$$
\begin{aligned}
i\frac{\partial}{\partial t}\Psi(\mathbf{r},t) &= \left[c\alpha^i\frac{\partial}{\partial x^i} + \beta c^2 + \big(A_0(\mathbf{r}) + \alpha^i A_i(\mathbf{r},t)\big)\right]\Psi(\mathbf{r},t) && (3.22)\\
&= \quad \mathbb{H}_{\vec{\partial}} \quad + \quad \mathbb{H}_{\mathbf{r}}\ , && (3.23)
\end{aligned}
$$

whereas $A_0(\mathbf{r})$ is the stationary potential $\varphi(r)$ and $A_i(\mathbf{r})$ are the components of the vector potential $\mathbf{A}(\mathbf{r})$. For a short time interval, where the potential can be taken as a constant, the time evolution of the wave packet can be written as:

$$
\Psi_{t_0+\Delta t} = e^{-i\Delta t\mathbb{H}}\Psi_{t_0}\ , \tag{3.24}
$$

where, $\mathbb{H}_{\vec{\partial}}$ is the derivative part of the entire Hamiltonian $\mathbb{H}$=$\mathbb{H}_{\vec{\partial}}$+$\mathbb{H}_{\mathbf{r}}$ and $\mathbb{H}_{\mathbf{r}}$ the position-dependent part, respectively. That means the time integration of $\mathbb{H}$ in the exponent is substituted by $\Delta t\mathbb{H}$. The time propagation with the Split-Operator method reads then as

$$
\begin{aligned}
\psi_{(t_0+\Delta t)}(\mathbf{r}) \;\approx\; & \exp\left(-i\frac{\Delta t}{2}\,\mathbb{H}_{\vec{\partial}}\right)\exp\left(-i\Delta t\,\mathbb{H}_{(t_0+\frac{\Delta t}{2},\mathbf{r})}\right)\\
& \exp\left(-i\frac{\Delta t}{2}\,\mathbb{H}_{\vec{\partial}}\right)\psi_{t_0}(\mathbf{r}) + O(\Delta t^3)\ . \qquad (3.25)
\end{aligned}
$$

Now the Eq. (3.25) can be iterated as follows $\Psi_t = \Psi_{t_0+N\Delta t}$, where N counts the number of time steps, rendering the wavefunction computable at any time. The error made by this time propagation algorithm is of the order of Δt^3. The derivative part of the time propagator will be handled via a Fast Fourier transformation (FFT) between the momentum and position space. In the case of the Schrödinger equation, upon which one uses the same technique, the exponentials contain in momentum space a scalar operator

in contrast to the Dirac equation, where they contain matrices. This problem can be solved by finding a unitary matrix S that diagonalizes them.

There are several numerical difficulties, which have to be considered and will be briefly mentioned in the following. First of all, the spatial resolution of the wavefunction. It has to be chosen in such a way that the related momentum is not going to be large enough to hit the boundary in momentum space. A simple estimation can be obtained by the analytical results for a free electron [58].
In momentum space:

$$p_{pol} = \frac{E_0}{\omega} \qquad\qquad p_{prop} = \frac{p_{pol}^2}{2c} \ . \tag{3.26}$$

In position space:

$$\Delta x_{pol} = \frac{2E_0}{\omega^2} = \frac{2p_{pol}}{\omega} \qquad\qquad \Delta x_{prop} = \frac{\pi E_0^2}{2c\omega^3} = \frac{\pi p_{pol}^2}{2c\omega} \ , \tag{3.27}$$

whereby Δ denotes the change per laser cycle. These relations can be used to mark an upper limit for the case of bound states. There exist some numerical tricks, which avoid the reflection of the electron distribution on the grid boundary. These methods [48] are based on dynamically adjusting the boundary position by a in both, position and momentum space growing and moving numerical grid, to avoid that the boundary is approached by the wave packet at all [48]. In addition to the spatial resolution one needs to take care of the temporal resolution. In the Dirac case, this is mainly restricted by the large rest mass of the electron, which has to be taken into account. Hence, the temporal resolution is defined by $\Delta t \leq 1/E$ where E denotes the total energy including the rest mass c^2 of the electron, which makes it more demanding in terms of computing time compared to the calculation with the Schrödinger equation. A further point for the numerical calculation is to avoid the destructive reflection of the wave packet at the border of the grid. This is done by applying a function at the edge of the grid, which absorbs the part of the wave function that hits the border of the grid. Another ansatz is to propagate the analytically given free Volkov solution [59] at a certain distance from the ion potential, instead of using the wavefunction at the edges of the grid. With this, the approximation neglects

the atomic potential, but the laser field potential is fully included. This is an appropriate ansatz, for ionization problems with huge intensities, where the electron is driven far away from the nucleus.

3.4 Observables

The quantum mechanical wavefunction contains all the information of the system. The manipulation of it can be used to extract necessary information. During the propagation of the wavefunction by the split-operator method, the observable quantities, which describe the electron dynamics of the applied potential, can be calculated. To illustrate the dynamics of the wave packet, the probability density $\rho(x,z,t) = |\Psi(x,z,t)|^2$ is computed for every time step of the wavefunction $\Psi(x,z,t)$. This allows us to visualize particularly the ionization dynamics of the electron. Moreover, the absorbing boundary conditions of the grid can be used to define a measure of the ionization. Those parts of the wavefunction that hit the border of the grid are absorbed due to the boundary condition. In this sense, the absorption of the wave packet can be used to qualitatively measure the ionization fraction $\Gamma(t)$ by $\Gamma(t) = 1 - e^{-\gamma t}$, where γ is the ionization rate.

Furthermore the center-of-mass motion of the electronic wavefunction is an important observable and comparable with the motion of a classical particle. The expection values of the polarization (x-direction):

$$\langle x \rangle = \int_{z_{min}}^{z_{max}} dz \int_{x_{min}}^{x_{max}} dx |\Psi(x,z,t)|^2 x \tag{3.28}$$

and the propagation (z-direction):

$$\langle z \rangle = \int_{x_{min}}^{x_{max}} dx \int_{z_{min}}^{z_{max}} dz |\Psi(x,z,t)|^2 z \tag{3.29}$$

direction are additionally calculated during the propagation of the wavefunction to visualize the center-of-mass motion of the electron. A matter of interest is also the radiation spectrum of a moving particle (electron) characterized by the radiated energy d^2W at a frequency interval $d\omega$ in the solid angle $d\Omega$. In general, it can be calculated by the classical non-relativistic formula [60]

$$\frac{d^2W}{d\omega d\Omega} = \frac{1}{2\pi c^3} |a_\perp(\omega)|^2 \,, \tag{3.30}$$

where $a_\perp$ is the acceleration component perpendicular to the observation direction. In the quantum mechanical calculation of the radiation spectrum the above formula (3.30) is modified by replacing the classical acceleration component by the expectation value of the acceleration. In the relativistic case this simple modification can not be applied as there exist principle difficulties to define an appropriate velocity in the Dirac theory, see discussion in [61]. Another ansatz is the calculation of the emission spectrum from the charge current, which is done here. For more details on this calculation the reader is referred to the extensive discussion in the work of G. Mocken [48].

The main interest lies in the next two observables. The first one is probability of the electron to be in a certain stationary state $|\langle\phi_i|\Phi(t)\rangle|^2$, where $\Phi(t)$ denotes the actual wavefunction. This observable is used to characterize the population dynamics of the bound states. In use of that definition the amount of population in the continuum state can be additionally evaluated. The ionization probability is given by:

$$P(t) = 1 - \sum_{i=1}^{N} |\langle\phi_i|\Phi(t)\rangle|^2 \,, \tag{3.31}$$

where N stands for the number of bound states. From this the ionization fraction can be determined as the ionization probability at the end of the pulse, which is qualitatively used to compare with experimental results. It is rather more efficient to calculate the total occupancy of the bound state population and substract it from one, as to calculate the overlap of the actual wavefunction with the continuum states, which are much larger in number.

Another observable of interest is the calculation of the transition dipole moments of particular interest for the bound dynamics. The one-photon transition dipole matrix element can be calculated in x-direction by the following expression:

$$d = \langle\Psi_1|x|\Psi_2\rangle \,, \tag{3.32}$$

where x denotes the dipole moment direction and Ψ_1 and Ψ_2 are the bound state wavefunctions of the associated transitions given for some specific transitions in table 3.3. Higher multipole moments can not be directly calculated like carried out in Eq. (3.32). The

Table 3.3: Table of some specific transition dipole moment matrix elements for a one-photon transition in Zn^{29+}. Here $\Delta\omega$ gives the transition frequency to the ground state $|1S_{1/2}\rangle$.

transition	dipole moment	$\Delta\ \omega$ in [a.u.]
E1 ($\|1S_{1/2}\rangle \leftrightarrow \|2P_{1/2}\rangle$)	2.47×10^{-2}	285
M1 ($\|1S_{1/2}\rangle \leftrightarrow \|2S_{1/2}\rangle$)	1.33×10^{-10}	339
E1 ($\|2S_{1/2}\rangle \leftrightarrow \|2P_{1/2}\rangle$)	5.99×10^{-2}	54
M1 ($\|2S_{1/2}\rangle \leftrightarrow \|3S_{1/2}\rangle$)	9.22×10^{-10}	65

non-trivial calculation of multiphoton transition matrix elements is shown in chapter 5 using Rabi oscillations.

3.5 Classical relativistic model

An alternative approach to describe the interaction of atoms with strong laser fields is the solution of the classical relativistic motion of an electron in the combined field of an ultra-strong laser and the Coulomb potential of a hydrogen-like multiply charged ion. This nonlinear interaction is represented by the system of eqs. (3.33), where only the energy of the initial state is quantum mechanically given. As no single classical state of the atom is spherical symmetric. Our classical calculation is mostly applied in the regime of low laser frequencies and strong fields, where it is well-known that quantum mechanical and classical simulations are in good agreement. This has been additionally verified by our Dirac calculation on the observable of interest, the *ionization fraction*. Moreover, we verified that in the limit of large number of trajectories both calculations of the ionization fraction agree considerably, apart from pure quantum effects like the spin which are not included in the classical calculation.

3.5.1 Monte-Carlo simulation

In a real atom the electron is quantum mechanically described by a wavefunction, while in phase space an ensemble of classical particles is used by averaging over various initial electronic positions $\mathbf{r}$ in space and momentum $\mathbf{p}$. In the pioneering work of Percival

and Leopold [62] the stationary ground state of the hydrogen atom was modeled by a microcanonical ensemble in phase space. The full three-dimensional extension of this problem for the relativistic equations of motion with focus on the investigation of the ionization time in the case of the hydrogen atom can be found in [63]. Here, the calculation of the ionization fraction with the relativistic ground state energy E_g is carried out by following this procedure in the case of arbitrary ionic charges Z. In the phase space model the equation of motion is solved separately for each member of the ensemble with randomly chosen initial conditions under the constraint of a fixed atomic ground state energy. The stationary ground state is modeled by a microcanonical distribution in order to simulate the statistical property of the electron wavefunction. This distribution function is given in phase space by

$$\rho(\mathbf{r},\mathbf{p}) \propto \delta(E - E(\mathbf{r},\mathbf{p}))$$

with the relativistic energy $E(\mathbf{r},\mathbf{p}) = c^2\sqrt{1+|p|^2/c^2} - V(r)$ with an electrostatic potential V(r). A member of the microcanonical ensemble is generated by a set of uniformly distributed parameters $\{|\mathbf{l}|^2,\ t\}$ via [63], where $\mathbf{l}$ is the angular momentum and t the time from which the position $\mathbf{r}$ and momentum $\mathbf{p}$ as initial conditions can be generated and are implemented in Eq. (3.33). The classical relativistic equations of motions in the 6-dimensional phase space are given by:

$$\dot{\mathbf{r}} = \frac{1}{\gamma}\mathbf{p}, \qquad \dot{\mathbf{p}} = -\left(\mathbf{E}(\mathbf{r},t) + \frac{1}{c\gamma}\mathbf{p}\times\mathbf{B}(\mathbf{r},t)\right), \tag{3.33}$$

where $\mathbf{E}(\mathbf{r},t) = -\frac{1}{c}\frac{\partial\mathbf{A}(\mathbf{r},t)}{\partial t} - \boldsymbol{\nabla}\varphi(r)$, $\varphi(r) = Z/r$, $\mathbf{B}(\mathbf{r},t) = \boldsymbol{\nabla}\times\mathbf{A}(\mathbf{r},t)$ and $\mathbf{A}(\mathbf{r},t) = A_0\cos(\omega t - \frac{\omega}{c}z)\mathbf{e}_x$ with time t, laser frequency ω and spatial components x, z in polarization and propagation direction, respectively, with $\gamma = \sqrt{1+|\mathbf{p}|^2/c^2}$. They can be numerically solved by implicit iterative methods of ordinary differential equations. We use here the well-known Runge-Kutta method of 4th rank with adaptive step size regulation [64]. The initial state is given by the fixed energy $E_g = c^2\sqrt{1-(Z\alpha)^2}$ and five additional parameters, which define the location of the electron orbit in space and the position of the electron on it. The polar coordinates R, φ via [63] determine the position of the electron on the orbit (solution of the relativistic equation of motion of an electron in the Coulomb field) and the three Euler angles ψ, φ, θ give the orientation of the

electron orbit in space . From these five classical quantities and the fixed energy E_g the initial conditions of the electron's position and momentum can be determined by a series of vector transformations together with an iterative solution of the Kepler equation. A summary of the general steps of the phase space method solving the relativistic classical equation of motion is given in the following:

- Step 1: Determine the energy E_g of the desired state for which the trajectories will be calculated $E_g = c^2\sqrt{1-(Z\alpha)^2}$.

- Step 2: Prepare the microcanonical ensemble where the angular momentum $\mathbf{l}$ and the time t are uniformly distributed in a certain range of parameters.

  1. $0 < E_g < c^2$
  2. $1 < c^2 l^2 < 1/W$
  3. $0 < t < \frac{2\pi}{c^3 W^{3/2}}$

  with $W = 1 - \frac{E_g}{c^4}$. The angular momentum and the time are randomly chosen within the above mentioned interval.

- Step 3: Numerically solve the relativistic Kepler problem to get the eccentricity u. The radius R and angle φ of the electron orbit can be expressed as a function of u.

- Step 4: Calculate the initial conditions of the position $\mathbf{r}$ and the momentum $\mathbf{p}$ from u, $\mathbf{l}$, t and the energy E_g of the position of the electron on its orbit.

- Step 5: Employ a rotation in space by applying the rotation matrix A consisting of randomly chosen Euler angles:

$$\mathbf{r}' = A\mathbf{r} \qquad \mathbf{p}' = A\mathbf{p}$$

with

$$A = \begin{pmatrix} -\cos\varphi\sin\eta - \sin\varphi\cos\theta\cos\eta & -\cos\varphi\cos\eta + \sin\varphi\cos\theta\sin\eta & -\sin\varphi\sin\theta \\ -\sin\varphi\sin\eta + \cos\varphi\cos\theta\cos\eta & -\sin\varphi\cos\eta - \cos\varphi\cos\theta\sin\eta & \cos\varphi\sin\theta \\ -\sin\theta\cos\eta & \sin\theta\sin\eta & \cos\theta \end{pmatrix},$$

where
$0 \leq \theta \leq \pi$, $0 \leq \varphi \leq 2\pi$ and $0 \leq \eta \leq 2\pi$, to define the orientation of the electron's orbit in space.

In the non-relativistic case the orbits of the stationary electron motion are closed (ellipses) and the motion is periodic. However, in the relativistic case the orbits are no longer closed, as a perihelion shift is present and the distance from the center r is not the same. The reason is that in this case the energy of the electron $\mathcal{E} = c\sqrt{p^2 + m^2c^2}$ is always larger than the Coulomb potential $-Z/r$. Instead of ellipses the orbits are like rosettes. That means the property of a finite motion in the non-relativistic mechanics is lost in the relativistic mechanics. The relativistic Coulomb problem of an electron moving in the Coulomb field can be solved analytically [63] parameterized by radius $R(u)$, angle $\varphi(u)$ similar to the standard solution of the classical Kepler problem [65].
For sufficient strong laser fields the potential barrier is suppressed well below the energy of the bound electron, which can then escape on classical orbits. This regime is known as the over-the-barrier ionization (OTBI) regime. Our classical approach for the calculation of the ionization fraction is particularly justified by the fact that the atomic potential becomes less important with increasing laser intensities. From the known electron position $\mathbf{r}$ and the momentum $\mathbf{p}$ we can classically calculate all other observables by taking the ensemble average. The number of necessary classical particles employed for the average is defined by the condition that any further increase of trajectories does not lead to a visible change of the considered property. However, classical approaches do not apply when intrinsic quantum mechanical effects such as quantum coherence or interference become significant. Moreover, the classical calculations were proven to be useful for understanding the underlying physics, especially in situations where the relativistic laser-matter interaction cannot be treated fully three-dimensional in quantum mechanics. We are especially interested in calculating the ionization fraction in order to determine most sensitively ultra-strong laser intensities using multiply charged hydrogen-like ions (chapter 4).

Chapter 4

Ionization dynamics of multiply charged ions

4.1 Motivation

A profound insight into fundamental ultra-high field laser-matter interactions [66] requires an increase in the maximum intensity [20] and a decrease of the minimum pulse duration [67] of currently available lasers. The next generation of such laser pulses are regarded to reach peak intensities of up to $10^{23} - 10^{26}$ W/cm^2 [13,68]. These ultra-intense laser fields provide an understanding into the fascinating field of strong laser-matter interactions, e.g. to test the validity of QED through vacuum polarization [14], to study nuclear interaction and generating GeV electron beams [15] or for medical applications as accomplished in cancer therapy [16]. A better characterization of the ultra-intense laser fields leads to a better understanding of ultra-intense laser fields and assist to generate even higher intensities in the future. Therefore, relativistic laser-ion interaction has been investigated in this thesis in order to determine ultra-strong laser intensities and to characterize them with respect to the pulse length, shape and phase.

The generation of ultra-intense laser fields can be controlled by two main parameters. It is either possible to reduce the spot size of the laser focus or to increase the laser power. For the reduction of the spot size including the temporally and spatially sensitive distortion of the wavefront and the correction of the aberration of the focusing optics [69], rendering the task very challenging. However, the tight focusing of the laser pulse is more effective

than to increase the laser power, if the aberration can be handled. For laser intensities below $I = 10^{16}\mathrm{W/cm^2}$ (SI units), the peak intensity can be measured simply from the spot size and the given laser power. For higher laser intensities the energy flux is so strong that hardly any detector will sustain these intensities and report the necessary intensity profile with enough resolution spatially as well as temporally. Instead of these direct measurements, which are feasible for relatively low laser intensities, we consider indirect techniques using multiply charged ions to characterize ultra-intense laser fields. This technique provides a measure of the laser field amplitude, as the multiply charged hydrogen-like ion can be chosen such that the mean atomic field strength is comparable to the laser field. The ionization of the hydrogen-like ions [70] depend both on the atomic field strength and the maximal laser intensity. The ease of selectively generating multiply charged hydrogen-like ions of any charge [70] renders them applicable to probe a wide range of laser intensities, both current and future ones, without being limited by a specific preparation of the laser pulse.

Before explaining the method and results in more detail we like to give an idea about the strengths of the atomic electric field in multiply charged hydrogen-like ions and in comparison the field strengths of the applied laser intensities. The unit mean atomic electric field strength is, due to the electrostatic interaction between the proton and an electron on the first Bohr orbit in hydrogen, defined by $E_a = 1$ a.u. ($E_a = 5.14 \times 10^9\mathrm{V/cm}$). The corresponding field intensity is $I_a = 1$ a.u. ($I_a = 3.51 \times 10^{16}\mathrm{W/cm^2}$). This sets an intensity scale for a hydrogen atom in its ground state. The field strength changes dramatically (proportional to Z^3) for higher multiply charged hydrogen-like ions. However, as seen from the Fig. 4.1 the highest field strength, which can be achieved today with intense lasers is already reached for the hydrogen-like ion with an ionic core charge of $Z = 10$. For these high laser intensities we are still in the lower part of the mean atomic field strength ($< 10^{13}\mathrm{V/cm}$) curve plotted in Fig. 4.1. The maximal atomic field strength of this curve is given for hydrogen-like uranium U^{92+} with a field strength of $1.8 \times 10^{16}\mathrm{V/cm}$ (SI units), which corresponds to an intensity of $4.2 \times 10^{29}\mathrm{W/cm^2}$ (SI units). These estimations show that the compensation of the laser field strength by the atomic field strength of multiply charged ions is by far not reached yet. Although a natural

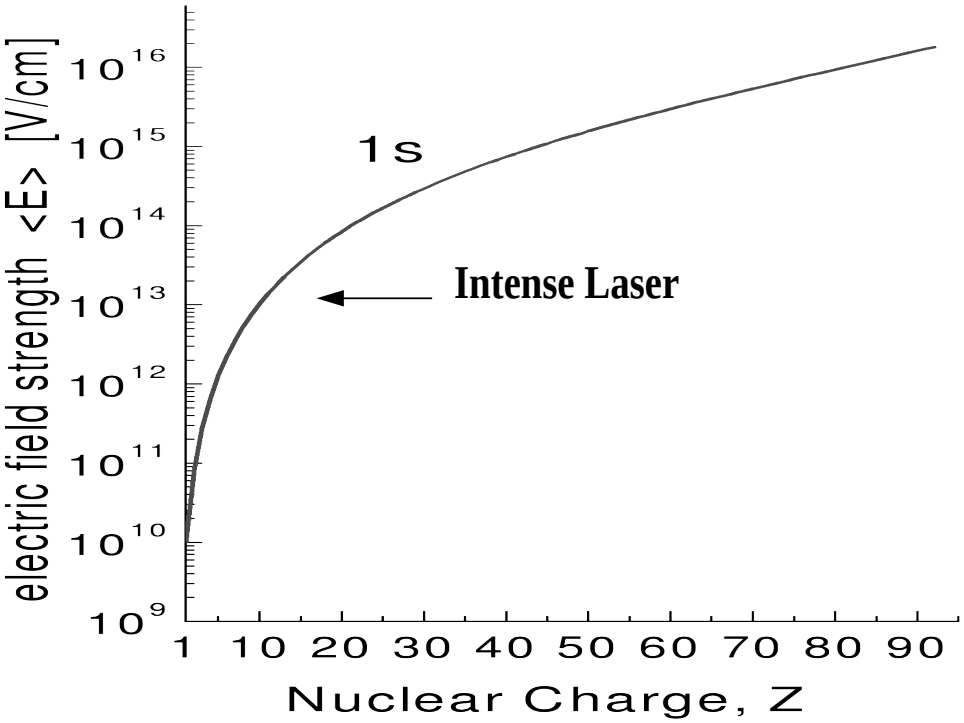

Figure 4.1: Plotted is the mean atomic field strength of hydrogen-like ions as the function of the ionic core charge Z. With the nowadays possible laser intensities we are just on the lower part of this curve as marked by the arrow. There are still 4 orders of magnitude of the atomic field strength remaining for the determination of much higher laser intensities with the use of multiply charged ions, than available today.

limit of the atomic field strength will be the critical charge $Z_{crit} = 137$ of the nucleus, where the bound state wavefunction becomes delocalized, resulting in an instable nuclei.

In the following the photoelectron spectra and the ionization rates are studied both with classical relativistic and quantum Dirac calculations.

4.2 Ionization rate

The ionization process manifests itself for electric field strengths which become comparable to or are higher than the corresponding binding atomic field strength experienced by the electrons. Throughout the thesis we only consider systems with one electron, namely multiply charged hydrogen-like ions. In these systems the electron can escape with substantial probability from its bound state via tunneling or in case that the laser field suppresses the Coulomb barrier strong enough by classically leaving the ionic core. By gaining energy from the laser field the electron accomplishes a wiggling motion in the laser field perturbed by possible Coulomb attraction. The amplitude of this motion in case of strong laser fields exceeds the Bohr radius by several orders of magnitude and the corresponding cycle averaged kinetic energy (ponderomotive potential $U_p = \frac{F^2}{4\omega^2}$) is much greater than the binding energy.

For bound-free transitions the analysis of the Keldysh parameter γ classifies the possible ionization processes. In the non-relativistic case, γ is given by $\gamma = Z\omega/F$, with the ionic core charge Z, the laser frequency ω and the laser field strength F. For multiphoton ionization realized by a high laser frequency and a low laser field strength, $\gamma^2 \gg 1$, the bound-free transition can be fully perturbatively described. Here, ionization occurs by simultaneous absorption of N, N+1, ... photons, where N is the smallest number of photons needed to reach the continuum. Related to this ionization process is the finding of the above-threshold ionization by P. Agostini et al. [71], where they showed that the atom may absorbs many more photons than the minimum number N of photons necessary for the ionization. In the strong field limit $\gamma^2 \ll 1$, realized by low frequency and high field strength, the laser field suppresses the Coulomb barrier so strong that the electron can classically leave the ionic core. The related ionization process can be in the limit

of adiabatic variation of the field described by the quasistatic ionization rate w, whose analytical calculation will be discussed below.

4.2.1 Semiclassical calculation in the non-relativistic regime

In this section and the following, the calculation of the analytical ionization rate formula valid in the tunnel regime will be briefly discussed, which is later used to compare with our numerical relativistic classical trajectory Monte-Carlo (CTMC) simulation. In the strong field ionization regime only the initial and the final state has to be known for the calculation of the ionization rate, i.e. no intermediate state has to be considered, which complicates the whole calculation tremendously. This can be fulfilled by the conditions $\omega \ll I_p$ and $F \ll F_{at} \sim Z^3$ permitting the use of a quasiclassical approximation, where I_p denotes the ionization potential and F_{at} the atomic field strength. Implying, a constant electric and magnetic field during the tunneling process. In the case of strong low-frequency fields, the transition amplitude A_{if} from the initial state i to the final state f is calculated in the adiabatic limit ($\omega \ll I_p$) by the well known general Landau-Dykhne formula:

$$A_{if} = \exp\left\{ i \int_0^{t_0} dt (E_f(t) - E_i(t)) \right\} . \tag{4.1}$$

Here E_i denotes the initial and E_f the final energy, respectively and the complex time t_0 is calculated from the constraint $E_i(t_0) = E_f(t_0)$. In the adiabatic approximation the ionization rate strongly depends on the chromaticity of the radiation field, the ponderomotive acceleration of the ejected electrons and the saturation of the ionization probability. The ionization rate is given in the non-relativistic case in its most general form, valid also for excited states in complex atoms, well known as the ADK (Ammosov-Delone-Krainov) formula [72] in the case of linear polarized light by:

$$\begin{aligned} w_m^l &= (2l+1)\left(\frac{3Fn^{\star 3}}{\pi Z^3}\right)^{1/2} (Z^2/4\pi n^{\star 3})(2e/n^\star)^{2n^\star}(l+|m|)! \\ &\quad \left(\frac{2Z^3}{Fn^{\star 3}}\right)^{2n^\star - |m| - 1} 2^{-|m|}[(|m|)!(l-|m|)!]^{-1} \exp(-2Z^3/3n^{\star 3}F) , \end{aligned} \tag{4.2}$$

where $n^\star = Z/\sqrt{2\mathcal{E}_n}$ is the effective principal quantum number, l the orbital quantum number, m the magnetic quantum number, F the electric field strength and Z the charge

of the ionic core. The effective principal quantum number $n^\star = n - \delta_l$ takes quantum defects δ_l of the ionic core charge into account, caused by the innershell electron screening of the ionic core on the outershell electrons. Its value is determined by experimental data of the binding energy, considering the large distance of the electron from the ionic core.

In case of the orbital quantum number $l = 0$ and the magnetic quantum number $m = 0$ the general form of the tunnel rate Eq. (4.2) reduces for hydrogen-like ions in electromagnetic fields to

$$w_{nr} = \left(\frac{3F^3 n^{\star 3}}{64\pi^3 Z^5}\right)\left(\frac{4eZ^3}{Fn^{\star 4}}\right)^{2n^\star} \exp\left\{-\frac{2Z^3}{3n^\star F}\right\} . \tag{4.3}$$

For $m \neq 0$ and for the same orbital quantum number l, the tunnel rate is substantially lower. Moreover, the ionization rate depends on the initial momentum of the electron. For non-zero initial momentum, Nikishov & Ritus [73] and Delone & Krainiov [74] calculated the ionization rate to be

$$w(p_\parallel) = w(0)\exp\{-p_\parallel^2\omega^2(2E_i)^{3/2}/3F^3\} , \tag{4.4}$$

where $p_\parallel$ denotes the electron momentum in the laser field direction. In the case of zero initial momentum the ionization rate for linear polarized light $F = F_0\cos(\omega t)$ is given by

$$w_{nr} = \frac{4\kappa^5}{F}\exp\left(-\frac{2}{3}\frac{\kappa^3}{F}\right) , \tag{4.5}$$

with $\kappa = \sqrt{2I_p}$ and I_p the ionization potential of the atom. This expression is true as long as $F \ll F_{at}$, whereas F_{at} is the atomic field strength. These formulae (4.4), (4.5) can only give a limited idea of the ionization process. For more detailed information of the tunneling ionization process, it is necessary to look at the energy-resolved and angle-resolved energy spectra of the ejected electrons.

4.2.2 Semiclassical calculation in the relativistic regime

The main difference between the non-relativistic and relativistic calculation of the tunnel rate originates from the difference in their binding energies, which has a significant influence for charges of $Z \geq 10$. The relativistic generalization of the Keldysh parameter

is $\gamma_{rel} = \frac{\omega}{F}\sqrt{1-\epsilon^2}$, with $\epsilon = \sqrt{1-(Z\alpha)^2}$ and $\alpha = 1/c$, where c is the speed of light. A complete derivation of the Keldysh parameter is given e.g. in [75]. In the relativistic case a semiclassical expression for the ionization rate for the Coulomb potential was derived recently by [76]. In SI units they found:

$$\begin{aligned} w_r &= \frac{mc^2}{\hbar}\frac{(F/F_s)^{1-2\epsilon}}{2\sqrt{3}\xi\Gamma(2\epsilon+1)}\sqrt{\frac{3-\xi^2}{3+\xi^2}}\left(\frac{4\xi^2(3-\xi^2)^2}{\sqrt{3}(1+\xi^2)}\right)^{2\epsilon} \\ &\quad \times \exp\left(6\mu \arcsin\frac{\xi}{\sqrt{3}} - \frac{2\sqrt{3}\xi^3}{F/F_s(1+\xi^2)}\right) \end{aligned} \tag{4.6}$$

with

$$\mu = \frac{e^2 Z}{\hbar c} \tag{4.7}$$

$$\epsilon = \sqrt{1-\mu^2} \tag{4.8}$$

$$\xi = \sqrt{1-\frac{\epsilon}{2}(\sqrt{\epsilon^2+8}-\epsilon)} \tag{4.9}$$

$$F_s = \tfrac{m^2c^3}{\hbar e} = 1.32\times 10^{16}\frac{V}{\mathrm{cm}} \tag{4.10}$$

This formula agrees for the ground state in the limit of $Z = 1$ with the non-relativistic formula of Eq. (4.2). Both, for the non-relativistic and the relativistic case, the calculation of the ionization rates are based on the WKB (Wentzel, Kramers, Brillouin) method. Its principal concept is described in the following.

The ground state wave function remains valid in the vicinity of the nucleus. In this region the influence of the laser field is negligible. In far distance from the nucleus the effect of the Coulomb potential is weak and the wavefunction can be determined by a quasiclassical solution. The complete wavefunction is then constructed by matching these two solutions over the whole region of interaction. The WKB approximation (potential is constant within the laser wavelength) is sufficiently good for low-lying states including the ground state. Within the approximation ($\omega \ll I_p$), it is assumed that the electric laser field is temporally constant over the period of tunneling ($a_0 \ll \lambda$). Another aspect of the tunnel ionization process has to be considered, namely the critical field strength $F_{crit}^{non-rel.}$ for the exert of over-the-barrier ionization in the non-relativistic case, as generally given for atoms by $F_{crit}^{non-rel.} = I_p^2/4Z = Z^3/16$ [77]. This is known to be the level at which

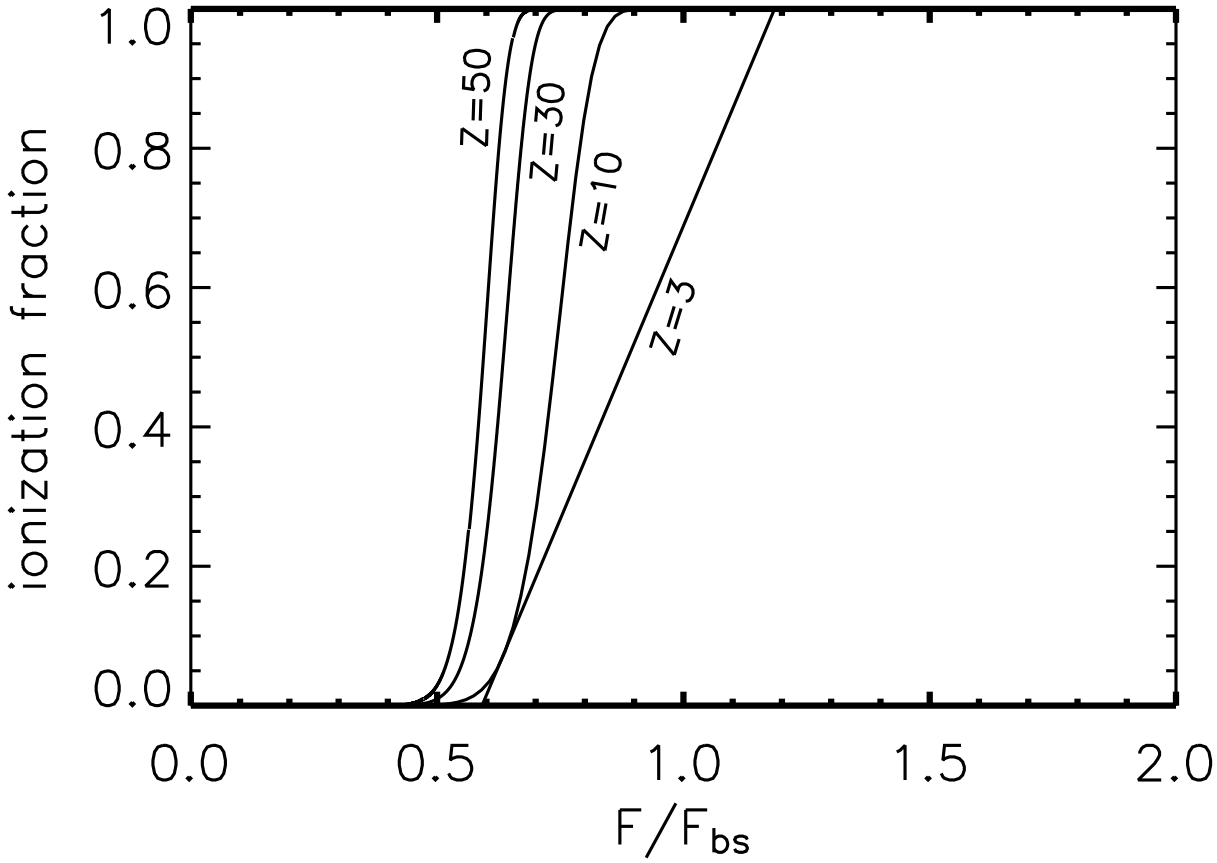

Figure 4.2: Comparison of the relativistic tunnel ionization fraction see Eq. (4.6) of a linear polarized one-cycle pulse of frequency $\omega = 0.043$ a.u. ($\lambda = 1054$ nm) for different charges Z as a function of the field strength normalized by the barrier suppression field strength F_{bs} as defined in the text.

the laser field strength becomes equal to the Coulomb barrier, beyond over-the-barrier ionization takes place. However, for hydrogen-like ions the general non-relativistic field strength changes to $F_{crit,new}^{non-rel.} = (\sqrt{2}-1)Z^3/2^{3/2}$ [78]. That means, the general critical field strength $F_{crit}^{non-rel.}$ underestimates the tunnel rate by roughly a factor of two in the case of hydrogen-like ions. The reason for the discrepancy of the critical field strength is based on the fact that the electron motion in propagation direction and polarization direction can not be considered as independent for hydrogen-like ions.

Subsequently, the relativistic tunnel ionization fraction is investigated for various ionic core charges Z. Instead of the ionization rate, we evaluated the ionization fraction, which is comparable with experimental results. It is defined as the ionization rate measured

at the end of the laser pulse. In Fig. 4.2 the relativistic tunnel rate ionization fraction measured at the end of a one-cycle sinusoidal pulse is displayed. In order to compare the tunnel rate for the different charges Z properly, the applied laser field strength is normalized by the barrier suppression field strength for over-the-barrier ionization F_{bs}. Hereby, F_{bs} is defined as $F_{bs} = c^4/4Z(1-\sqrt{1-Z^2/c^2})^2$, with c to be the speed of light. The relativistic ionization fraction starts for high ionic core charges at smaller values of the normalized field strength compared to low ionic core charges. However, the experimental relevant ionization takes place in the region of $0.3 < F/F_{bs} < 0.7$. A comparison of the relativistic tunnel rate formula of Eq. (4.6) with a relativistic classical trajectory Monte-Carlo simulation will be given in section 4.4.5.

4.3 Determination of ultra-strong laser intensities

In the regime of moderate laser field strength $10^{14}-10^{17}\mathrm{W/cm^2}$ the laser intensities can be simply determined by the focus spot size of the laser beam and the beam energy. Another possibility is to use the change of the intensity dependent refraction index. However, these direct measurement techniques are of no use if ultra-intense laser intensities are involved. Firstly, only a few detectors would actually sustain the ultra-strong laser [20] intensities and secondly, the acquired speed and resolution to report the intensity profile is above the possibilities of the nowadays available detectors. Therefore, it is necessary to look for indirect intensity-dependent effects, which characterizes these high laser intensities and are described after a short review of the laser intensities reached today and scheduled for the future together with possible applications.

The availability of lasers reaching intensities considerably higher than the characteristic atomic field strength of $F_a = 5.1 \times 10^9$ V/cm [79] allows to access a new regime for the study of laser-matter interaction [80]. The next generation of high-power laser sources is going to reach peak intensities of up to 10^{23}-10^{25} W/cm^2 [13]. They offer a wide range of application like in high field physics [81] concerning photon-photon splitting due to virtual electron-positron pair production in vacuum; in attoscience to freeze dynamical processes [82]; and hadron therapy [83].

Nevertheless, in this regime there is no accurate way of experimentally measuring high laser intensities just by the laser power and the spot size of the laser beam. Moreover, the tighter focus of the laser pulse and the associated temporally and spatially sensitive distortion of the wavefront [20] has to be taken into account, rendering the task very challenging. Instead of direct measurements, which are feasible for relatively low laser intensities, we consider indirect techniques using multiply charged ions to characterize ultra-intense laser fields. This technique provides a measure of the laser field amplitude as multiply charged hydrogen-like ion can be chosen such that the atomic field strength is on average comparable to that of the laser field. The ionization of the selected ions [70] depend both on the atomic field strength and the maximal laser intensity, the relation of which will be governed by the chosen atomic species [84]. The ease of selectively generating multiply charged hydrogen-like ions of any charge [70] renders them applicable to probe a wide range of laser intensities, both current and future ones, without being limited by the preparation of the laser pulse.

The central interest will be to develop a procedure with optimal precision which determines the maximal laser field strength of ultra-strong short pulses especially in the intensity range of $10^{18} - 10^{26}\mathrm{W/cm^2}$. We show, based on classical relativistic trajectory Monte-Carlo simulations, how a particular hydrogen-like ion is identified to most sensitively determine the applied laser field strength via measuring the fraction of over-the-barrier ionization (OTBI). Additionally, the ionization angle of the ejected electron is investigated by the full quantum mechanical solution of the Dirac equation of the laser-matter interaction in two dimensions [87]. In this case the laser field strength has been linked to the ionization direction of the ejected electron as an alternative measurement technique. Both methods will be discussed separately in the following sections.

4.3.1 Quantum Dirac calculation - ionization angle

One possibility to determine ultra-strong laser intensities is by means of the angle of the ejected photoelectrons. The numerical analysis of the photoelectron angle in the relativistic regime is done via solving the Dirac equation (3.3) in two dimensions. The

initially prepared Dirac ground state of the atomic wavefunction of the ionic core charge Z is then propagated in time on a two-dimensional grid.

The initial angular distribution of the ejected electron has a maximum in laser polarization direction in case of linear polarized field for low field strengths. The drift component of the electron momentum in propagation direction increases for higher field strength as does the magnetic force. For the laser field strength considered here, the electron acquires a non-negligible drift velocity in the propagation direction, due to the Lorentz force, which is taken into account in our two-dimensional analysis. We make use of the Doppler effect in combination with conventional laser intensities accessible nowadays to show that our method works in the regime of future ultra-strong laser intensities, which can be realized experimentally by counterpropagating an ion beam with a laser beam. This technique enables us to reach higher field strengths and frequencies in the ion's rest frame, which will be used for our numerical calculation. With a gamma boost up to 30, which is possible, e.g. at the GSI [88], the standard laser wavelength of $\lambda = 1054$ nm ($\omega = 0.043$ a.u.) in the laboratory frame can be transformed to $\underline{\lambda} = 17.6$ nm ($\underline{\omega} = 2.58$ a.u.) in the ion's rest frame. The transformation of the laser frequency to higher values in the ion's rest frame additionally ensures that the numerical calculation is feasible in terms of computation time. The necessary transformation of the laser parameters between the ion frame (underlined) and the laboratory frame is expressed by the following formulae:

$$\underline{E_0} = \gamma(1+\beta)E_0 \qquad \underline{\omega} = \gamma(1+\beta)\omega \qquad \beta > 0\ , \tag{4.11}$$

where the scaled velocity β of the ion is given by $\gamma = 1/\sqrt{1-\beta^2}$. The considered values of both the laser frequency and field strength still require a considerable numerical effort, caused by the high momentum of the electron after the ionization. The total energy of the electron E including its large rest mass c^2 thereby needs to be temporally resolved by $\Delta t \leq 1/E$, which renders the numerical calculation very lengthy in terms of computation time. Before discussing the results, we address some numerical issues of the calculations.

The Dirac wavefunction, prepared to be initially in the ground state, is propagated in time on the two-dimensional grid. The electron momentum therefore increases substantially, due to the dominant interaction with the laser field, when the electron leaves the vicinity of

the ionic core. In the recollision scenario, the grid size needs to be increased dramatically in order to deal with the high electron momenta when it returns to the core. As we are only interested in the initial ionization distribution, we restrict ourselves to the vicinity of the ionic core. Numerically, this is accomplished by using absorbing boundary conditions on the grid. Consequently, the norm of the wavefunction decreases continuously when the wavefunction encounters the boundary.

In our two-dimensional calculation, which incorporates all the necessary physics of the ionization dynamics [4], the characterization of the bound states in terms of the total angular momentum quantum number is different from the well-known three-dimensional case. Here, the ground state wavefunction is defined by $\lambda = 1/2$, where λ is the quantum number of the total angular momentum in two dimensions, which corresponds to the total angular momentum quantum number j in three dimensions. The initial wavefunction (in our case the ground state with λ=1/2 and spin-up) of the ion is generated numerically via the spectral method [54] also see section 3.2.3, starting from the total angular momentum eigenfunction $\Psi_\lambda^\uparrow$ with $(\lambda \pm \frac{1}{2}) \in \mathbb{Z}$ analytically given by

$$\Psi_\lambda^\uparrow = \begin{pmatrix} u_0(r)e^{i(\lambda-\frac{1}{2})\phi} \\ 0 \\ 0 \\ u_2(r)ie^{i(\lambda+\frac{1}{2})\phi} \end{pmatrix} \qquad \Psi_\lambda^\downarrow = \begin{pmatrix} 0 \\ -v_0(r)e^{-i(\lambda+\frac{1}{2})\phi} \\ v_2(r)ie^{i(\lambda-\frac{1}{2})\phi} \\ 0 \end{pmatrix} .$$

The functions $u_0(r)$ and $u_2(r)$ can be chosen arbitrarily and are taken here as Gaussian. Upon having discussed some numerical difficulties of the calculation, we focus now on the relevant observable and parameters of our system of interest.

The ionization angle $\underline{\theta}$ in the ion's rest frame with respect to the propagation direction is calculated from the expectation value of the kinetic momentum of the electron in polarization $\underline{p_x}$ and propagation direction $\underline{p_z}$ to be $\tan\underline{\theta} = \underline{p_x}/\underline{p_z}$. The transformation of the ionization angle from the ion's rest frame to the laboratory frame is then ascertained by :

$$\tan\theta = \frac{\underline{p_x}}{\gamma\left(\underline{p_z} - \beta\sqrt{\underline{p_x}^2 + \underline{p_z}^2 + c^2}\right)} . \tag{4.12}$$

The ionization angle in both frames of reference always refers to the laser propagation direction. Additionally, the pulse shape of the laser field is modified to investigate its

Table 4.1: The ionization angles in both the ion's rest frame $\underline{\theta}$ and the laboratory frame θ are given for different field amplitudes in the case of the hydrogen-like ion Ne^{9+} ($Z = 10$). The values of the kinetic momentum for the calculation of the ionization angles were taken at the field maximum of the applied single-cycle laser pulse ($t = T/4$) in the ion's rest frame, where T denotes the laser period. The size of the numerical grid was fixed to 26×26 a.u.

$\underline{E_0}$ [a.u.]	E_0[a.u.]	$\underline{p_x}$[a.u.]	$\underline{p_z}$[a.u.]	$\underline{\theta}$[°]	θ [°]
60	1.00	-0.30	0.0047	89.1	179.99
100	1.67	-8.72	0.55	86.4	179.88
200	3.33	-51.61	9.56	79.5	179.29
300	5.00	-90.47	28.27	72.6	178.76
400	6.67	-122.45	51.35	67.2	178.33
600	10.00	-174.07	101.40	59.7	177.67
800	13.33	-216.18	150.50	55.1	177.18

dependency on the ionization angle. For our calculations the laser frequency $\underline{\omega} = 2.58$ a.u. and the parameter β are fixed, where β arises from a gamma boost of $\gamma = 30$. The ionization angles of the emitted electron and the associated laser field strength in the ion's rest as well as in the laboratory frame are listed in table 4.1 for Ne^{9+} ($Z = 10$). These calculations are made with a static grid size in contrast to the calculations for Zn^{29+} ($Z = 30$), where a "moving-grid" approach is used because of the high momenta that arise. In the "moving-grid" approach only the area in position and momentum space centered around the moving wave packet is considered [87]. Due to the laser magnetic field component, a drift of the electron in the propagation direction is caused, which leads to a decrease of the magnitude of the ionization angle $\underline{\theta}$ towards the propagation direction, as the ratio of the magnitude of the momentum between the polarization and propagation direction decreases comparatively. In both frames, the ion's rest and the laboratory frame, the ionization angles decrease with increasing field strength. Moreover, in the laboratory frame the kinetic momentum of the electron is roughly along the ion beam direction, as a consequence of the strong gamma boost in the laser propagation direction. At low laser field strengths the electron leaves the ionic core predominantly in the laser polarization direction. In contrast, for high laser fields the magnetic component of the laser becomes more important, which consequently guides the ionization angle more in propagation direction. The influence of the scalar potential of the multiply charged

ion on the ionization dynamics can be seen by comparison with a free electron. The ionization angle of the free electron in its rest frame is smaller compared to the initially bound electron for multiply charged ions, as $\theta = \arctan(2c\underline{\omega}/\underline{E_0})$.

The competition between the atomic field strength and the laser field is illustrated by the electron dynamics of the electron in the combined field of the parent ion and the laser. The external laser field mainly influences the electron after it has left the vicinity of the nucleus. This results in a large amplitude of the laser field in polarization and propagation direction, as seen from the plots in Fig. 4.3. These calculated snapshots have been taken at the first field maximum of the one-cycle sin-square laser pulse in the ion's rest frame. For a low laser intensity Fig. 4.3 (a) the main part of the electron density remains with the nucleus. With increasing laser field strength (Fig. 4.3 (b), (c), (d)) the electron density diminishes by moving away both in laser polarization and propagation direction.

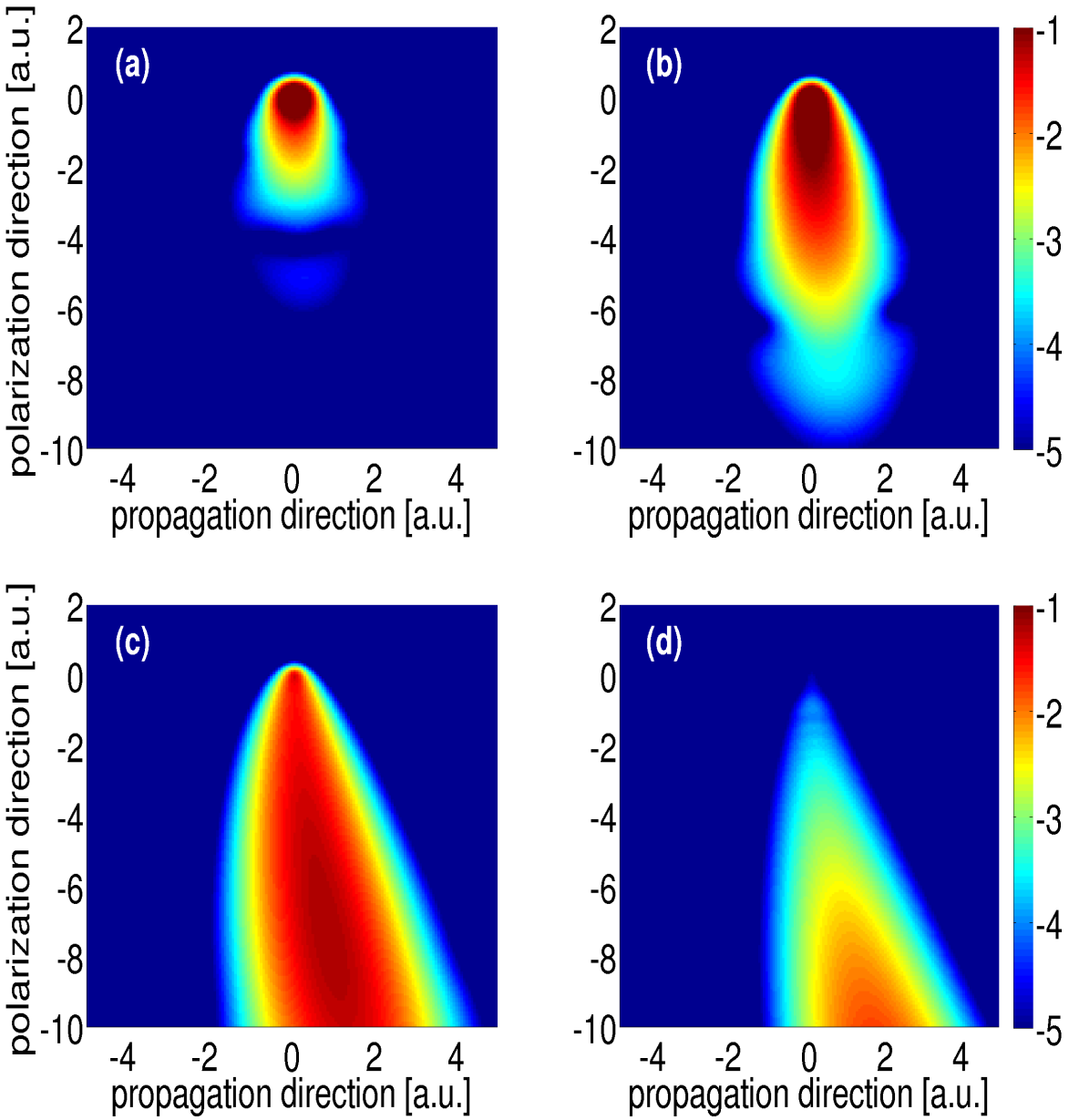

Figure 4.3: Snapshots of the electron probability density in the ion's rest frame are given for Ne^{9+} ($Z = 10$) on a logarithmic scale for different field strengths (a) $\underline{E_0} = 60$ a.u. ($E_0 = 1$ a.u.), (b) $\underline{E_0} = 100$ a.u. ($E_0 = 1.67$ a.u.), (c) $\underline{E_0} = 200$ a.u. ($E_0 = 3.3$ a.u.) and (d) $\underline{E_0} = 300$ a.u. ($E_0 = 5$ a.u.) as a function of the two spatial coordinates x, z. The values in parenthesis are given in the laboratory frame. The hydrogen-like ion was initially prepared to be in the ground state. Depicted is the ionization resulting from a single-cycle sinusoidal pulse without any additional turn-on or turn-off ramp. The snapshots were taken at 1/4 of the laser pulse cycle.

The extension of the electron density distribution in both laser directions is governed by mainly two factors, the high electron velocity in laser polarization direction and the Lorentz force, arising from the magnetic field component of the laser field. The latter induces a substantial acceleration of the electron in laser propagation direction away from the nucleus.

Furthermore, we added an additional turn-on and turn-off phase to the sinusoidal single-cycle pulse which smoothed out the otherwise sharp raising/falling of the field strength. Therewith, the experimentally not well-defined absolute phase of the laser pulse is investigated. We compare three cases, in fact without any additional turn-on phase, with half a cycle turn-on phase and with one cycle turn-on phase. As can be seen from Fig. 4.4, the direction of the electron emission changes according to the chosen fraction of the pulse period. For the additional turn-on pulses, interference structures in the density distribution, which results from the reverse motion of the electron, are visible. For an additional one-cycle turn-on pulse compared, to the case without any additional pulse, the absolute value of the ionization angle changes by two degrees in the ion's rest frame at a fixed field strength of $\underline{E_0} = 100$ a.u. ($E_0 = 1.67$ a.u.). The change of the absolute value of the ionization angle by one degree corresponds to a change of the associated field strength without any additional turn-on pulse of 0.01%.

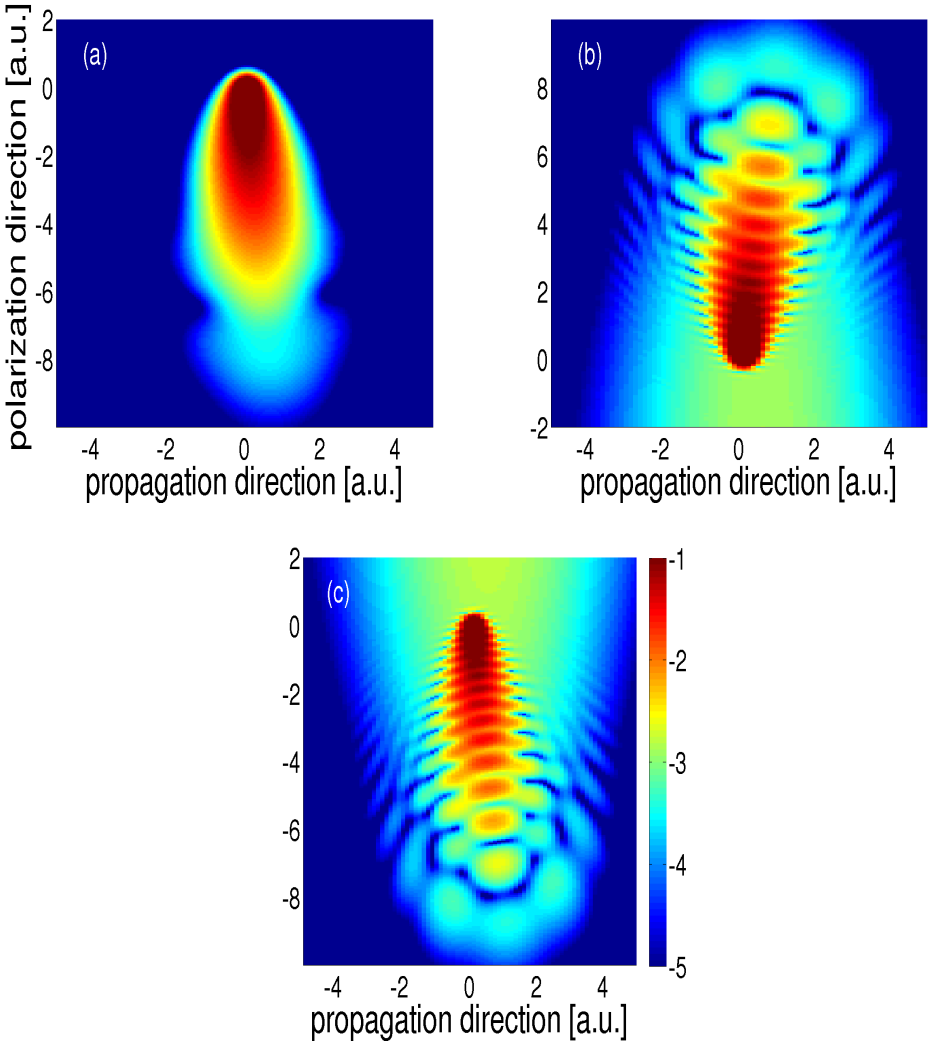

Figure 4.4: Depicted are snapshots at time t of the electron density distribution on a logarithmic scale in the ion rest frame for a charge $Z = 10$ (Ne^{9+}) of a fixed field strength of $\underline{E_0} = 100$ a.u. ($E_0 = 1.67$ a.u.) and a static grid size of 26×26 a.u. The comparison is made between different turn-on phases, which are additionally added to the constant one cycle laser pulse. The pulses are in (a) without any additional turn-on cycle ($t = T/4$), (b) with an additional 1/2 turn-on cycle ($t = 3/4T$), and (c) with an additional turn-on phase of one cycle ($t = 5/4T$) where T denotes the laser period.

$\underline{E_0}$ [a.u.]	E_0[a.u.]	$\underline{p_x}$[a.u.]	$\underline{p_z}$[a.u.]	$\lvert\underline{\theta}\rvert$[°]	θ [°]
1000	16.67	-1.20	0.000094	89.99	179.98
2700	45.0	-6.14	1.67	74.78	179.91
10800	180.0	-297.44	327.77	42.22	175.51
16200	270.0	-444.29	728.82	31.36	173.76
24000	400.0	-513.14	968.83	27.92	172.81
32040	534.0	-560.46	1158.30	25.96	172.20

Table 4.2: The ionization angles in both the ion's rest frame $\underline{\theta}$ and the laboratory frame θ are given for different field amplitudes in the case of the hydrogen-like ion Zn^{29+} ($Z = 30$). The values of the kinetic momentum for the calculation of the ionization angles were taken at 1/8 of the laser period of a single-cycle squared pulse in the ion's rest frame. The underlined values are given in the ion's rest frame, whereas the values that are not underlined indicate the values of the laboratory frame.

To summarize, since the calculation for the ionization angles required considerably less computing time compared to the total ionization yields we decided to employ the somewhat more accurate quantum relativistic calculation. For the calculation of the ionization fraction, in the next section, we have chosen to solve the classical relativistic equation. Furthermore, we verified that there are indeed no other quantum effects of relevance in this regime and have tested with our two-dimensional Dirac code that our relativistic classical Monte-Carlo (CTMC) simulation has delivered correct values in the parameter regime of interest.

4.3.2 Classical relativistic calculation - ionization fraction

A second independent criterion to precisely determine ultra-strong laser intensities is via the calculation of the ionization fraction.

The ionization of a bound electron in the laser field is treated classically when the Coulomb barrier of the bound potential is lowered such that the electron can simply leave the influence of the ionic potential (OTBI regime). The solution of the classical relativistic equation of motion for an electron in a Coulomb potential and a laser field can be generally calculated by using the Monte-Carlo simulation of the classical trajectories, see chapter 3. The numerical details of that are discussed below.

Our observable of interest, the ionization fraction, determined in case of multiply charged

hydrogen-like ions is investigated in the framework of the relativistic phase-space averaging method. The relativistic equations of motion eqs. (3.33) have been solved numerically by the Runge-Kutta method with variable step size. The initial ensemble is in phase space prepared with the relativistic energy for the ground state given by $E_g = c^2\sqrt{1-(Z\alpha)^2}$, with $\alpha = 1/c$, as illustrated in section 3.5.1. The calculations have been performed by an average over thousands of particles until a further increase of the number of trajectories did not lead to a visible change of the properties under consideration. The average correspond to different initial conditions randomly chosen from a microcanonical ensemble, prepared to be in the ground state of the selected hydrogen-like ion with the ground state energy E_g. The small radius for high charge Z (the Bohr radius for hydrogen-like ions is inversely proportional to the ionic core charge Z) is compensated by the substitution of $\mathbf{r}' = \mathbf{r}Z$. Consequently, the numerical difficulty of smaller radii, which is related to a smaller step size chosen by the algorithm, can be avoided. The ionization fraction is defined as the fraction of ionized electron trajectories to the total number of trajectories taken into consideration. An electron is considered to be ionized when its energy $E(t) = (\gamma - 1)c^2 - Z/r$ measured at the end of the pulse is positive and bound of it is negative.

In the following, we describe the procedure of determining ultra-strong laser fields via the calculation of the ionization fraction, which is experimentally a well-established technique. The ionization fraction for several different ions of charge Z is given in Fig. 4.5. For a fixed ionic core charge the ionization fraction grows with a flat profile followed by a rather steep rise ending up with a plateau of complete ionization. The sharp ascent of the ionization curve is the region, where the ionization fraction can be most accurately measured. If an approximate laser intensity range may be expected, an ionic core charge should be selected with maximal slope at this intensity. In case of a mistaken choice, e.g. if an ionization fraction of nearly 1 is measured, no precise statement about the corresponding intensity can be made as the curve is effectively uniform. In this region several laser intensities can be associated to the same ionization fraction. Then our procedure requires that the ionic charge needs to be increased and vice versa for the range around a very small ionization fraction. This procedure needs to be continued until the ionization fraction is in the

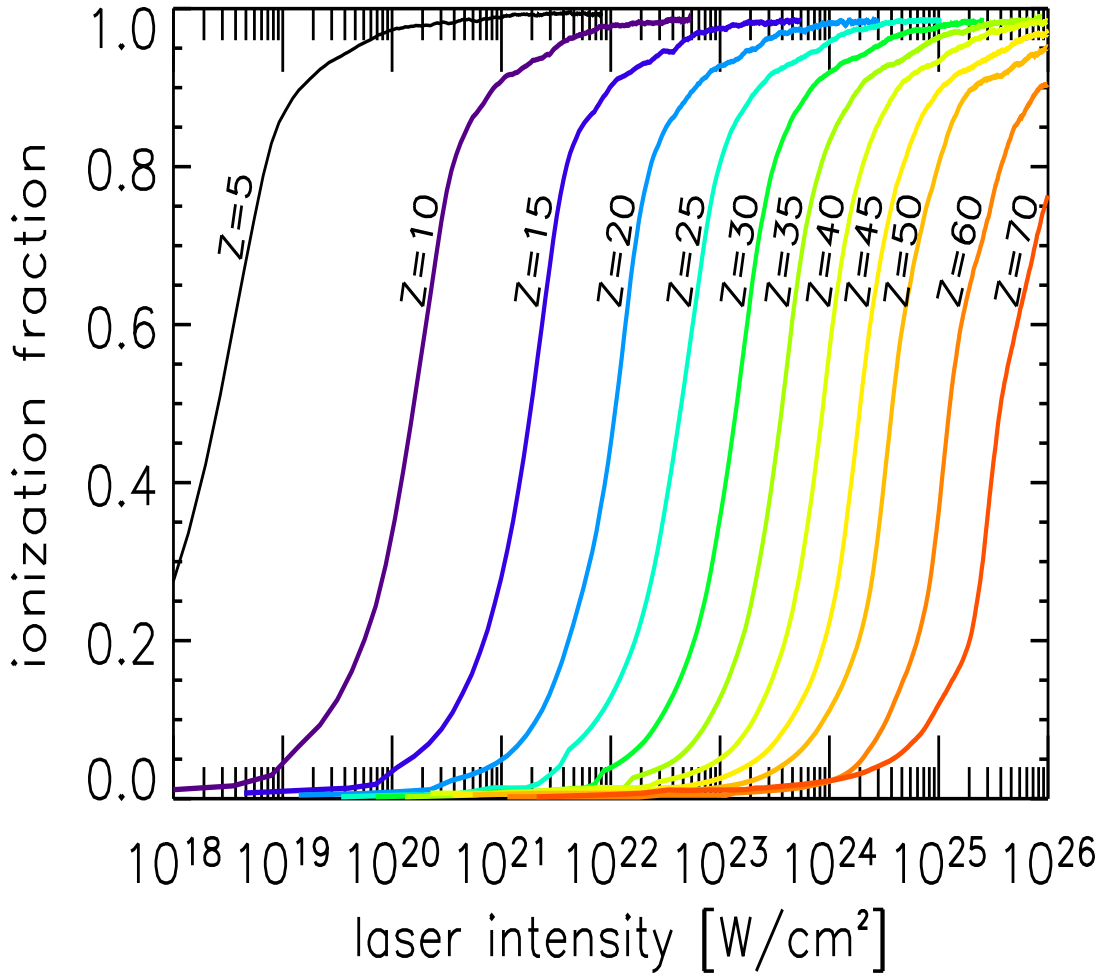

Figure 4.5: Plotted is the ionization fraction for several different hydrogen-like ions Z as a function of the maximal laser intensity in the laboratory frame. The ionization fraction is calculated at the end of a single-cycle square-shaped laser pulse of wavelength $\lambda = 1054$nm (frequency $\omega = 0.043$ a.u.).

narrow range of the sharp ascent of the ionization curve (narrow intensity range), where the corresponding laser intensity can be most precisely determined.

At the steepest points of the sharp ascents for all investigated ionic charges Z we can read off the ionization fraction and laser intensity for each curve in Fig. 4.5 and obtain Fig. 4.6. The unknown laser intensity can now be more effectively determined. In a first step a particular ion needs to be selected, whose ionization fraction should then be measured. As a possible first guess, we refer to the dashed line of Fig. 4.6, which indicates the corresponding ionic charge of the expected intensity range. Here, for example, an intensity of $I = 10^{23}\mathrm{W/cm}^2$ corresponds to an ionic charge of $Z = 30$, which would be

a proper candidate to begin with if an intensity around $10^{23}\mathrm{W/cm}^2$ is assumed. In a second step, the ionization fraction of the selected fixed ionic charge should be measured. If the ionization fraction is higher than the corresponding one depicted in Fig. 4.6 (solid line) then the measurement has to be repeated for a higher ionic charge and vice versa for a smaller ionization fraction. This procedure has to be continued until the ionization fraction matches with the corresponding value given by Fig. 4.6 for the respective ion. From the final charge Z, the corresponding laser intensity can then be read off via the dashed curve of Fig. 4.6.

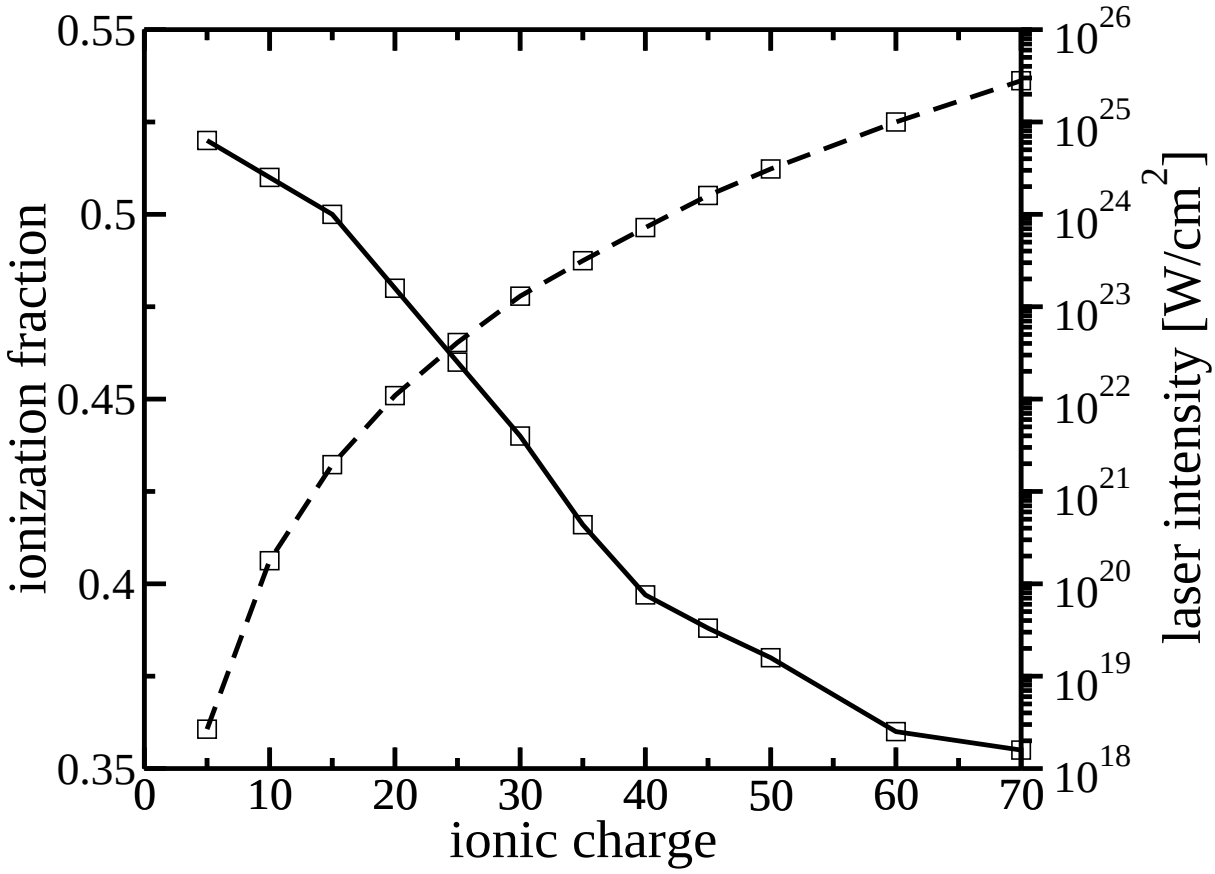

Figure 4.6: The solid line defines the most sensitively measured ionization fraction (left axis), whereas the dashed line shows the corresponding laser intensity (right axis) as a function of the respective optimal ionic core charge Z. The laser field parameters are the same as given in Fig. 4.5. The squares indicate the deduced points from Fig. 4.5.

4.4 Influence of quantum effects, laser frequency, pulse shape, length and carrier phase

After having introduced the method to sensitively determine the laser field strength we examine now the dependence of the ionization fraction via the relativistic classical trajectory Monte-Carlo (CTMC) simulation on the characteristic laser parameters, i.e. the frequency and on the pulse shape, length and carrier phase exemplarily for an ionic core charge of $Z = 10$. Additionally, the influence of quantum effects are studied by means of comparing the relativistic CTMC simulation with the quantum Dirac calculation.

4.4.1 Investigation of the pulse length

We start with the investigation of the pulse length, which is varied between 1 and 10 laser cycles for two different pulse shapes, a sin-square and a sin-sin^2 pulse. Hence, the electric field of the sin-square pulse is defined as $\mathbf{E}(\eta) = E_0 \sin(\eta)\mathbf{e_x}$ and the sin-sin^2 pulse as $\mathbf{E}(\eta) = E_0 f(\eta) \sin(\eta)\mathbf{e_x}$ with $\eta = \omega t - \mathbf{kr}$ and $f(\eta)$ correspondingly given in section 3.3.1. Taking the ionization fraction at the most sensitive point of the one-cycle sinusoidal pulse as a reference the corresponding peak laser intensities of the different pulse lengths can be determined. In case of a sin-square pulse the laser intensity differs at most by 10% in the case of the 10 cycle pulse. The reason is an increase in the appropriate pulse energy given to the electron by the increased pulse length. Therefore, the electron has a higher momentum at the end of the pulse to escape from the nucleus, which leads to a shift to smaller laser intensities for the most sensitive measured ionization fraction. The ionization fraction is measured under the condition of an adiabatic field (atomic frequency on the first Bohr orbit is much higher than the laser field frequency) render it only depending on the applied field amplitude which is the same for all three pulse lengths in the case of a sin-square pulse. The measured deviation of the ionization fraction resulting from the different pulse energies of the various pulse lengths which play a minor role in the considered frequency regime compared to the condition of maximal field strength within the pulse as can be seen from the investigation on the $\sin - \sin^2$ pulse.

For more realistic sin^2-shaped pulses, the additionally added turn-on and -off phases to the

constant pulse part smooth out the sharp rise and fall of the maximal field strength compared to the sin-square pulse studied before. Here, attaining the maximal field strength by the pulse, renders a great difference in the ionization fraction. In Fig. 4.7 (a) those different pulse lengths are depicted for the $\sin - \sin^2$ pulse. It shows that the maximal field strength compared to a corresponding sin-square pulse is not reached in case of few cycle pulses but for many cycle pulses, e.g. 10 cycles or more. The measurements of the ionization fraction performed for the different pulse lengths are displayed in Fig. 4.7 (b) as a function of the applied laser intensities. In case of few cycle laser pulses, the corresponding ionization curve is shifted towards higher peak laser intensities, at most in the case of the one-cycle pulse by up to 47% for the most sensitive measured intensity point. This difference gains smaller with increasing number of laser cycles. The reason is that the maximal field strength amplitude of a corresponding sin-square pulse is approached in the limes of large numbers of laser cycles, which leads to a higher ionization fraction for the same field strength. Hence, the number of laser cycles together with the attained maximal field intensity during the laser pulse has a large influence on the measurement of the ionization fraction.

The situation changes in the case of fast oscillating fields. In comparison to the optical frequency regime in the XUV regime and above, the higher laser field amplitude is not sufficient to ionize the electron, instead also the ionization time needs to be large enough for the electron to have enough time to tunnel through the Coulomb barrier before the oscillating electric field changes its direction again. A more detailed analysis is provided in the paragraph of frequency dependence below.

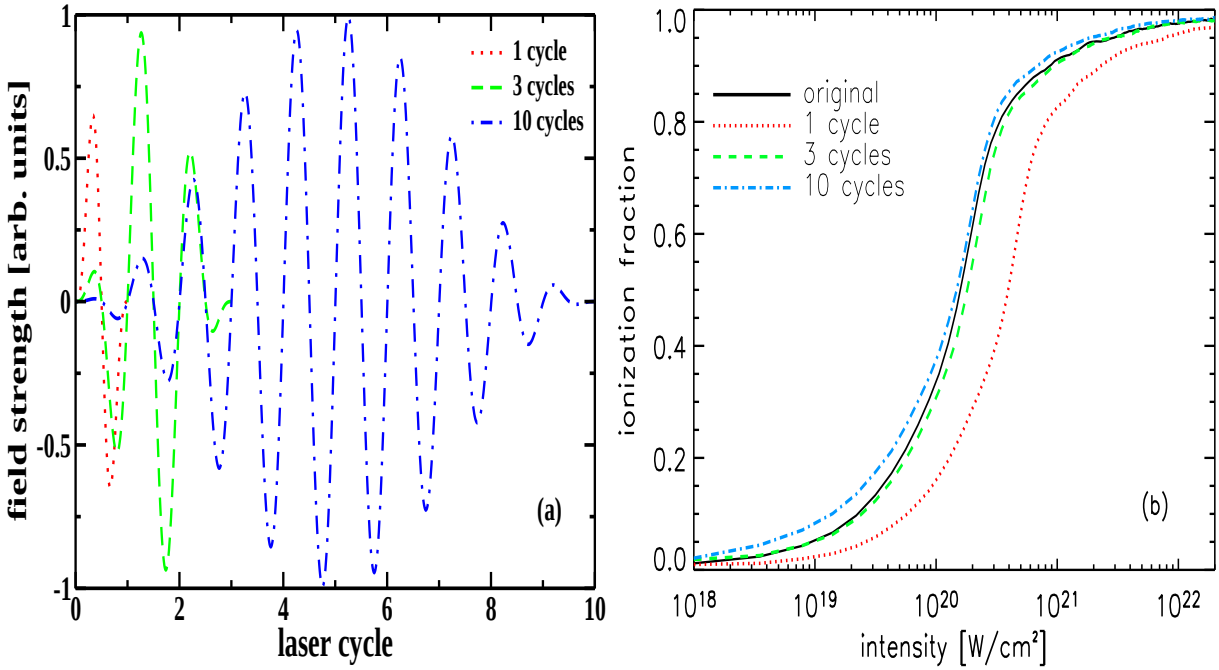

Figure 4.7: In (a) the various pulse cycles of a $\sin - \sin^2$-shaped pulse are depicted. The corresponding ionization fraction for the different pulse cycles and the original one-cycle sin-square pulse for comparison are shown in (b) for an ionic core charge of $Z = 10$.

4.4.2 Investigation of the carrier phase

For further investigations of the characteristic laser parameters we changed the pulse phase by a fraction of π from zero to π as seen from Fig. 4.8 (a). Two of the selected pulse phases $\phi_0 = 0$ and $\phi_0 = \pi$ have the same amplitude but different sign. Therefore, it is interesting to see whether the maximal amplitude of the pulse has a greater impact on the ionization fraction or the phase of the pulse. For a sin-square one-cycle pulse the intensity changes at most by 33% towards smaller intensities in case of a maximum phase shift of $\phi_0 = \pi/2$ as the maximum field strength is reached later in time. With a further increase in the pulse length towards a 10 cycle sin-square pulse no better agreement is achieved. More interesting is the effect of the phase change on more realistic $\sin - \sin^2$ pulses. Here, the influence of the phase leads as well to an increase of the laser intensity compared with the sin-square laser pulse. This increase of the laser intensity originates from the instant maximum laser field strength reached during the pulse as already seen from the study of the pulse length. A good example are the phases $\phi_0 = 0$ and $\phi_0 = \pi$.

They both have the same amplitude but are totally different in shape see Fig. 4.8 (a), (b). Their corresponding ionization fraction are nevertheless equal for both phases as depicted in Fig. 4.8 (c), (d). The importance of the maximum field amplitude can also been seen by comparing the ionization fraction of the original sin-square pulse with the $\sin - \sin^2$-shaped pulse with a phase shift of $\phi_0 = \pi/2$. In both cases the maximum field strength is obtained during the pulse but at very different points in case of the one-cycle $\sin - \sin^2$-shaped pulse with a phase shift of $\phi_0 = \pi/2$ once and twice in case of the sin-square pulse, nevertheless their most sensitive field intensity is the same.

To summarize the phase difference has not such an important influence on the ionization fraction as the reaching of the maximum field strength has. Altogether, the phase difference effect for $\sin^2$-shaped pulses has a maximum for the one-cycle pulse as it is already the case for the pulse length and is calculated to be at most for a phase shift of π to be 50% decreasing to 15% in case of three-cycle pulse, which results from the smaller field strength. A phase shift of $\pi/4$ leads to a shift in intensity of 20% in case of the one-cycle $\sin - \sin^2$-shaped pulse compared to the original sin-square pulse. In general the phase of the pulse has a minor influence on the ionization fraction than the pulse length has.

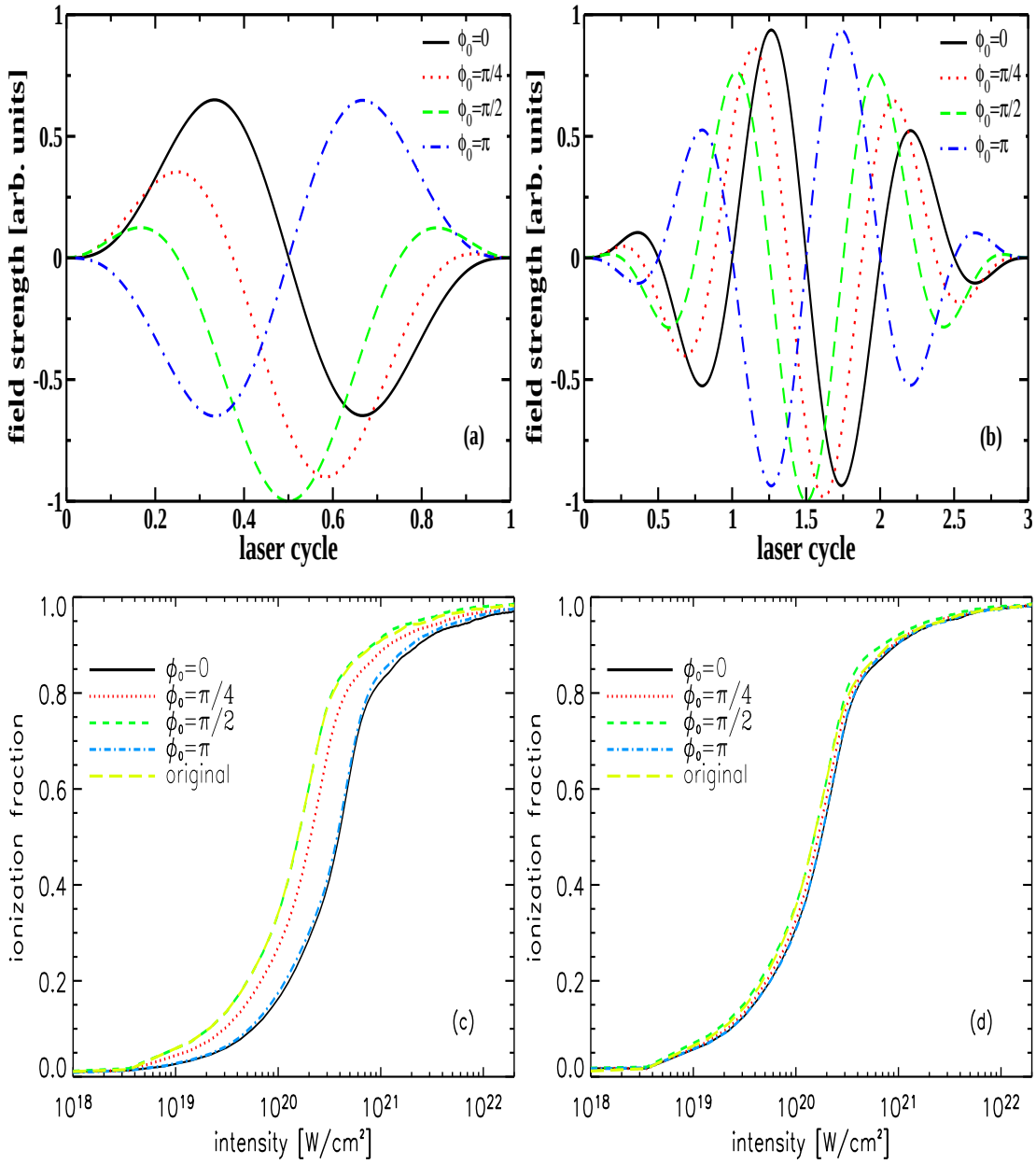

Figure 4.8: Depicted are the different laser pulse phases for one-cycle (a) and three-cycle (b) pulses of $\sin - \sin^2$ shape. The behavior of the corresponding ionization fraction is depicted for the one-cycle pulse in (c) and the three-cycle pulse in (d). The yellow long dotted line corresponds to the original sin-square one-cycle pulse as defined in the text, in case of an ionic core charge of $Z = 10$.

4.4.3 Investigation of the pulse shape

The influence of the shape of the laser pulse is studied below. Therefore, the variation of three different types of laser pulse shapes, namely a sin-square, a $\sin - \sin^2$ and a $\cos - \sin^2$ -shaped pulse, which are shown in Fig 4.9 (a), (b) for a one-cycle and three-cycle pulse, respectively, are investigated. In case of a one-cycle pulse the maximal field strength is reached for the sin-square cycle pulse twice and for the $\cos - \sin^2$ shaped pulse once. Thereby, the number of maxima obtained by the laser field has no influence on the ionization fraction which both of them equally led to the same corresponding laser intensity. The agreement can be clearly seen in Fig 4.9 (c). In comparison, the $\sin - \sin^2$ pulse has a much smaller corresponding ionization fraction, due to the smaller corresponding laser field strength of the pulse, resulting in a 50% higher laser intensity for the most sensitive measured ionization fraction. The situation changes with increasing laser cycles leading to a difference of only 10%.

Therefore, we conclude that for the measurement of the ionization fraction at the end of the laser pulse only the maximal field strength during the laser pulse is of main importance. An especially huge difference is made in the case of single or few cycle pulses. With increasing laser pulse cycles the differences are decreasing as the maximal laser field strength is reached as well. This is true as long as the laser field frequency is much smaller than the underlying atomic frequency.

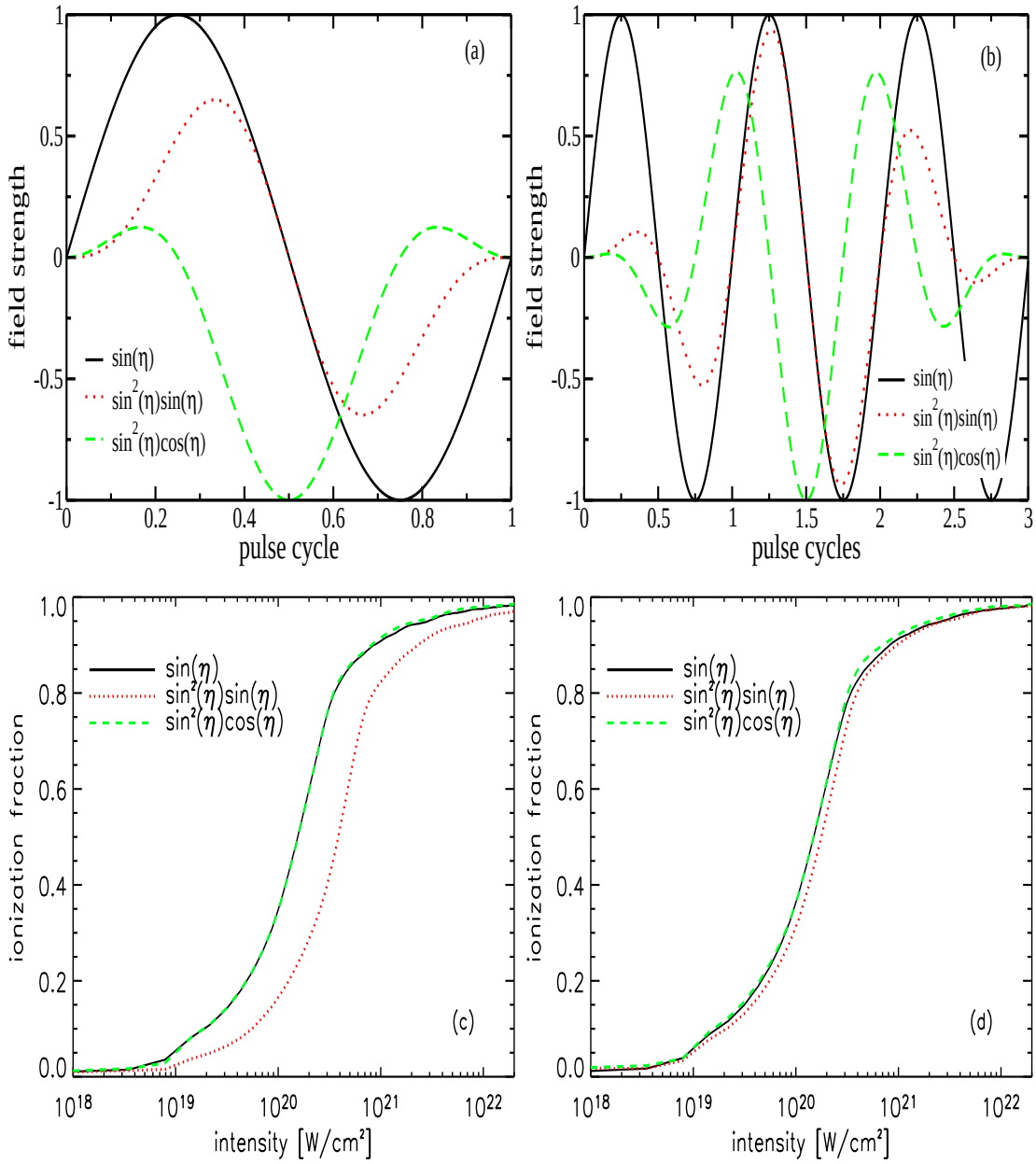

Figure 4.9: Depicted are the laser fields in case of the ionic core charge $Z = 10$ for different kind of pulses, namely a sin-square, $\sin - \sin^2$ and $\cos - \sin^2$ pulse in the case of one-cycle (a) and three laser cycles (b). The behavior of the corresponding ionization fraction is depicted for the one-cycle pulse in (c) and the three-cycle pulse in (d).

4.4.4 Investigation of the laser frequency

The proposed method of determining the ionization fraction of multiply-charged hydrogen-like ions and therewith the measurement of the maximal laser intensity can be extended to currently available and future sources of high frequencies (UV, XUV frequency range). The typical wavelengths of these new sources are $\lambda = 32$ nm (FEL source [7], $\omega = 1.4$ a.u.), $\lambda = 6.5$ nm (FLASH source [8], $\omega = 7$ a.u.) and $\lambda = 0.4$ nm (XFEL source [9], $\omega = 114$ a.u.). The corresponding ionization fraction for these different frequencies as a function of the applied laser intensities are given in Fig. 4.10. For comparison of the influence of the frequency on the ionization fraction we selected three different hydrogen-like ions with the ionic charges of $Z = 10$, 30, 50 in case of a one-cycle sin-square pulse. The ionization fraction curves for low ionic charge e.g. $Z = 10$ are shifted towards higher intensities with increasing frequency. However, the typical slope remains the same. The dominating ionization process in this case is multiphoton ionization which is strongly suppressed and therefore gives a low ionization fraction. The highest deviation can be seen for the frequency of the XFEL source ($\omega = 114$ a.u.). In this case the ratio η of the laser frequency towards the atomic frequency is not anymore smaller than 1, i.e. the adiabaticity of the field is no longer guaranteed. Therefore, the electron on the first Bohr orbit sees the temporal variation of the amplitude of the oscillation laser field. For the ionization process this means that in addition to the maximum field strength, the temporal variation of the laser field influences the most sensitive measured point of laser intensity. With increasing ionic charges Z the atomic field strength increases and therewith η becomes again smaller than 1. For high enough ionic charges Z, the adiabatic condition can be again satisfied, inducing a decrease of the differences of the ionization fraction between the different frequencies.

We conclude that for low ionic charges Z and high enough laser field strength, the adiabatic regime is not valid anymore, resulting in a two orders of magnitude higher laser intensity for an ionic core charge of $Z = 10$ and a XFEL frequency of $\omega = 114$ a.u., which can be changed by selecting higher charges, where the atomic frequency is again higher compared to the laser frequency.

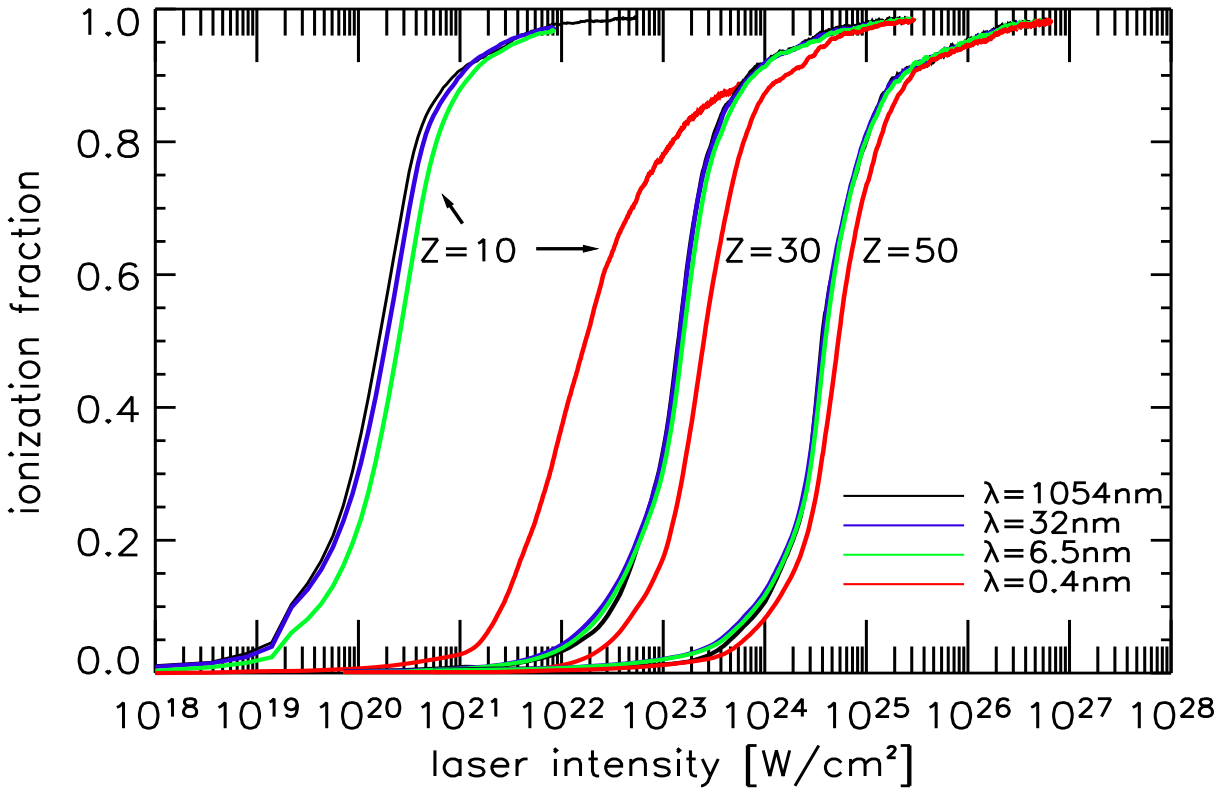

Figure 4.10: Plotted is the ionization fraction for several different wavelengths as a function of the laser intensity in the laboratory frame. For comparison three different ionic charges $Z = 10$, 30, 50 are taken here. The with the two arrows marked curves belong to the same ionic charge $Z = 10$.

4.4.5 Quantum versus classical calculation

In the following the ionization fraction obtained by the classical relativistic Monte-Carlo simulation is investigated by comparison with additional calculations.

To show that for our method of most sensitively measuring ultra-strong laser intensities, tunneling ionization is of no relevance, we compare our results with the analytical given tunnel ionization formula 4.6. The results of the corresponding ionization fraction of both calculations is displayed in Fig. 4.11 in the case of the ionic core charge of $Z = 10$ (Fig. 4.11 (a)) and $Z = 30$ (Fig. 4.11 (b)).

In the regime around $\gamma = 0.1$, where tunneling dominates, i.e. for small ionization fraction, both calculations show similar ionization yields. However, with rising ionization and increasing intensity we note clearly deviating results. In order to discuss the applicability

of the tunneling yields we have indicated two dashed lines in above Fig. 4.11. For the left dash line, i.e. indicating $\gamma = 0.1$ the tunneling formula applies, however, for the right one and beyond it certainly does not. This line marks the border to the over-the-barrier regime, where the tunneling barrier is exactly zero. Thus for higher intensities and even somewhat below one cannot apply the tunneling formula because tunneling does not occur or does not describe the dominating mechanism. In the parameter regime of laser intensities of interest here (the over-the-barrier regime) with maximal slope (indicated with a cross in the Fig. 4.11), where the sensitivity in the ionization with regard to derivations in the intensity is maximal, tunnel ionization does certainly play no role. Moreover, this comparison defines the range of validity of the analytical given relativistic

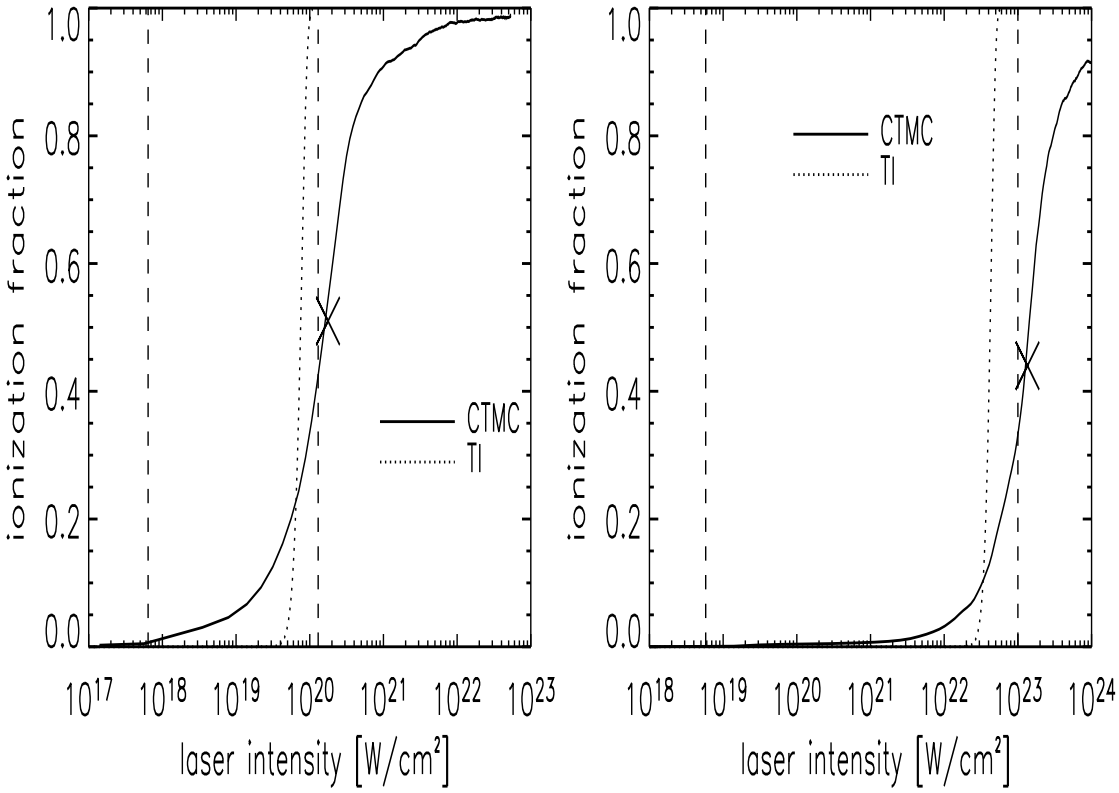

Figure 4.11: Plotted is the ionization fraction of the charge $Z = 10$ (left plot) and $Z = 30$ (right plot) for our CTMC calculation (solid line) and the semiclassical relativistic tunnel ionization (TI) fraction (dotted line) of Eq. (4.6). The dashed lines mark the corresponding tunneling regime with the lower boundary indicating the Keldysh parameter $\gamma = 0.1$ and the upper boundary the critical relativistic barrier suppression field intensity according to [76]. The most sensitively measured intensity value calculated by the CTMC method, according to Fig. 4.5 is denoted by X, described in the next section.

tunnelrate formula.

Additionally, in order to show that our CTMC calculation models the ionization behavior correctly and quantum mechanical effects are of minor importance in the regime of over-the-barrier ionization here, we render a comparison in two dimensions with the quantum mechanically correct Dirac equation. To get a quantum mechanically appropriate computation time for the Dirac equation the frequency has been increased for both calculations to $\omega = 7$ a.u. for the present investigation. The primary results displayed in Fig. 4.12 show that for low ionic core charges Z, the calculated ionization fraction obtained via the Dirac equation, gives smaller values for the CTMC simulation compared to the quantum Dirac calculation. The reason is the ionization via tunneling, which is intrinsically included in the quantum mechanic calculation starts to happen before the electron classically leave the ion. However, this difference in the ionization fraction seems to be decreasing with increasing ionic core charge, resulting in a lower probability of tunnel ionization. For $Z = 10$ the classical CTMC calculation leads to uncertainties for the most sensitively measured laser intensity of the order of 40% in comparison to the Dirac simulation and thus smaller than the uncertainty via lacking information of the laser pulse shape, length and carrier phase.

Quantitative non-negligible deviations of the ionization fraction due to QED effects are also likely to result especially starting at about $Z = 50$, rendering our evaluations, however, still useful for order of magnitude estimations.

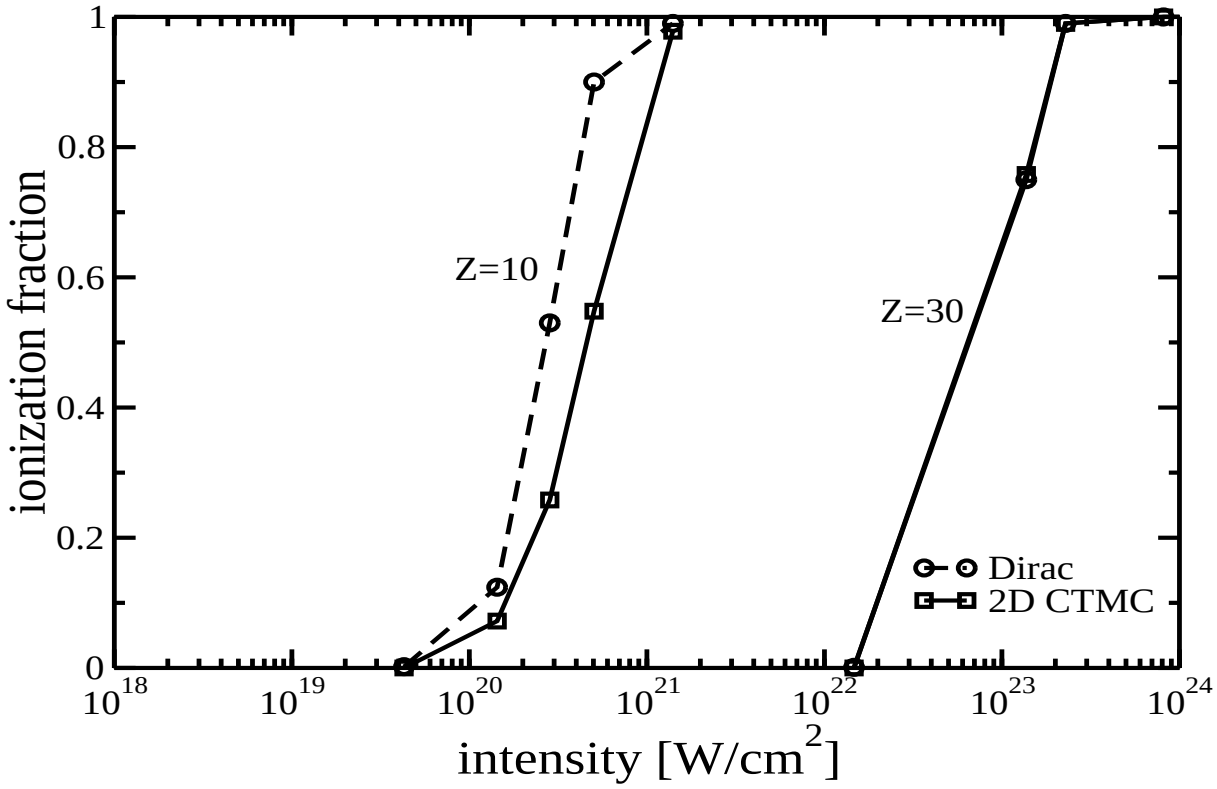

Figure 4.12: Displayed are the calculations of the ionization fraction for some intensities in the case of the ionic core charges $Z = 10$ and $Z = 30$ for a one-cycle sinusoidal laser pulse of frequency ω=7 a.u.

4.5 Conclusion

To summarize, by carrying out our classical relativistic Monte-Carlo simulation via the calculation of the ionization fraction, we have investigated the validity of the analytically given relativistic tunnel rate formula.

It has been shown that the analytical result and the CTMC simulation are quite similar in the experimental relevant range for tunnel ionization. However, close to the critical field strength for over-the-barrier ionization the analytically given ionization fraction sharply increases leading the corresponding ionization fraction questionable. Moreover, the importance of relativistic effects for multiply charges hydrogen-like ions gain of importance above an ionic core charge of $Z = 10$.

Furthermore the ionization fraction and the ionization angle has been investigated both with a classical relativistic Monte-Carlo simulation and a quantum Dirac calculation in two

dimensions. Based on the study of the ionization fraction we have presented a new method to determine most sensitively the laser intensity by measuring the ionization fraction in multiply charged hydrogen-like ions. We have shown that the proposed method is in principle not limited by any ultra-strong laser field apart from the limit of the ionic field strength via the critical charge of $Z = 137$, which provides instable ions. The dependence of this method on the typical laser parameters like the phase, shape and pulse length have been studied and the extension of the method from the optical frequency to the XUV frequency range are shown. Especially, it could be shown that for high XFEL laser frequencies $\omega = 114$ a.u. the measurable laser intensity range is increased by two orders of magnitude when leaving the adiabatic frequency regime in case of low ionic core charges Z. Additionally, we verified the validity of the classical trajectory Monte-Carlo simulation in the regime of interest (over-the-barrier ionization) by comparing the ionization fraction via a two dimensional calculation for both the Dirac equation and the classical relativistic equations of motion.

Chapter 5

Bound dynamics of multiply charged ions

5.1 Motivation

The bound dynamics in conventional quantum optics with weak laser fields deals with a quantized radiation field [91]. In this chapter however, we treat the interaction of matter with the radiation field semiclassically, where the field is assumed to be classical and the atom is considered quantum mechanically. Possible differences arising from this treatment in comparison with a quantized field can be seen from the interaction of a simple two-level system with a single-mode radiation. Semiclassical theory predicts Rabi oscillations ocurring from the population inversion between the two levels by neglecting all decay processes. On the contrary, in quantum theory the atomic inversion shows collapse and revival phenomena [92] due to the quantized field. However, the study of these quantum phenomena is not the aim of this chapter. Instead, we examine only systems interacting with strong and short laser pulses, where the dynamics is fully relativistical and therefore all kinds of spontaneous emission processes are negligible.

One of the main properties in the investigation of bound dynamics is the shift of energy eigenstates in strong oscillating laser fields. This ac-Stark effect can be described as the interaction energy of the electric dipole moment of the atom with the field. It is nowadays possible to calculate the ac-Stark splitting in second-order perturbation theory for resonant multiphoton transition of highly charged ions [93] beyond the dipole approxima-

tion. Unfortunately, no analytical expressions are known for a two-dimensional soft-core potential in ultra-strong laser fields, which is studied here.

5.2 Transitions beyond the dipole approximation

Before treating our system by taking all relativistic orders into account, a brief overview of the analytic solution of the simplest two-level system is given in the following. Therefore, the coupling of a two-level system to a single mode of an external laser field [94] of frequency ω is considered. However, in realistic atomic systems consisting of many levels a two-level description of the atomic systems is only valid, if the two levels are resonantly or near-resonantly coupled to the driving field, while all other levels are detuned. We define the lower state by n with the energy E_n and the upper state by m with the energy E_m. Resonance occurs when the following conditions are satisfied:

$$\Delta = \omega_{mn} - \omega \quad \ll \quad \omega \tag{5.1}$$

$$|d_{mn}E| \quad \ll \quad \omega_{mn} \ , \tag{5.2}$$

with ω_{mn} to be the transition frequency between the states n, m and d_{mn} the dipole matrix element of the field free states. Additionally, to the resonance condition the intensity of the applied laser field strength E needs to satisfy the condition $E \ll E_{at}$, where E_{at} is the atomic field strength. This condition ensures that the bound dynamics of the system and not any ionization into the continuum is studied.

In the following, the analytic semiclassical solution of the interaction of an ideal two-level system with a single-mode field $E(t) = E_0 \cos(\omega t)$ in dipole approximation is examined. The state vector of the two-level system is expressed by:

$$|\Psi(t)\rangle \quad = \quad \sum_k C_k(t) e^{-iE_k t} |k\rangle \tag{5.3}$$

$$= \quad C_n(t) e^{-iE_n t} |n\rangle + C_m(t) e^{-iE_m t} |m\rangle \tag{5.4}$$

with the propability amplitudes $C_n(t)$ and $C_m(t)$ of the lower and upper state, respectively. The time evolution of the wavefunction by the Schrödinger equation can be written as:

$$i\frac{\partial \Psi(\mathbf{r},t)}{\partial t} = H\Psi(\mathbf{r},t) = (H_{at} + H_{int}(t))\Psi(\mathbf{r},t) \ , \tag{5.5}$$

where $H_{at} = \omega_{nm}|m\rangle\langle m|$ (energy of the lower state n is chosen to be zero) is the unperturbed atomic part of the Hamiltonian and $H_{int}(t) = \mathbf{d} \cdot \mathbf{E}(\mathbf{t})$ describes the interaction Hamiltonian. Substituting the expansion given in Eq. (5.4) into the time-dependent Schrödinger equation (5.5) we obtain a set of coupled first order differential equations of the amplitudes:

$$\frac{dC_n}{dt} = -iE_0 cos(\omega t) d_{nm} e^{i\omega_{nm}t} C_m \tag{5.6}$$

$$\frac{dC_m}{dt} = -iE_0 cos(\omega t) d^{\star}_{nm} e^{-i\omega_{nm}t} C_n \tag{5.7}$$

or by expanding the term $\cos(\omega t)$ we obtain

$$\frac{dC_n}{dt} = \frac{i}{2} E_0 d_{nm} \{e^{i(\omega_{nm}-\omega)t} + e^{i(\omega_{nm}+\omega)t}\} C_m \tag{5.8}$$

$$\frac{dC_m}{dt} = \frac{i}{2} E_0 d^{\star}_{nm} \{e^{-i(\omega_{nm}-\omega)t} + e^{-i(\omega_{nm}+\omega)t}\} C_n \; . \tag{5.9}$$

Applying the rotating wave approximation, i.e. neglecting the fast oscillating terms $\omega_{nm} + \omega$. The set of equation becomes

$$\frac{dC_n}{dt} = \frac{i}{2} E_0 d_{nm} \{e^{-i(\omega_{nm}-\omega)t}\} C_m \tag{5.10}$$

$$\frac{dC_m}{dt} = \frac{i}{2} E_0 d^{\star}_{nm} \{e^{-i(\omega_{nm}-\omega)t}\} C_n \; . \tag{5.11}$$

Integrating Eq. (5.10,5.11) and introducing the detuning $\Delta = \omega_{nm} - \omega$ with the initial condition at time $t = 0$ to be $C_n(0) = 1$, $C_m(0) = 0$ gives the solution of the population in the upper state

$$C_m(t) = -i \frac{d^{\star}_{nm} E_0}{\Omega_R} e^{\frac{i\Delta t}{2}} \sin\left(\frac{\Omega_R t}{2}\right) \; , \tag{5.12}$$

where

$$\Omega_R = \sqrt{\Delta^2 + (d^{\star}_{nm} E_0)^2} \tag{5.13}$$

is the effective Rabi frequency. The probability of the atom to be in the upper state m (excited state) is

$$P(t) = |C_m(t)|^2 = \left(\frac{d^{\star}_{nm} E_0}{\Omega_R}\right)^2 \sin^2\left(\frac{\Omega_R t}{2}\right) \tag{5.14}$$

In Fig. 5.1 the probability amplitude P(t) is plotted for various values of the detuning Δ. For an increase in the detuning the probability of finding the atom in the upper

state is decreasing. The process described above is called Rabi oscillation resulting from the process of stimulated emission and absorption of photons. During the oscillation of the population between the two states the atom is in a superposition of the lower and upper state. The Rabi frequency is proportional to the strength of the radiation field. The proportionality factor thereby is the transition dipole matrix element $\mathbf{d} = e\mathbf{r}$. The quantum mechanical analogon to the Rabi model with a quantized atom is the Jaynes-Cumming model [95]. For the analytic solution the laser pulse is assumed to be infinite. In the next sections we investigate the interaction of bound wavefunctions with a finite laser pulse.

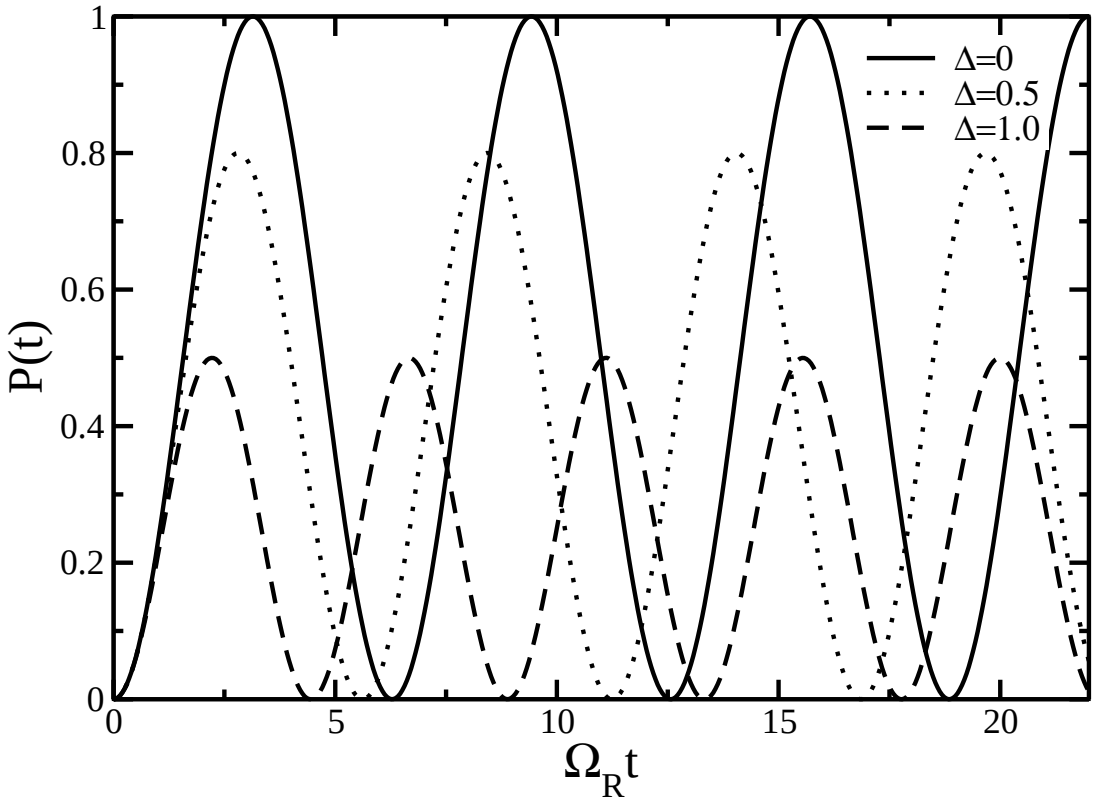

Figure 5.1: Schematic diagram of Rabi oscillations for different values of the detuning Δ of a resonantly driven two-level system.

5.2.1 One photon transition

So far we have discussed the simple two-level model, now we turn to more elaborated analyses investigating the interaction of resonantly coupled two-level systems in multiply charged hydrogen-like ions with a single-mode laser field by means of semiclassical theory, i.e. the bound states are treated quantum mechanically by means of the Dirac equation and the laser field classically. Thereby, the bound states are represented by the generated wavefunction of the unperturbed two-dimensional soft-core potential of Eq. (3.2). The laser field is taken to be finite and has a $\sin^2$-shaped pulse, for details see section 3.3.1. The whole bound dynamics is then given by the full relativistic wavefunction propagating on a two-dimensional numerical grid. Therefore, the following assumptions made in the analytic approach can be neglected.

Firstly, the analytic treatment was done in the scope of non-relativistic theory for atoms with a charge of $Z = 1$ by solving the Schrödinger equation. The systems we are studying here involve higher nuclear charges ($Z > 1$), where relativistic effects have to be considered. These are taken into account by the solution of the Dirac equation. Secondly, we have extended the for the analytic solution necessary dipole approximation of resonantly driven systems, by keeping the spatial dependence of the laser field. The phase η of the laser field $E(t) = E\cos(\eta)$ becomes then $\eta = \omega t - \mathbf{kr}$ instead of $\eta = \omega t$ as before. Thirdly, the rotating wave approximation has not been applied, i.e. we keep all the terms including these with high oscillations.

However, for our analysis we restrict ourselves to the near resonant photon regime, where only a few levels are involved in order to keep the whole bound dynamics feasible. The population probability amplitude is then numerically determined by a projection of the actual wavefunction on the bound state eigenwavefunction. The therefore necessary bound eigenstates and their associated wavefunctions of the selected multiply charged hydrogen-like atomic core of charge Z are generated via the spectral method see section 3.2.3 before applying the laser field. Even though we can chose many states as initial state in our present analysis we have taken the ground state to be the initial state. In the following, we investigate the bound dynamics of a bound transition resonantly driven by

a laser field. Hereby, any spontaneous decay processes of excited states are not considered. Once the external laser field is switched off the population numerically remains in their eigenstates. The population dynamics at any time t is then obtained by projecting the actual wavefunction, which is distorted through a superposition of the populated many levels system, on the field-free bound state of interest. The square of this projection defines then the probability to find the electron in the considered state. Such a population dynamics of some states is illustrated in Fig. 5.3. Here the transition from the initially populated ground state $|1S_{1/2}\rangle$ to the higher lying state $|3P_{3/2}\rangle$ is resonantly driven with a laser frequency corresponding to a one-photon transition between those states. A change of the population from the ground state $|1S_{1/2}\rangle$ to the $|3P_{3/2}\rangle$ excited state is clearly visible, as the whole population moves from the ground state into the excited state and back again. Additionally, the population dynamics of the $|3S_{1/2}\rangle$ state has been plotted to show that only a small percentage of the population is excited from the $|1S_{1/2}\rangle$ state into the above $|3S_{1/2}\rangle$ state. This $|1S_{1/2}\rangle \leftrightarrow |3S_{1/2}\rangle$ transition is in fact dipole forbidden. The non-zero probability amplitude results from the transition of the $|3P_{3/2}\rangle$ to the $|3S_{1/2}\rangle$ state. As this transition is not resonantly coupled to the laser field its population is rather low. The oscillation in the probability amplitude arises from the non-resonantly coupling of the laser field to the $|3S_{1/2}\rangle \leftrightarrow |3P_{3/2}\rangle$ transition. From the Rabi frequency of the resonantly driven $|1S_{1/2}\rangle \leftrightarrow |3P_{3/2}\rangle$ transition the one-photon transition dipole matrix element is calculated according to Eq. (5.13) to be $d_R = 0.027$ a.u.

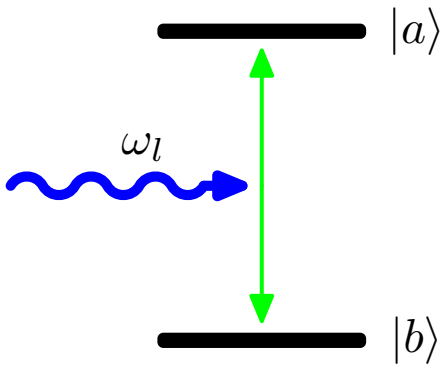

Figure 5.2: Schematic diagram of the interaction of a two-level system with the laser field of the one-mode frequency ω_l .

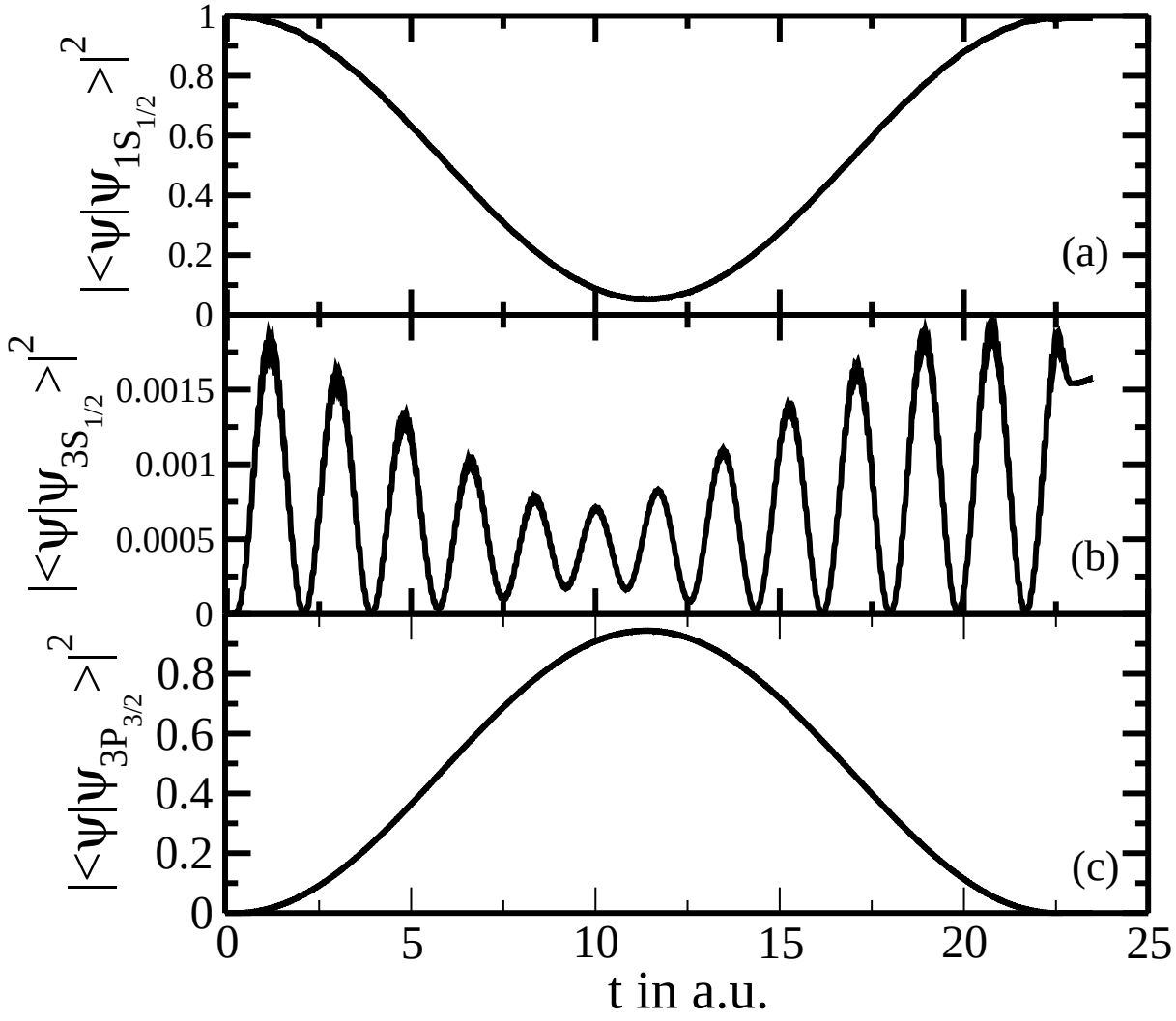

Figure 5.3: Depicted is a resonantly driven one-photon transition $|1S_{1/2}\rangle \leftrightarrow |3P_{3/2}\rangle$ in a hydrogen-like Ne^{9+} ($Z = 10$). The laser frequency $\omega = 43$ a.u. ($\lambda = 1.06$ nm) is chosen to be in resonance with the unperturbed transition of $|1S_{1/2}\rangle \leftrightarrow |3P_{3/2}\rangle$ for a field strength of $E = 10$ a.u. and a $\sin^2$-shaped pulse of 157 cycles including 3.5 cycles turn-on and turn-off ramp, respectively.

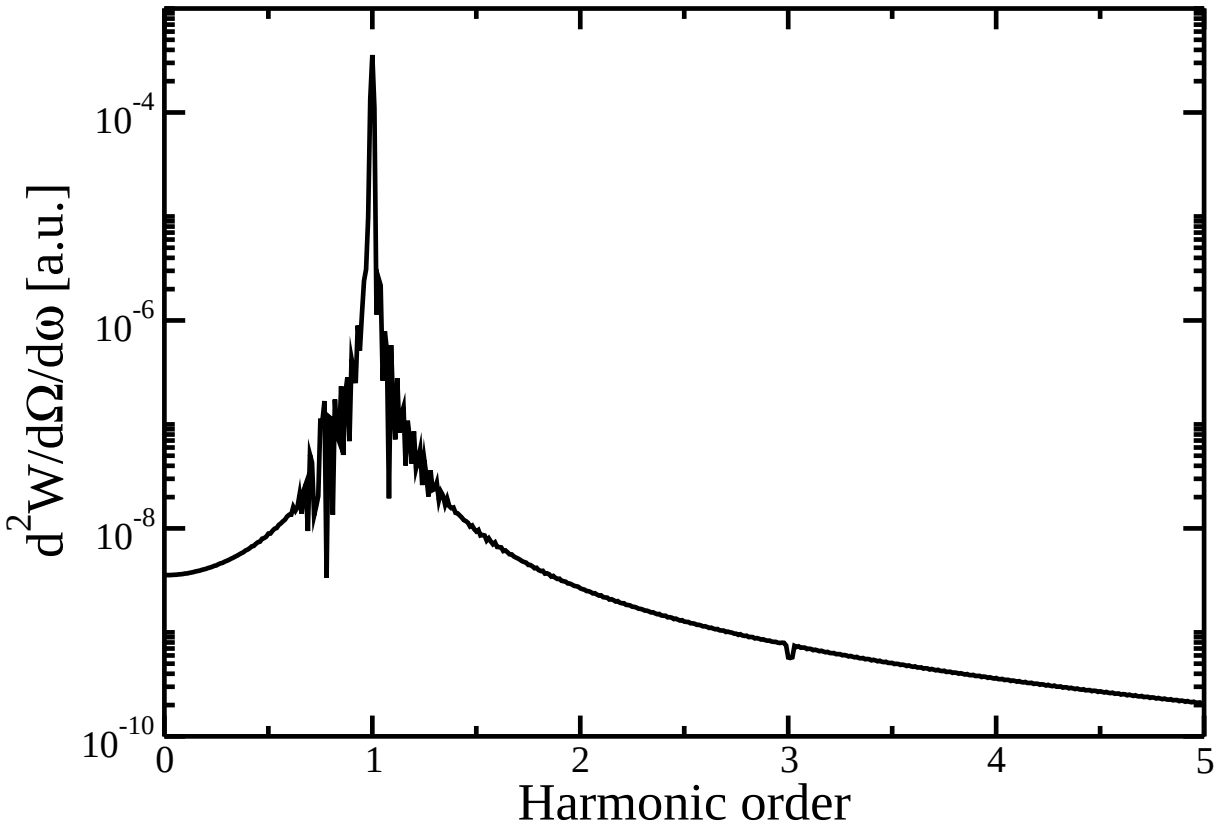

Figure 5.4: Plotted is the radiation spectrum of the resonantly driven transition of $|1S_{1/2}\rangle \leftrightarrow |3P_{3/2}\rangle$ with the same parameters as given in the caption of 5.3.

To verify the excitation of only the resonantly driven one-photon transition $|1S_{1/2}\rangle \leftrightarrow |3P_{3/2}\rangle$ we have additionally calculated the radiation spectrum of the bound dynamics plotted in Fig. 5.4. It is generated via a Fourier transformation of the dipole acceleration in laser propagation direction. The driven transition can be clearly identified as the main fundamental peak in the radiation spectrum, which represents the emission of radiation of the stimulated transition and can be principally used to detect relativistic signatures in the spectrum by comparing with non-relativistic calculations. In case of multiphoton transitions between resonantly coupled states in highly charged ions the emission frequency can reach the X-ray regime.

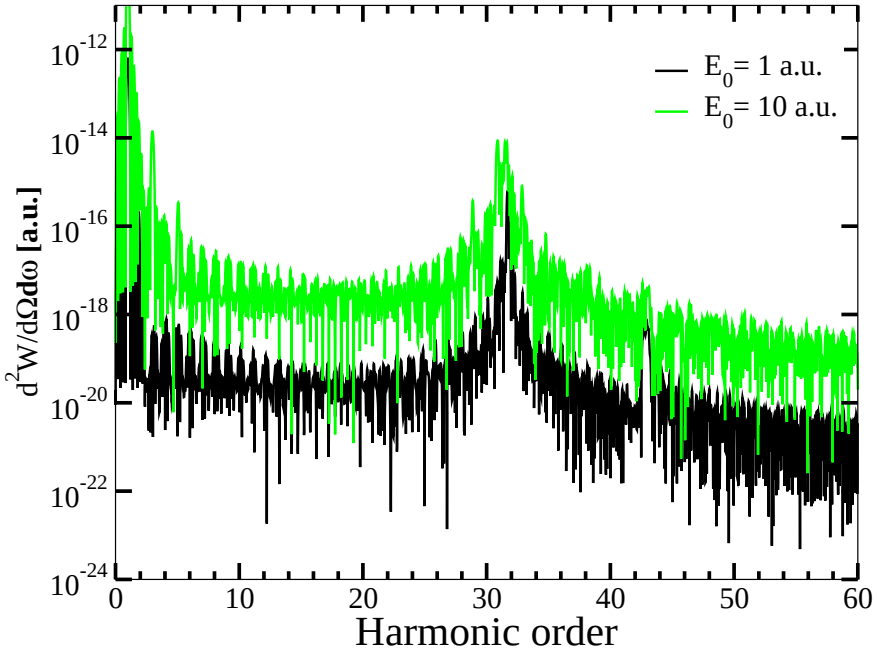

Figure 5.5: Plotted is the radiation spectrum for a laser frequency $\omega = 1$ a.u. ($\lambda = 4.56$ nm) applied to Ne^{9+} for two different field strengths. The spectrum shows the fundamental of the applied laser field strength at the first two transition from the ground state $|1S_{1/2}\rangle$ to the excited states $|2P_{3/2}\rangle$ and $|3P_{3/2}\rangle$. The pulse consist of six cycles including one cycle for the turn-on and turn-off ramp, respectively.

In the following, the dependence of the radiation spectrum on the applied laser field strength E is investigated. As an example we take an ionic core charge of $Z = 10$ and a laser field frequency of $\omega = 1$ a.u., which is smaller than the related transition frequencies in the system. For the field strengths E of 1 a.u. and 10 a.u. applied to this system the corresponding radiation spectrum is displayed in Fig. 5.5. The population is initially in the ground state $|1S_{1/2}\rangle$. The corresponding radiation spectrum consists of two other peaks at the harmonic order of 32 and 43 apart from the fundamental frequency, which belong to the transition frequency of the $|1S_{1/2}\rangle \leftrightarrow |2P_{3/2}\rangle$ and $|1S_{1/2}\rangle \leftrightarrow |3P_{3/2}\rangle$ respectively, as is clearly seen in the case of E= 1 a.u. For the higher field strength of 10 a.u. (1/100 of the atomic field strength) the second peak becomes not distinctly visible from the background oscillations arising from the Fourier transformation. The higher field strength causes somewhat greater perturbations to the energy eigenstates, related to the ac-Stark effect resulting in a smaller coupling to the laser field.

5.2.2 Three-photon transitions

Of increasing interest in the general process of intense laser-atom interaction is the coherent radiation of short-wavelengths, which e.g. are generated by bound-bound multiphoton transitions in highly charged ions. For an efficient multiphoton excitation the laser field should be strong enough to induce such a transition. However, the interactions of non-resonantly coupled energy states in a multi-level configuration need to be avoided in order to have a negligible influence on the resonantly coupled transition of interest. Moreover, it has to be assured that the laser field is not too strong in order to avoid that multiphoton ionization rates exceed the excitation rate of the considered transition.

In this section, we investigate the above discussed $|1S_{1/2}\rangle \leftrightarrow |3P_{3/2}\rangle$ transition by driving it resonantly via three photons. The three-photon transition matrix element is much smaller compared to the one-photon transition. Moreover, with the lower applied laser frequency other levels might as well be non-resonantly populated. We furthermore satisfy that only bound-bound transitions take place by choosing the laser field strength to be 1% of the mean ionic field strength, otherwise bound-continuum transitions are involved. In Fig. 5.6 the time-dependent population is depicted for the $|1S_{1/2}\rangle \leftrightarrow |3P_{3/2}\rangle$ transition. We again initially populated the ground state $|1S_{1/2}\rangle$. The laser field resonantly couples to the $|1S_{1/2}\rangle \leftrightarrow |3P_{3/2}\rangle$ transition driving the population slowly in time into the state $|3P_{3/2}\rangle$. The decreasing population probability amplitude of the $|1S_{1/2}\rangle$ state is modulated by high oscillations, which results from the coupling to the energy level $|2P_{3/2}\rangle$ for the chosen laser frequency on a much shorter time scale. As the three photon transition dipole matrix element is so small, the time for a full Rabi oscillation is numerically coming up to a limit of adequate computation time as the whole wavefunction has to be spatially and temporally kept within the numerical grid in order to project every hundred time step on to the eigenstates of the unperturbed system for the calculation of the population dynamics. However, with an interpolation of the temporal probability amplitude of the depopulation of the state $|1S_{1/2}\rangle$ we roughly estimate the Rabi frequency to be Ω_R=0.0006 a.u. and therefore the corresponding transition dipole matrix element to be d_R=6 $\times 10^{-5}$.

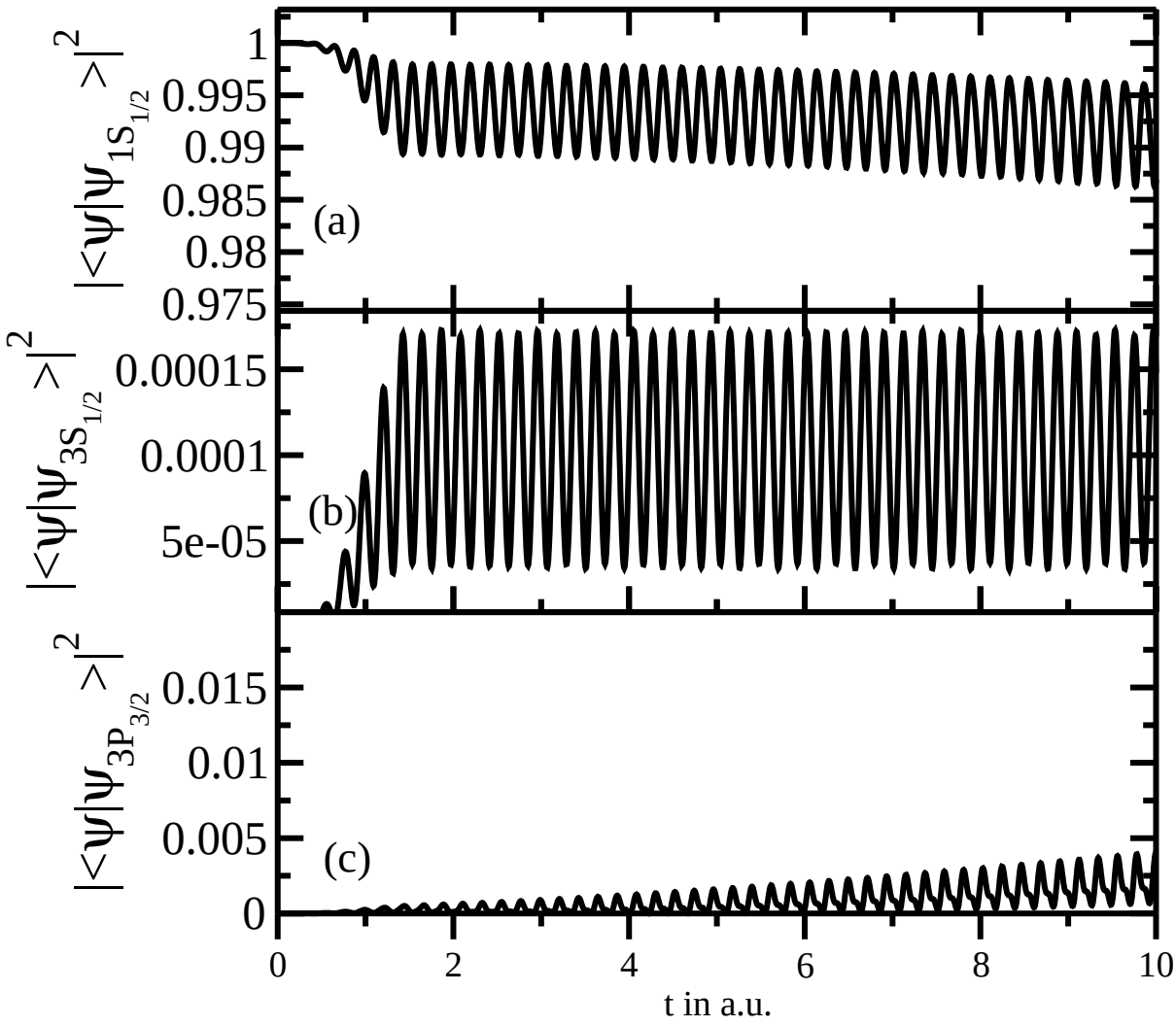

Figure 5.6: Depicted is a resonantly driven three-photon transition $|1S_{1/2}\rangle \leftrightarrow |3P_{1/2}\rangle$ in Ne^{9+}. The laser frequency $\omega = \omega_0/3$ is chosen to be in resonance via three photons with the transition frequency w_0 of the unperturbed system for a field strength of $E_0 = 10$ a.u. and a sinusoidal laser pulse of 157 cycles with 3.5 cycles turn-on and turn-off ramp, respectively.

From the radiation spectrum of the resonantly driven three-photon transition three main peaks can be distinguished. These three peaks are displayed as a function of the fundamental harmonic of the laser frequency given by one third of the unperturbed transition frequency. The second peak is thereby the corresponding peak to the three photon transition. As there exists for this three-photon transition between the states $|1S_{1/2}\rangle$ and $|3P_{3/2}\rangle$ some detuning, the corresponding radiation peak is not the highest in the radiation spectrum, but it is enhanced compared to the exponential decay of the peak height. The first peak is so strong as unfortunately the chosen laser frequency couples to the relatively strong low-lying $|2P_{3/2}\rangle$ state. The third peak represents a coupling to the excited high-lying state $|4P_{3/2}\rangle$. The oscillations of the spectrum between the three main peaks are due to the numerical Fourier transformation.

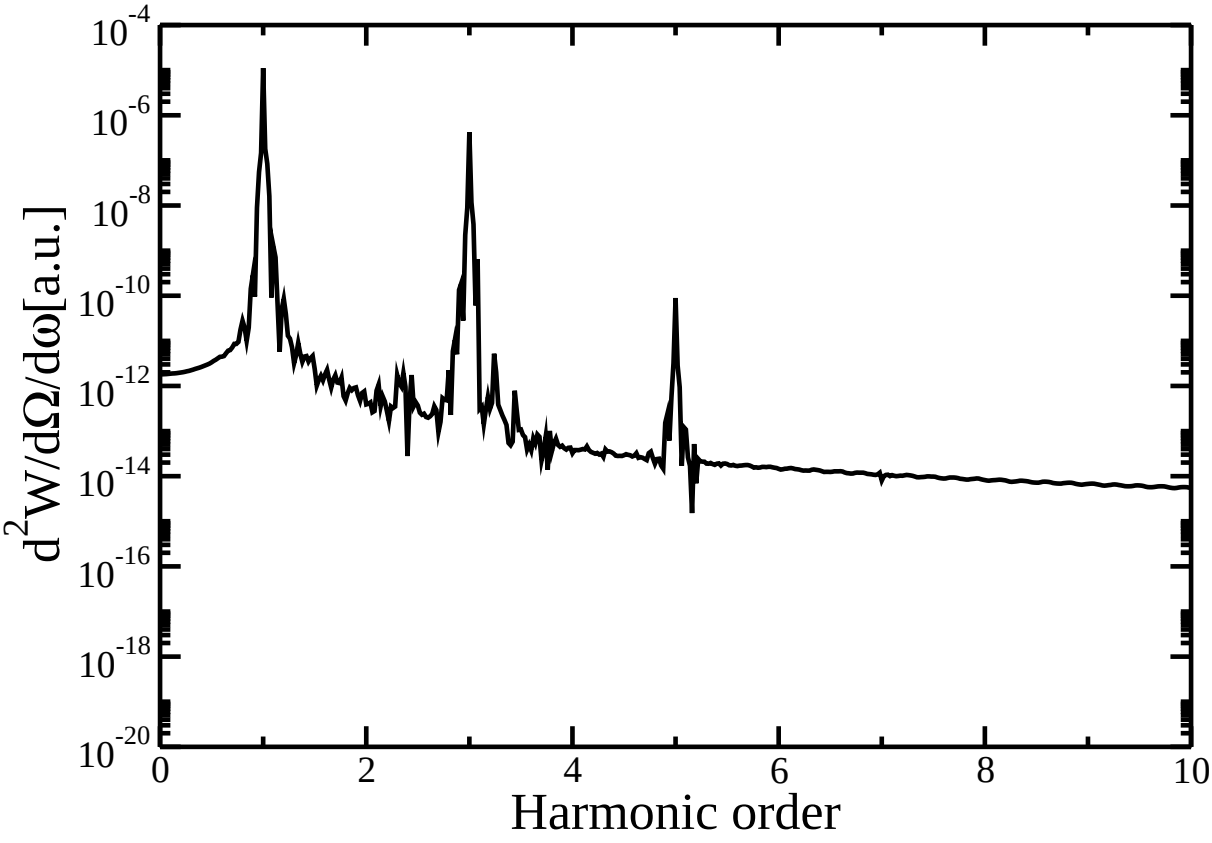

Figure 5.7: Plotted is the radiation spectrum of the resonantly driven three-photon transition of the transition $|1S_{1/2}\rangle \leftrightarrow |3P_{1/2}\rangle$. The laser parameters are the same as given in the caption of Fig. 5.6.

5.3 Conclusion

The bound dynamics has been investigated with the numerical solution of the Dirac equation in two dimensions. We focused especially on the population dynamics of the low-lying bound states of multiply charged hydrogen-like ions, taking non-dipole and relativistic orders into account. The population dynamics of multiply charged hydrogen-like ions has been evaluated by projecting the actual spatially and temporally highly resolved wavefunction on the eigenwavefunction of the associated eigenstates of the unperturbed system. We have exemplified that the one-photon transition matrix element in a full relativistic treatment of the bound dynamics can be calculated by an investigation of the population dynamics via Rabi oscillation, which is in principle also possible for multiphoton transitions. Additionally, the harmonic spectra of the related transitions have been calculated and an enhancement of a particular harmonic via a three photon resonance has been shown. The high harmonic radiation from these widely separated transition states in highly charged ions is of broad interest to be a tunable table-top source in the XUV and soft X-ray regime.

Summary and Outlook

In this thesis we focus on the relativistic dynamics of ultra-strong laser fields in multiply charged hydrogen-like ions. The related interactions can be further distinguished into an ionization and a bound dynamics regime, both of which are studied. This classification corresponds to the different ratios of the atomic field strength, that an electron on the first Bohr radius exposes, and the applied laser field strength. A laser field strength of the order of the atomic field strength or above is associated with the ionization dynamics regime, whereas laser field strengths below belong to the bound dynamics regime.

The interaction of the electron in the combined field of the Coulomb potential and the laser for both regimes has been numerically investigated by means of an integration of the classical relativistic equation of motion and by solving the Dirac equation via the split-operator method. For the latter, the calculation has been restricted to two dimensions to gain feasible computation time. For the solution of the classical relativistic equation of motion we have implemented the Runge-Kutta technique with a 4th-order adaptive step-size algorithm for the integration, where the initial relativistic ground state energy has been taken from quantum mechanics. The electron is then modeled by a microcanonical ensemble in phase space.

In chapter 2 the basic processes for both the ionization and the bound dynamics have been presented. In the case of ionization dynamics, we especially investigated the non-relativistic laser-atom interaction and the relativistic laser-ion interaction resulting in a diagram regarding the importance of magnetic field and relativistic effects as a function of the field frequency and intensity for different ionic core charges Z. In the case of the bound dynamics regime the center-of-mass motion within the dipole approximation and beyond has been studied.

In chapter 3 the numerical models of the respective calculations are presented. The numerical calculation of the energy eigenstates and their corresponding wavefunctions have been obtained via the spectral method in the Dirac case. For this approach, the Coulomb potential of the ionic core charge is approximated by a two-dimensional soft-core potential. The resolution of the height and width of the energy spectrum peaks depends on the propagation time of the associated wavefunction.

The first part of the relativistic interaction regime of chapter 4 is based on the investigation of the validity of the analytically given tunnel rate formula in the non-relativistic and relativistic case. A comparison of the ionization fraction, which is the ionization probability at the end of the pulse, has been made with the classical relativistic Monte-Carlo simulation. It has been shown that the analytical relativistic tunnel rate formula and the CTMC simulation yield similar ionization fractions in the experimentally relevant range of tunnel ionization. However, close to the critical field strength for over-the-barrier ionization the analytically calculated ionization fraction exponentially increases, thereby limiting its validity. Moreover, relativistic effects of the bound electron become important for multiply charged hydrogen-like ions above an ionic core charge of $Z = 10$.

Apart from the ionization fraction, a further observable has been studied, namely the ionization angle. This observable corresponds to the ratio of the electron kinetic momentum between the laser polarization and the propagation direction in comparison to the experimental photoelectron spectra.

Based on the study of the ionization fraction we have presented a novel method to determine most sensitively the laser intensity by measuring the ionization fraction in multiply charged hydrogen-like ions by means of a classical relativistic Monte-Carlo simulation. We showed that our proposed method is in principle not limited by any ultra-strong laser fields apart from the limit of the ionic field strength via the critical charge of $Z = 137$, which provides instable ions. The dependence of this method on typical laser parameters like the pulse length, shape and carrier phase as well as quantum effects have been studied and the extension of the method from the optical towards the XUV frequency range has been shown. The greatest impact on the measured ionization fraction arises from the

chosen pulse length and shape concerning the attained peak intensity as from quantum effects.

Favorable for a complete characterization in the future of further possible effects on the ionization fraction is to include in addition QED corrections, which are likely to contribute significantly at an ionic core charge above $Z = 50$.

In the second part, examined in chapter 5, the bound dynamics of the electron in multiply charged hydrogen-like ions has been investigated. Here, the population dynamics of various available states has been fully relativistically examined by means of the Dirac equation. The main problem of these calculations is the shift of the bound state energy due to the dynamical Stark effect, which plays a major role with increasing field strength. Moreover, the investigation has been used to calculate multiphoton transition matrix elements with the help of studying Rabi oscillations. In the associated radiation spectra these transitions have been identified.

More advantageous is the generation of even higher harmonics from these multiphoton transitions in highly charged ions. In particular the study of laser-driven multiphoton transitions is of special interest in the field of relativistic resonant interactions with highly charged ions e.g. for high precision two-photon spectroscopy, quantum optical effects such as the interference of two different initial states resonantly driven by two-color laser frequencies ending up in the same final state and the generation of harmonics in the XUV frequency range in case of highly charged ions. As a future task the study of multiphoton transitions in even higher ionic core charges should be carried out for a comparison of the transitions within the dipole approximation and beyond, as dipole forbidden states could be populated.

Appendix A

Method of finite differences

The finite difference methods are usually applied for numerical approximations of the solution of differential equations, especially on their derivatives. The simplest form is thereby the replacing of the derivative expression with approximately an equivalent difference quotient. The calculation of the derivative of the angular momentum operator has been done in section 3.2.4 by using the method of finite differences [96], based on the Taylor series of the function $f_n = f(x_n)$ for different points $x_n = nh$ with $n = 0, \pm 1, \pm 2, \ldots$. From

$$f_{\pm 1} \equiv f(x = \pm h) = f_0 \pm hf' + \frac{h^2}{2} f'' \pm \frac{h^3}{6} f''' + \frac{h^4}{24} f^{(4)} + O(h^5) \tag{A.1}$$

$$f_{\pm 2} \equiv f(x = \pm 2h) = f_0 \pm 2hf' + 2h^2 f'' \pm \frac{4h^3}{3} f''' + \frac{2h^4}{3} f^{(4)} + O(h^5) \tag{A.2}$$

the 5-point-formula for the calculation of the 1st and 2nd derivative can be easily obtained.

$$\underline{\text{1.Ableitung :}}$$

$$f' = \frac{1}{12h}[f_{-2} - 8f_{-1} + 8f_1 - f_2] + O(h^4) \tag{A.2}$$

$$\underline{\text{2.Ableitung :}}$$

$$f'' = \frac{1}{12h^2}[f_{-2} + 16f_{-1} - 30f_0 + 16f_1 - f_2] + O(h^4) \tag{A.2}$$

The ϕ derivative from Eq. 3.12 corresponds then on a 2-dimensional grid to

$$\frac{\partial}{\partial \phi} = x_1 \frac{\partial}{\partial x_2} - x_2 \frac{\partial}{\partial x_1} \, . \tag{A.2}$$

In analogy we get for the $\hat{J}^2$ operator

$$\frac{\partial^2}{\partial\phi^2} = \left(x_1\frac{\partial}{\partial x_2} - x_2\frac{\partial}{\partial x_1}\right)\left(x_1\frac{\partial}{\partial x_2} - x_2\frac{\partial}{\partial x_1}\right) \tag{A.3}$$

$$= x_1^2\frac{\partial^2}{\partial x_2^2} - x_1\frac{\partial}{\partial x_1} - x_2\frac{\partial}{\partial x_2} - 2x_1x_2\frac{\partial}{\partial x_2}\frac{\partial}{\partial x_1} + x_2^2\frac{\partial^2}{\partial x_1^2} \tag{A.4}$$

From the mixed derivative $\frac{\partial}{\partial x_2}(\frac{\partial}{\partial x_1}f_{ij})$ in J^2 we obtain the contribution

$$\begin{aligned}\frac{\partial}{\partial x_2}\left(\frac{\partial}{\partial x_1}f_{ij}\right) = \frac{1}{12h_2}\Bigg[&\left(\frac{f_{i-2,j-2} - 8f_{i-2,j-1} + 8f_{i-2,j+1} - f_{i-2,j+2}}{12h_1}\right)\\ &-8\left(\frac{f_{i-1,j-2} - 8f_{i-1,j-1} + 8f_{i-1,j+1} - f_{i-1,j+2}}{12h_1}\right)\\ &+8\left(\frac{f_{i+1,j-2} - 8f_{i+1,j-1} + 8f_{i+1,j+1} - f_{i+1,j+2}}{12h_1}\right)\\ &+\left(\frac{f_{i+2,j-2} - 8f_{i+2,j-1} + 8f_{i+2,j+1} - f_{i+2,j+2}}{12h_1}\right)\Bigg]\end{aligned}$$

For the finite difference methods exists two sources of errors, round-off error, due to the loss of precision by computer rounding of decimal quantities, and the discretization error, known as the difference between the exact solution of the finite difference equation and the exact quantity assuming perfect arithmetic, which need to be taken care of.

Appendix B

Clifford algebra

In Dirac notation the Dirac spinor Ψ is written as $\Psi = \left(\Psi_1, \Psi_2, \Psi_3, \Psi_4\right)^T$.
The standard γ matrices have the form $\gamma_0 = \begin{pmatrix} I & 0 \\ 0 & -I \end{pmatrix}$, $\gamma_k = \begin{pmatrix} 0 & -\sigma_k \\ \sigma_k & 0 \end{pmatrix}$
where k=1,2,3 and $\sigma_1 = \begin{pmatrix} 0 & 1 \\ 1 & 0 \end{pmatrix}$, $\sigma_2 = \begin{pmatrix} 0 & -i \\ i & 0 \end{pmatrix}$, $\sigma_3 = \begin{pmatrix} 1 & 0 \\ 0 & -1 \end{pmatrix}$.
These matrices fulfill the relation

$$\sigma_1\sigma_2\sigma_3 = iI \ , \tag{B.0}$$

where $i = \sqrt{-1}$ is the imaginary number. In the Dirac notation (Clifford algebra) these σ_k for $k = 1, 2, 3$ are no longer matrices but instead are vectors in the space-time algebra. They generate an algebra in $\mathbb{R}$, which is isomorph to the known Pauli algebra. In analogy to standard notation we write in the space-time algebra formalism

$$\vec{\sigma_1}\vec{\sigma_2}\vec{\sigma_3} = i \tag{B.0}$$

with $\vec{\sigma_k} = \gamma_k\gamma_0$.

The Clifford algebra in $\mathbb{R}^{1,3}$ provides a multivector from zero to forth grade, which generates the Dirac or time-space algebra. In the following table the possible combinations are listed:

Name	Grades	basis elements
scalar	0	1
vector	1	$\gamma_0, \gamma_1, \gamma_2, \gamma_3$
bivector	2	$\gamma_1\gamma_0 = \vec{\sigma_1}, \gamma_2\gamma_0 = \vec{\sigma_2}, \gamma_3\gamma_0 = \vec{\sigma_3}$ $\gamma_3\gamma_2 = i\vec{\sigma_1}, \gamma_1\gamma_3 = i\vec{\sigma_2}, \gamma_2\gamma_1 = i\vec{\sigma_3}$
trivector	3	$\gamma_1\gamma_2\gamma_3 = \gamma_0 i, \gamma_0\gamma_2\gamma_3 = \gamma_1 i$ $\gamma_0\gamma_3\gamma_1 = \gamma_2 i, \gamma_0\gamma_1\gamma_2 = \gamma_3 i$
pseudoscalar	4	$\gamma_0\gamma_1\gamma_2\gamma_3 = i$

The basis vectors in $\mathbb{R}^{1,3}$ are then defined by

$$\gamma_\nu\gamma_\mu + \gamma_\mu\gamma_\nu = 0 \qquad \Leftrightarrow \qquad \mu \neq \nu \tag{B.0}$$

For $\mu, \nu \in 0, 1, 2, 3$ apply the rules

$$\gamma_0^2 = 1 \tag{B.1}$$

$$\gamma_k^2 = -1 \quad \text{with} \qquad k \in 1, 2, 3 \tag{B.2}$$

The most general multivector in this algebra can be converted to the standard spinor notation by the decomposition of

$$\Psi = \alpha + E^k\vec{\sigma_k} + B^k i_k + \beta i \tag{B.3}$$

$$= \underbrace{(\alpha + B^3 i_3)}_{\Psi_1} + \vec{\sigma_3}\underbrace{(E^3 + \beta i_3)}_{\Psi_3} + \vec{\sigma_1}\underbrace{(E^1 + E^2 i_3)}_{\Psi_4} - i_2\underbrace{(-B^2 + B^1 i_3)}_{\Psi_2} \tag{B.4}$$

Hereby, the i_3 has to be replaced by the imaginary unit i to obtain $\Psi \in \mathbb{C}^4$ and the superscripts represents the corresponding grades in the Dirac notation.

Appendix C

Atomic units

In this thesis atomic units (a.u.) are used, if not explicitly stated otherwise In this unit system the physical constants of length, mass and charge are chosen to be

$$\alpha_0 = m_e = e_0 = \hbar = 1. \tag{C.1}$$

Here, α_0 denotes the Bohr radius, m_e the electron mass, e_0 the charge of the positron and $\hbar$ the Planck constant h reduced by a factor of 2π. The following table shows the conversion of physical quantities from atomic units in SI units.

physical quantity	atomic unit [a.u.]	SI units
energy ε	1	$27.21\,\mathrm{eV}$
electric field E	1	$5.14 \times 10^9\,\mathrm{V/cm}$
intensity I	1	$3.51 \times 10^{16}\,\mathrm{W/cm^2}$
speed of light c	137.036	$2.99 \times 10^8\,\mathrm{m/s}$
time t	1	$24.2 \times 10^{-18}\,\mathrm{s}$
angular frequency ω_0	1	$2.59 \times 10^{17}\,s^{-1}$
length α_0	1	$52.9 \times 10^{-12}\,\mathrm{m}$

The conversion of the electric field E in atomic units of a sinusoidal laser wave to laser intensities in SI units, is often used and is given by:

$$I[\mathrm{W/cm^2}] = 3.51 \times 10^{16} (E_0[\mathrm{a.u.}])^2 \,. \tag{C.2}$$

Other useful formula are e.g. the conversion of the angular frequency ω in atomic units to the wavelength λ and the photon energy $E_{ph} = \hbar\omega$ expressed by:

$$\frac{\lambda}{1\mathrm{nm}} = 45.56 \quad \frac{1\mathrm{a.u.}}{\omega} \tag{C.3}$$

$$\frac{E_{ph}}{1\mathrm{eV}} = 21.21 \quad \frac{\omega}{1\mathrm{a.u.}} \,. \tag{C.4}$$

Bibliography

[1] J. D. Bjorken and S. D. Drell, Relativistische Quantenmechanik, BI-Hochschultaschenbuch: Bd.98 Wissenschaftsverlag.

[2] D. M. Wolkow, Z. Phys. **94**, 250 (1935).

[3] W. Gordon, Z. Phys. **48**, 11 (1928); C. G. Darwin, Proc. Roy. Soc. Lond., Ser. A **118**, 654 (1928).

[4] Y. I. Salamin *et al.*, Phys. Rep. **427**, 41 (2006).

[5] A. H. Zewail, Angew. Chem. Int. Ed. **2000**, 2586 (2000).

[6] T. Brabec and F. Krausz, Rev. Mod. Phys. **72**, 545 (2000); P. Corkum, Nature **403**, 845 (2000).

[7] V. Ayvazyan *et al.*, Eur. Phys. J. D. **37**, 297 (2006).

[8] Flash report, http://flash.desy.de/

[9] The European X-Ray Free-Electron Laser Technical design report, http://xfel.desy.de/

[10] K. W. Madison, P. K. Patel, D. Price, A. Edens, M. Allen, T. E. Cowan, J. Zweiback, T. Ditmire, Phys. Plasmas **11**, 270 (2004).

[11] H. Popescu *et al.*, Phys. Plasmas **12**, 063106 (2005).

[12] S. Ter-Avetisyan *et al.*, Phys. Plasmas **12**, 012702 (2005).

[13] *European Light Infrastructure (ELI), ELI Scientific Case, http://www.extreme-light-infrastructure.eu/*(2007).

[14] G. Brodin, M. Marklund and L. Stenflo, Phys. Rev. Lett. **87**, 171801 (2001); T. Heinzl *et al.*, Opt. Commun. **267**, 318 (2006); A. Di Piazza, K. Z. Hatsagortsyan and C. H. Keitel, Phys. Rev. Lett. **97**, 083603 (2006) and *ibid.* **100**, 010403 (2008).

[15] G. Pretzler *et al.*, Phys. Rev. E **58**, 1165 (1998); K. W. D. Ledingham *et al.*, Phys. Rev. Lett. **84**, 899 (2000); T. J. Bürvenich, J. Evers and C. H. Keitel, Phys. Rev. Lett. **96**, 142501 (2006); W. P. Leemans *et al.*, Nature Phys. **2**, 696 (2006); S. M. Pfotenhauer *et al.*, New J. Phys. **10**, 033034 (2008).

[16] S. Fritzler *et al.*, Appl. Phys. Lett. **83**, 3039 (2003); H. Schwoerer *et al.*, Nature (London) **439**, 445 (2006); Y. I. Salamin, Z. Harman and C. H. Keitel, Phys. Rev. Lett. **100**, 155004 (2008).

[17] D. Strickland and G. Mourou, Opt. Commun. **56**, 219 (1985); P. Maine *et al.*, IEEE Journal of Quantum Electronics **24**, 398 (1988); M. D. Perry and G. Mourou, Science **264**, 917 (1994).

[18] M. D. Perry and G. Mourou, Science **264**, 917 (1994).

[19] M. Protopapas, C. H. Keitel and P. L. Knight, Rep. Prog. Phys. **60**, 389 (1997); T. Brabec and F. Krausz, Rev. Mod. Phys. **72**, 545 (2000); Y. I. Salamin *et al.*, Phys. Rep. **427**, 41 (2006); G. A. Mourou, T. Tajima and S. V. Bulanov, Rev. Mod. Phys. **78**, 309 (2006).

[20] S.-W. Bahk *et al.*, Opt. Lett. **29**, 2837 (2004); Y. Yanovsky *et al.*, Opt. Express **16**, 2109 (2008).

[21] L.V. Keldysh, Sov. Phys. JETP **20**, 1307 (1965).

[22] F. H. M. Faisal, J. Phys. B **6**, L312 (1973).

[23] H. R. Reiss, Phys. Rev. A **2**, 1786 (1980).

[24] P. B. Corkum, Phys. Rev. Lett. **71**, 1994 (1993).

[25] P. Agostini, F. Fabre, G. Mainfray, G. Petite, and N. K. Rahman, Phys. Rev. Lett. **42**, 1127 (1979); P. H. Bucksbaum, M. Bashkansky, R. R. Freeman, T. J. McIlrath, and L. F. Di-Mauro, Phys. Rev. Lett. **56**, 2590 (1986); G. G. Paulus, W. Nicklich, Huale Xu, P. Lambropoulos, and H. Walther, Phys. Rev. Lett. **72**, 2851 (1994).

[26] A. McPherson, G. Gibson, H. Jara, U. Johann, T. S. Luk, I. A. McIntyre, K. Boyer, and C. K. Rhodes, J. Opt. Soc. Am. B **4**, 595 (1987); M. Ferray, A. L' Huillier, X. F. Li, L. A. Lompre, G. Mainfray and C. Manus, J. Phys. B **21**, L31 (1988).

[27] S. Augst et al., J. Opt. Soc. Am. B **8**, 858 (1991); B. Walker et al., Phys. Rev. A **48**, R894 (1993).

[28] F. H. M. Faisal, A. Becker and J. Muth-Böhm, Laser Phys. **9**, 115 (1999).

[29] R. Panfili, S. L. Haan and J. H. Eberly, Phys. Rev. Lett. **89**, 113001 (2002); P. J. Ho, R. Panfili, S. L. Haan and J. H. Eberly, Phys. Rev. Lett. **94**, 093002 (2005); R. Panifili, J. H. Eberly and S.L. Haan, Opt. Express **8**, 431 (2000).

[30] D. Bauer and F. Ceccherini, Opt. Express **8**, 377 (2001).

[31] L. S. Brown and T. W. Kibble, Phys. Rev. **133**, A705 (1964); E. S. Sarachik and G. T. Schappert, Phys. Rev. D **1**, 2738 (1970); A. I. Nikishov and V. I. Ritus, Zh. Eksp. Teor. Fiz. **46**, 776 (1966); I. I. Goldman, Sov. Phys. JETP **46**, 1412 (1964).

[32] M. Protopapas, C. H. Keitel, and P. L. Knight, Rep. Prog. Phys. **60**, 389 (1997); Atoms in Intense Laser Fields, edited by M. Gavrila (Academic, San Diego, 1992); H. R. Reiss, Prog. Quantum Electron. **16**, 1 (1992); C. J. Joachain, M. Dörr, and N. Kylstra, Adv. At. Mol. Phys. **42**, 225 (2000); T. Brabec and F. Krausz, Rev. Mod. Phys. **72**, 545 (2000).

[33] A. D. Bandrauk, Molecules in Laser Fields (Dekker, New York, 1993).

[34] A. McPherson *et al.*, Nature London **370**, 631 (1994); Phys. Rev. Lett. **72**, 1810 (1994); T. Ditmire *et al.* **75**, 3122 (1995); T. Ditmire *et al.* Nature London **398**, 489 (1999).

[35] M. D. Perry and G. Mourou, Science **264**, 917 (1994); P.A. Norreys *et al.*, Phys. Rev. Lett. **76**, 1832 (1996).

[36] H. R. Reiss, Phys. Rev. A **63**, 013409 (2000).

[37] T. Stöhlker *et al.*, Phys. Rev. Lett. **85**, 3109 (2000).

[38] E. Silver *et al.*, Astrophys. J. **541**, 495 (2000); *ibid.*, Nucl. Instrument. Methods A **444**, 156 (2000).

[39] A. Schafer, Nucl. Instrum. Methods B **119**, 48 (1996).

[40] R. L. Kubena *et al.*, J. Vac. Sci. Technol. B **9**, 3079 (1991).

[41] C. A. Sacket *et al.*, Nature **404**, 256 (2000). H. R. Reiss, Phys. Rev. A **63**, 013409 (2000).

[42] D. Umstadter *et al.*, IEEE J. Quant. El. **33**, 1878 (1997); D. Umstadter, J. Phys. D **36**, R151 (2003).

[43] S. Matinyan, Physics Reports **298**, 199 (1998); A. V. Andreev *et al.*, Quant. Electron. **31**, 941 (2001).

[44] P. H. Mokler and Th. Stöhlker, Adv. At. Mol. Opt. Phys. **37**, 297 (1996); J. Ullrich *et al.*, J. Phys. B: At. Mol. Opt. Phys. **30**, 2917 (1997); J. R. C. López-Urrutia *et al.*, J. Phys. Conf. Ser. **2**, 430 (2004).

[45] E. M. Snyder, S. A. Buzza, and A. W. Castleman, Jr., Phys. Rev. Lett. **77**, 3347 (1996); T. Ditmire *et al.*, Phys. Rev. Lett. **78**, 2732 (1997).

[46] S. X. Hu and A. F. Starace, Phys. Rev. Lett. **88**, 245003 (2002); A. Maltsev and T. Ditmire, Phys. Rev. Lett. **90**, 053002 (2003).

[47] J. Javanainen, J. H. Eberly and Qichang Su, Phys. Rev. A **38**, 3430 (1998).

[48] Guido Mocken, PhD thesis (2004).

[49] Choon-Lin Ho and V. R. Khalilov, Phys. Rev. A **61**, 032104 (2000).

[50] V. R. Khalilov and Choon-Lin Ho, Mod. Phys. Lett. A **13**, 615 (1998).

[51] U. W. Rathe *et al.*, J. Phys. B: At. Mol. Opt. Phys. **30**, L531 (1997).

[52] W. E. Baylis und S. J. Peel, Phys. Rev. A **28**, 2552 (1983).

[53] Gerrard Aissing, Phys. Rev. A **44**, R2765 (1991).

[54] M. D. Feit, J. A. Fleck and Jr. A. Steiger, J. Comput. Phys. **47**, 412 (1982).

[55] V. B. Berestetskiĭ and E. M. Lifshitz and L. P. Pitaevskiĭ, Relativisitic quantum theory, Vol. 4, Pergamon Press Ltd. Headington Hill Hall, Oxford

[56] H. A. Bethe and E. E. Salpeter, Quantum Mechanics of one- and two-electron atoms, Springer-Verlag, 1997

[57] A. Baltuška *et al.*, Nature **421**, 611 (2003).

[58] Y. I. Salamin and F. H. M. Faisal, Phys. Rev. A **54**, 4338 (1996)

[59] L. S. Brown and T. W. B. Kibble, Phys. Rev. **133**, A705 (1964)

[60] Jackson, Classical Electrodynamics, (Wiley, New York), (1982).

[61] P. Strange, Relativistic Quantum Mechanics, (Cambridge University Press), (1998).

[62] R. Abrines and I. C. Percival, Proc. Phys. Soc. **88**, 861 (1966); J. S. Cohen, Phys. Rev. A **26**, 3008 (1982).

[63] H. Schmitz, K. Boucke and H.-J. Kull, Phys. Rev. A **57**, 467 (1998); L. N. Gaier and C. H. Keitel, Phys. Rev. A **65**, 023406 (2002).

[64] W. H. Press, S. A. Teukolsky and W. T. Vetterling, Numerical Recipies in C, (Cambridge University Press), (1998).

[65] L. D. Landau and E. M. Lifschitz, Mechanics, (Oxford:Pergamon Press), (1960).

[66] G. A. Mourou, T. Tajima and S. V. Bulanov, Rev. Mod. Phys. **78**, 309 (2006); Y. I. Salamin *et al.*, Phys. Rep. **427**, 41 (2006); M. Marklund and P. Shukla, Rev. Mod. Phys. **78**, 591 (2006); A. Maquet and R.Grobe, J. Mod. Opt. **49**, 2001 (2002); C. H. Keitel, Contemp. Phys. **42**, 353 (2001).

[67] N. M. Naumova *et al.*, Phys. Rev. Lett. **92**, 063902 (2004); Y. Mairesse *et al.*, Phys. Rev. Lett. **93**, 163901 (2004).

[68] *High Power laser Energy Research (HiPER), HiPER Technical Background and Conceptual Design Report, http://www.hiperlaser.org/docs/tdr/HiPERTDR2.pdf* (2007).

[69] S.-W. Bahk *et al.*, Opt. Lett. **29**, 2837 (2004);

[70] P. H. Mokler and T. Stöhkler, Adv. At. Mol. Opt. Phys. **37**, 297 (1996); T. Ditmire *et al.*, Nature **386**, 54 (1997); S. J. McNaught, J. P. Knauer and D. D. Meyerhofer, Phys. Rev. A **58**, 001399 (1998); S. X. Hu and C. H. Keitel, Phys. Rev. A **63**, 053402 (2001); S. X. Hu and A. F. Starace Phys. Rev. Lett. **88**, 245003 (2002); K. Yamakawa *et al.*, Phys. Rev. A **68**, 065403 (2003); V. P. Krainov, J. Phys. B: At. Mol. Opt. Phys **36**, 3187 (2003); V. S. Popov, Usp. Fiz. Usp. **47**, 855 (2004); J. R. Crespo López-Urrutia *et al.*, J. Phys. Conf. Ser. **2**, 430 (2004).

[71] P. Agostini *et al.*, Phys. Rev. Lett. **42**, 1127 (1979).

[72] M. V. Ammosov, N. B. Delone and V. P. Krainov, Sov. Phys. JETP **64**, 1191 (1986).

[73] A. I. Nikiishov and V. I. Ritus, Sov. Phys. JETP **23**, 168 (1966).

[74] N. B. Delone and V. P. Krainov, J. Opt. Soc. Am. B **8**, 1207 (1991).

[75] V. S. Popov *et al.*, Sov. Phys. JETP **102**, 760 (2006).

[76] N. Milosevic, V. P. Krainov and T. Brabec, Phys. Rev. Lett. **89**, 193001 (2002); V. S. Popov, B. M. Karnakov and V. D. Mur, JETP Lett. **79**, 262 (2004).

[77] T. Brabec and F. Krausz, Rev. Mod. Phys. **72**, 545 (2000).

[78] D. Bauer, Phys. Rev. A **55**, 2180 (1997).

[79] G. A. Mourou, C. P. J. Barty and M. D. Perry, Phys. Today **51**, 22 (1998); M. D. Perry *et al.*, Opt. Lett. **24**, 160 (1999).

[80] S. Augst *et al.*, Phys. Rev. Lett. **63**, 2212 (1989); E. Mevel *et al.*, Phys. Rev. Lett. **70**, 406 (1993); S. J. McNaught, J. P. Knauer and D. D. Meyerhofer, Phys. Rev. A **58**, 001399 (1998); N. Milosevic, V. P. Krainov and T. Brabec, J. Phys. B: At. Mol. Opt. Phys. **35**, 3515 (2002); Yousef I. Salamin *et al.*, Phys. Rep. **427**, 41 (2006).

[81] A. Di Piazza, K. Z. Hatsagortsyan, and C. H. Keitel, Phys. Rev. Lett. **97**, 083603 (2006).

[82] E. Goulielmakis *et al.*, Science **305**, 1267 (2004).

[83] RR. Wilson, Radiological Use of Fast Protons. Radiology **47**, 487 (1946)

[84] S. X. Hu and C. H. Keitel, Phys. Rev. A **63**, 053402 (2001);

[85] P. H. Mokler and Th. Stöhlker, Adv. At. Mol. Opt. Phys. **37**, 297 (1996); J. Ullrich et al., J. Phys. B: At. Mol. Opt. Phys. **30**, 2917 (1997); J. R. C. López-Urrutia et al., J. Phys. Conf. Ser. **2**, 430 (2004).

[86] E. M. Snyder, S. A. Buzza, and A. W. Castleman, Jr., Phys. Rev. Lett. **77**, 3347 (1996); T. Ditmire et al., Phys. Rev. Lett. **78**, 2732 (1997).

[87] G. R. Mocken and C. H. Keitel, J. Comput. Phys. **199**, 558 (2004).

[88] Petawatt High-Energy Laser for Heavy Ion Experiments, http://www.gsi.de/informationen/index.html

[89] U. W. Rathe *et al.*, J. Phys. B: At. Mol. Opt. Phys. **30**, L531 (1997); J. W. Braun, Q. Su and R. Grobe, Phys. Rev. A **59**, 604 (1999); G. R. Mocken and C. H. Keitel, Comput. Phys. Commun. **178**, 868 (2008).

[90] N. Milosevic, V. P. Krainov and T. Brabec, J. Phys. B: At. Mol. Opt. Phys. **35**, 3515 (2002).

[91] M. Sargent III, M. Scully and W. E. Lamb, Jr., Laser Physics, (Addison-Wesely, Reading, MA) (1974); C. Cohen-Tannoudji, J. Dupont-Roc and G. Grynberg, Atom-Photon Interactions, (Wiley, New York) (1992).

[92] J. H. Eberly and *et al.*, Phys. Rev. Lett. **44**, 1323 (1980); G. Rempe and H. Walther, Phys. Rev. Lett. **58**, 353 (1987); M. Fleischenhauer and W. Schleich, Phys. Rev. A **47**, 4258 (1993).

[93] private communication with Z. Harman.

[94] L. Allen and J. Eberly, Optical Resonance and two level atom, (Wiley, New York) (1975).

[95] M. O. Scully and M. S. Zubairy, Quantum Optics, (Cambridge University Press) (1997).

[96] S. E. Koonin, Computational Physics, The Benjamin/Cummings Publishing Company (1986).

Danksagung

An dieser Stelle möchte ich mich zum Gelingen dieser Arbeit bedanken bei:

- Prof. Dr. Christoph Keitel für die umfassende Betreuung meiner Arbeit am MPIK sowie der vorhandenen Freiräume, eigenen Ideen umsetzen zu können.
- Guido Mocken, der mich in die Clifford Algebra eingefürt hat und Heiko Bauke bei Fragen zu numerischen Problemen.
- Carsten Müller, der immer ein offenes Ohr für physikalischen Fragestellungen hatte.
- Peter Brunner für sämtliche Unterstützungen bei allen Computer Fragen einschließlich der Bereitstellung des vielen benötigten Speicherplatzes.
- Den Sekretärinnen Vera Beyer und Martina Weizmann für ihre freundliche und hilfsbereite Assistenz bei adminstrativen Angelegenheiten.
- allen Freunden am Institut für die viele unvergeßliche Momente.
- Michael für die wunderbaren Bergtouren, die ich sehr genossen habe und die anregenden physikalischen Diskussionen.
- Antje für ihre wundervolle Unterstützung während der Endphase dieser Arbeit und das Korrekturlesen.
- Meinen Eltern für ihren gesamten großartige Beistand.